Disorder Engineering of Ferroic Properties

by

Peter B. Meisenheimer

A dissertation submitted in partial fulfillment
of the requirements for the degree of
Doctor of Philosophy
(Materials Science and Engineering)
in the University of Michigan
2021

Doctoral Committee:

Assistant Professor John T. Heron, Chair
Assistant Professor Robert Hovden
Associate Professor Emmanouil Kioupakis
Professor Lu Li

Peter Meisenheimer
meisep@umich.edu
ORCID iD: 0000-0002-8903-3065

The work presented here would not have been possible without the contributions from many coauthors who are referenced throughout, including, in particular, computational results from L. Williams and STEM imaging from Sung S.H.

I also want to pay special mention to the people who have supported me though my time at Michigan, including (but not limited to): E. Sprague, S. Novakov, D. Del Gaudio, L. Andre, D. Vallejo, D. Greeley, B. Iezzi, K. Chou, T. Chambers, A. Bregman, B. Derby, and L. Dawahre.

I acknowledge financial support from NSF CAREER grant DMR-1847847 and the Rackham predoctoral fellowship

Table of Contents

List of Tables

List of Figures

List of Appendices

Abstract

Worldwide energy consumption is expected to increase 50% by the year 2050 [1], with as much as 25% of that being lost to waste heat from electronic devices. Multiferroic materials have the potential to mitigate this heating and volatility in computational devices [2] by allowing voltage control of a magnetic state, virtually eliminating waste heat from "always-on" Si-based technologies. This places multiferroic devices among the most competetive post-silicon technologies considering energy and delay [3, 4]. Multiferroic systems, however, are extremely rare, hindering the advancement of new technologies based on these materials. This dearth of materials can be mitigated through use of multiferroic composite systems, where, for instance, a piezoelectric layer is coupled to a magnet through strain, but further challenges exist in maximizing the coupling between layers in the composite, an effort that has seen relatively little work [5]. Additionally, existing engineering techniques utilize atomic-scale [6] or crystal-scale [7] ordering to access magnetic coupling in materials, but chemical and structural disorder is an oft explored technique that has been shown to lead to novel and colossal functional properties [8, 9, 10].

This thesis explores the intentional use of disorder as a primary phenomenon to both synthesize new ferroics and enhance material properties for superior functionalities [11, 12, 13], an orthogonal vector to addressing the scarcity of state-of-the-art materials. by using low-tempearture epitaxial growth to stabilize the disordered, α-Fe-like, phase of $Fe_{1-x}Ga_x$ out to high, metastable concentrations of Ga, both the increased spin-lattice coupling of Fe and Ga and the lattice softening associated with the phase transition can be leveraged without the formation of intermetallic phases that detract from functionality. With this technique, epitaxial, kinetic freezing of disorder, I have demonstrated a means to boost magnetostrictive coupling by as much as

10x relative to bulk [14], allowing us to show record magnetoelectric performance in a device based on the material.

Additionally, I have shown that the phase space of ferroic materials can be extended using entropy as a driving force to stabilize materials with novel chemistries [15]. By leveraging the large configurational entropy from the inclusion of many atomic species, the formation of a random, solid solution crystal can be achieved, potentially overriding other thermodynamic considerations. At elevated temperatures, a large entropic contribution to the Gibbs' free energy will stabilize the formation of a single phase, even in excess of an unfavorable heat of mixing. This metastability can be further controlled with modern thin film techniques, allowing further access to a large class of materials that have been shown to possess unusual and colossal functional properties [11, 16, 17]. For the first time, I have shown strong magnetism in these new systems [11], as well as shown that it is strongly correlated to structure and chemistry [12]. These new magnetic oxides provide a platform to investigate and tailor interplay between charge, lattice and spin via disorder for functional properties by the design of disorder.

The goal of the work presented here is to understand how engineered disorder plays a role in the tunability of functional properties. I show that low-temperature epitaxy can be used as a tool to access new, disordered, regions of the phase diagram, significantly enhancing the functional properties when compared to the thermodynamic phase [14]. Additionally, the engineering of disorder through chemistry and processing conditions can be used to further tune magnetic phenomena, introducing new order parameters to optimize the system [11, 12].

Chapter 1:

Multiferroics- a Path to Sustainable Electronics

1.1 Multiferroicity

Multiferroics are materials that possess more than one ferroic order, such as ferroelectricty [18, 19], (anti)ferromagnetism [20, 21], ferroelasticity [20, 22, 23], and/or ferrotoroidicity [24, 25, 26]. As most single phase multiferroic materials have ordering temperatures well below room temperature, severely limiting potential applications [27], our definition of a multiferroic is extended to include composite materials consisting of two individual ferroic materials, such as ferromagnet/ferroelectric bilayers [28, 29, 30, 31]. While multiferroic materials were initially discovered in the 1950's and 1960's [32], a renaissance in multiferroics research, starting in the early 2000's, has been sparked by the exciting physics that drives correlations between two or more ferroic orders [33, 34, 35, 36] and advances in thin film deposition [18, 37, 2].

For purposes of this discussion, the coupling between ferroelectric and magnetic orders (magnetoelectricity) in multiferroics is interesting because it enables magnetic field control of electrical polarization (the direct magnetoelectric effect) [38, 39] and the electric field control of magnetism (the converse magnetoelectric effect) [40, 41]. This is the modern thrust in multiferroics research because it can be used to enable

extremely sensitive low-(bio)magnetic field- sensing [42, 43, 44] and ultra-low-energy computational technologies [41, 45, 4, 46].

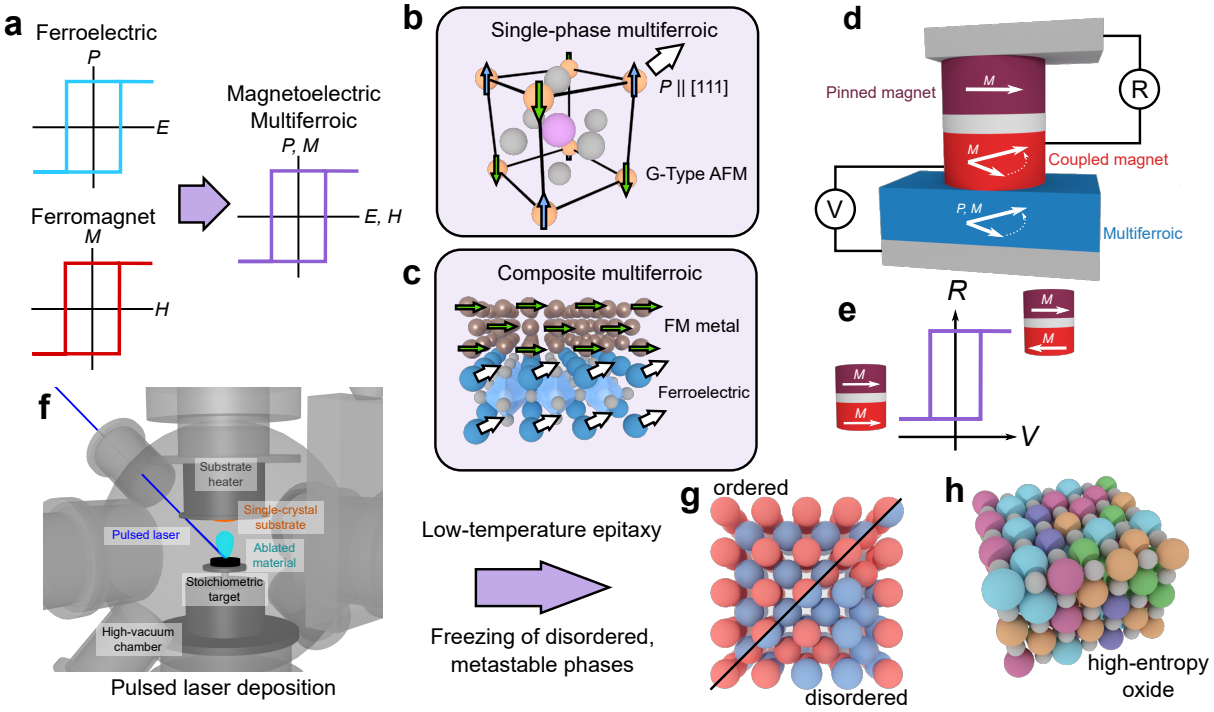

Figure 1.1: Disorder engineering of ferroic properties. Infographic showing the motivation for the research presented here. **a** Multiferroics (MF) are materials that show two or more intrinsic ferroic orders. Here, we discuss magnetoelectric multiferroics, which contain coupled ferroelectric (FE) and (anti)ferromagnetic ((A)FM) orders. In single phase multiferroics, **b**, the coexistence of FE and FM must occur through a complex physical mechanism, such as the Dzyaloshinskii-Moriya interaction or where improper FE results from a specific magnetic structure [47]. Here, the single phase MF $BiFeO_3$ (BFO) is shown, with FE and G-type AFM orders. In composite multiferroics, **c**, the material is made of two independent FE and FM phases, which are coupled through another parameter like magnetic exchange or strain. Multiferroics are exciting for many reasons, but here we will focus on the idea of multiferroic memory (**d**), where the resistive state can be switched with a voltage (**e**). In the magnetic tunnel junction (MTJ) shown here, the free magnetic layer can be coupled to a MF material, allowing a voltage to change the direction of magnetization and resistance of the device. In the search for new MF materials, I explore the use of low-temperature epitaxy (**f**) via pulsed laser deposition to stabilize new disordered phases and explore their ferroic properties. In pulsed laser deposition (PLD), because the substrate temperature is low, materials are kinetically frozen upon deposition, allowing access to as-deposited metastable phases. In particular, I have explored the synthesis of chemically disordered FeGa (**g**), for use in a composite multiferroic, and of magnetic entropy-stabilized oxides (**h**), to understand the use of disorder as a complex coupling mechanism.

While advances in the discovery of new room-temperature, single phase, magnetoelectric multiferroics are promising [7, 48, 49, 50, 51], the materials palette is still quite limited [52]. The conditions for the establishment of a polarization and magnetization

in a material are often mutually exclusive [53], yet, several mechanisms allow for a polarization to coexist with magnetic order [54]. For example, improper ferroelectric materials, in which the polarization is not the primary order parameter, often exhibit magnetic order [47]. One of the main challenges, however, is that the existence of multiferroic phenomena at room temperature is extremely rare. Additionally, magnetoelectric coupling is often too weak in these systems for device integration. Even in single phase multiferroics operable at room temperature, such as $BiFeO_3$, converse magnetoelectric coefficients tend to be low [54, 55, 56] and must be enhanced to facilitate real applications. The development focus for the field primarily lies in composite systems coupled through strain and interlayer magnetic exchange [2], because this is where the largest converse magnetoelectric coefficients and most reasonable switching times reported to date have been observed [57, 3]. These points illustrate the primary materials challenges in the field: 1) the optimization of materials for integration into composite systems, and 2) the discovery of new ferroic materials based on interesting order parameters.

Regarding the first point, the performance of composite multiferroic devices based on strain has been limited by the properties of magnetic layer. Ferroelectrics/piezoelectrics is a field that has been undergoing optimization for more than a century, but it has recently been noted that a significant need in multiferroics is the engineering of magnetostrictive magnets [5]. Regarding the second point, multiferroicity and magnetoelectricity in single phase materials is often based on complex phenomena. Because these materials are almost always magnetic oxides, they are very sensitive to small changes in lattice and electronic structure. To solve these materials challenges, I aim to use disorder and thin film epitaxy to explore new phases of magnetic materials and their structure property relations. Epitaxial stabilization is well known to give a significant degree of control over the structure and properties of oxides [58, 59, 60]. By depositing thin-film materials at low temperatures, new, metastable, phases can be accessed with potentially significantly enhanced properties with regards to bulk, and even other thin film depositions.

In thin film deposition techniques like PLD, the kinetics of material formation are

strongly influenced by the temperature of the substrate [61, 62, 63, 64]. When the substrate temperature is low, adatoms have significantly less kinetic energy and diffusion is slow, which can be seen by looking at the atomic jump frequency,

$$\nu = \nu_0 \exp(-E_a/k_B T), \tag{1.1}$$

which decreases exponentially with decreasing temperature (Figure 1.2b). This means that films are effectively frozen into their as-deposited configuration which, in the case of PLD, is something that is ideally atomically disperse. Using this technique and forcing a certain crystal system with epitaxial templating, high quality, disordered crystals can be reliably grown in an effort to study how disorder plays a role in controlling functional phenomena. Here, I discuss my work exploring low-temperature epitaxy to synthesize new material phases: novel magnetostrictors for use in strain-coupled composite multiferroics, and entropy stabilized magnets to investigate structure property relations in a new class of materials.

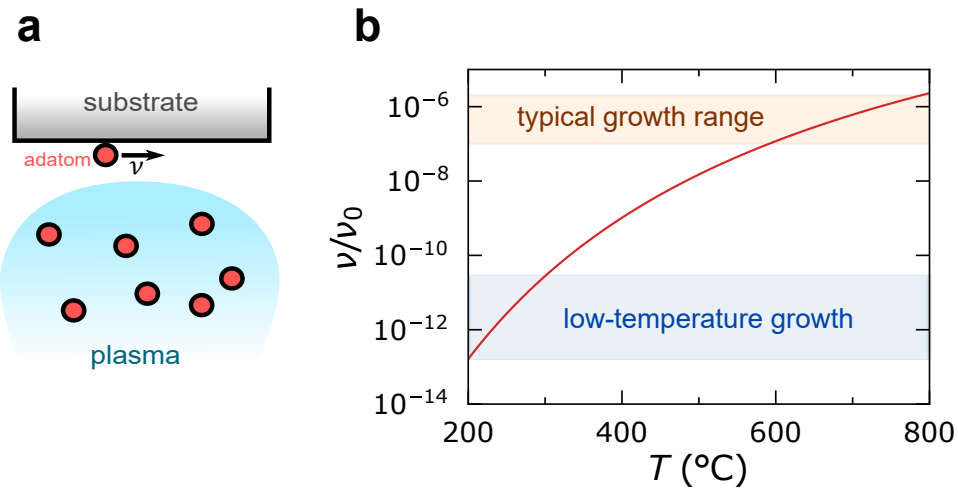

Figure 1.2: Low-temperature film growth with PLD. a Schematic of condensation on a substrate surface during PLD. **b** Estimation of the atomic hopping frequency, ν, showing the difference in atomic mobility between more typical PLD substrate temperatures (600°-800°C) and low temperature deposition (200°-300°C) can be 5 or more orders of magnitude. ν/ν_0 is calculated using an activation energy of E_a = 1.1 eV, a typical value for adatoms during PVD [64].

1.2 Strain-Coupled Magnetoelectric Heterostructures

Composite multiferroic structures are most commonly constructed by taking advantage of magnetization modulation through the application of strain by the piezoelectric layer and magnetostriction of a ferromagnet. In these strain-coupled materials, a magnetostrictive ferromagnetic layer is strained by a piezoelectric/ferroelectric crystal [65, 66] to produce changes in magnetic anisotropy [66, 67, 68, 69] and control the associated energy landscape through magnetostriction, as represented in Figure 1.3a.

The magnetostriction coefficient, usually denoted as λ_{ijkl}, describes how a material transduces magnetization into strain according to the relation

$$\epsilon_{ij} = \lambda_{ijkl} m_k m_l = -C^{-1}_{ijmn} B_{mnkl} m_k m_l, \tag{1.2}$$

where C_{ijmn} is the stiffness tensor, B_{mnkl} is the magnetoelastic energy, and m_k, m_l are the direction cosines of the magnetization [70, 71]. Physically, this originates from changes in the band structure of the material due to the mechanical distortion. Effectively, as a crystal is strained and the atoms move, the band structure will change which can deplete/add to the spin-dependent density of states of a ferromagnet [72, 73, 74]. Macroscopically, this is observed as the change in magnetocrystalline anisotropy per change in strain,

$$B_{mnkl} = \frac{\partial K_{mn}}{\partial \epsilon_{kl}}, \tag{1.3}$$

where K_{ij} is the magnetic anisotropy and ϵ_{kl} is the strain [75]. As this is an effect of the magnetic anisotropy energy, it is proportional to the spin-orbit coupling of the material [74] and ferromagnets with large spin-orbit coupling, like rare earth containing materials, tend to also exhibit large magnetostriction coefficients. Additionally, materials that are mechanically isotropic (i.e. the ratio of components of C_{ijmn} approach 1 or the shear modulus goes to 0) show larger magnetostriction values since λ is proportional to $C^{-1}B$. Experiments with strain-mediated composite magnetoelectrics usually employ conductive magnets with large magnetostrictive coefficients (λ) such as rare-earth containing Terfenol-D [76] ($\lambda \approx 1200$ ppm), Galfenol ($Fe_{1-x}Ga_x$) [77, 51] ($\lambda \approx$ 250 ppm), FeRh [78] (ferromagnet-antiferromagnet transition), CoFeB [76, 79] ($\lambda \approx 50$

ppm), and Ni [80] ($\lambda \approx$ -34 ppm).

As a demonstration of these physics, magnetostrictive magnet have been used to template domains from a ferroelectric substrate, being coupled through local strain states. By depositing magnetostrictive CoFe on a $BaTiO_3$ substrate, the in-plane strain state of a1-a2 domains in the $BaTiO_3$ create localized easy axes in the magnetostrictive magnet, effectively mapping the polarization of the substrate directly into a magnetic domain (Figure 1.3b) [66]. This effect has been duplicated with other magnetic films, such as LSMO and $CoFe_2O_4$ [81]. Functionally, this has been used to control domain walls in the magnetostrictor since, as ferroelectric domains are moved in the pre-switching regime, magnetic domain walls will track their location. [82, 67].

Projecting existing studies of strain-coupled multiferroics to the devices scale, researchers have been able to achieve energy dissipations per area per switch on the order of 1 - 100 μJ cm^{-1} [3], making these devices competitive in the realm of post-Si technologies[83, 84]. While much of the early work in strain-coupled multiferroics was done using bonded piezoelectric transducers [85, 86], scale devices necessitate thin film magnets deposited on high-strain piezoelectric crystals, typically relaxor-type $PbTiO_3$ (PTO) derivatives such as $Pb(Zr,Ti)O_3$ (PZT) [80, 21, 38] and $Pb(MgNb)O_3 - PbTiO_3$ (PMN-PT) [79, 87, 88]. Strain mediation has widely been used to manipulate the energy landscape in composite materials [89], changing coercive fields and the depth of the potential well along the easy axis (Figure 1.3c), however full switching of the anisotropy axis is much rarer [77, 90].

By leveraging epitaxy between the two ferroic layers to maximize strain transfer, researchers have been able to realize 90° switching of magnetization in a quasi-macroscale structure (epitaxial FeGa thin film heterostructure bonded to a bulk piezoelectric transducer) [77], demonstrated in Figure 1.3d,e. Additional experimental reports have demonstrated that enough magnetoelastic energy can be generated to drive 90° reorientation of anisotropy [66, 77, 88], but 180° switching, which is desired for maximum readout, may not be achievable unless sequential voltages are applied or material symmetries are broken by external stimuli like magnetic fields or spin torques

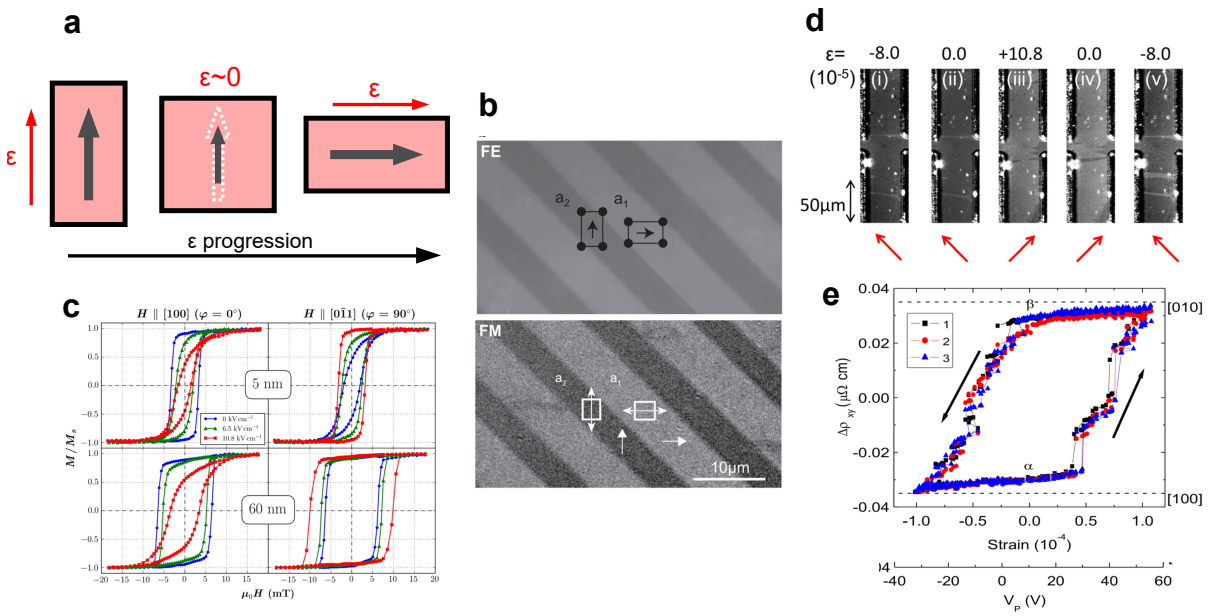

Figure 1.3: Strain mediated ME switching. a Schematic of strain-mediated switching in a composite multiferroic heterostructure. Application of an electric field (E) induces a ferroelastic strain (ϵ) through the converse piezoelectric effect, which modifies the strength of the magnetic anisotropy and/or magnetic moment in the magnetostrictor, shown by the large arrow. **b** Birefringent (top) and magneto-optical Kerr effect (MOKE, bottom) images showing domain mapping from ferroelectric to ferromagnetic domains based on the in-plane strain state. **c** Magnetic hysteresis loops, showing the change in magnetic anisotropy of a $Fe_{81}Ga_{19}$/PMN-PT heterostructure under electric field. **d** Magneto-Optical Kerr Effect (MOKE) images showing reversible, strain dependent magnetization orientation of an $Fe_{0.8}Ga_{0.2}$/PMN – PT multiferroic heterostructure. The greyscale contrast in the images shows the domain structure and the red arrows show the magnetization direction. **e** Transverse AMR of the device in **d**, showing hysteretic switching of the resistance, corresponding to the magnetization direction, as a function of strain and applied electric field. Part a from ref [91], part b from ref. [66], part c from ref [92], parts d,e from ref [77].

[93, 94, 95, 96]. Additionally, much of the existing work on magnetization/anisotropy switching has been achieved in bulk composites, partially due to the difficulty of working with thin films of the best magnetostrictors (e.g Terfenol-D). Researchers have been optimizing ferroelectrics for many decades, but optimization of magnetostrictive layers has only very recently become a point of interest [97]. This issue, a dearth of magnetostrictive ferromagnets, is understood and has been explicitly noted by experts in the field as being a primary concern [5].

The issues with rare-earth based magnetostrictors stem from sustainability and significant challenges in processing. Thus, if a sustainable materials with a comparable magnetostrictive coefficient can be realized, it will have a significant impact on the field and future of the technology. Electron correlations and quantum phenomena

emergent from Berry curvature in novel electronic structures enable new paradigms in this area. For example, the transition metal alloy FeGa has recently demonstrated efficient transverse thermoelectric energy conversion due to a large Berry curvature stemming from the significant spin-orbit coupling or nodal line structure [98, 99]. Magnetostrictive materials historically rely on rare earth components to enhance spin orbit coupling, yet we observe that the rare-earth free FeGa may boast one of the highest magnetostrictive coefficients recorded. this is done through disorder engineering of the material, using the combination of entropy and thin film techniques to stabilize a novel, disordered phase of the alloy with new exciting properties.

1.3 Introduction to High-Entropy Crystals

Historically, thermodynamics driven by the enthalpy of formation have been the guiding principle for discovery and design of new oxide crystals. Within this paradigm, highly controlled thin film epitaxy is used as an engineering control to extend the material space beyond that of the bulk phase diagram. In the past few years, entropy instead of enthalpy is starting to be explored as an orthogonal approach to the discovery of new materials and properties. In the nascent field of high-entropy oxides, multicomponent oxides where the configurational entropy is larger than or comparable to the enthalpy of mixing, an enormous potential space of new compositions is being targeted for applications across the entire ceramics field. As new chemistries are being synthesized, research is expanding to studies understanding how these new local and global degrees of disorder and frustration interplay with functional phenomena. In this section, I present a brief history of the field with a particular focus on functional phenomena. For all the reasons normal oxide crystals are targeted for applications, e.g. broken crystal symmetries, interesting correlated phenomena, and magnetism, exploration into high-entropy oxides has begun and a number of these phenomena have begun to be seen. Excitingly, the disorder in these oxides allows for new interplay between spin, orbital, charge, and lattice degrees of freedom to design the physical behavior.

High-entropy materials, popularized by the discovery of high-entropy metal alloys

20 years ago [100, 101, 102, 103], typically include 5 or more atomic species and are kinetically frozen into a metastable solid solution [104, 105] that is generally thought of as disperse on an atomic scale [100, 106, 107]. Properties of high entropy materials can be characterized by either rule-of-mixtures or cocktail effect behavior, depending significantly on the particular composition and property. Distinct from high-entropy crystals, where the only criteria is that configurational entropy is "large", in entropy-stabilized materials, the configurational entropy contribution to the Gibbs' free energy is actually large enough to drive the formation of a single phase solid solution [101, 15], potentially even in excess of a positive enthalpy of formation [108]. Beyond metal alloys, high-entropy and entropy-stabilized oxides (HEOs and ESOs) have attracted significant interest largely due to the prospect for increased hardness, toughness, and thermal resistance [105, 109]. Oxides are, however, a playground for the exploration of correlated-electron phenomena, such as ferroic properties, superconductivity, and metal-insulator transitions.

High-entropy materials are often defined by their large entropy of mixing, ΔS, in Gibbs' free energy of formation,

$$\Delta G = \Delta H - T\Delta S \tag{1.4}$$

which stems from a large number (i) of constituent species. Here, the entropy ΔS_{conf} can be expressed as:

$$k_{\text{B}} \sum_{\text{i}}^{N} x_{\text{i}} \ln(x_{\text{i}}), \tag{1.5}$$

where N is the number of species and x_{i} their compositions. If this Δi term is large, at high temperatures is can drive ΔG to be negative, which signifies thermodynamic stability. Potentially the most exciting prospect of these materials, is that this entropic term can actually override a positive enthalpy of mixing, allowing access of novel phases. The implication here, is that entropy-engineering can be use to force normally immiscible species into novel oxide phases. This ability to realize new phases and stereochemistry opens a new space for the synthesis and design of oxide materials. Because these materials become metastable when cooled, however, non-equilibrium synthesis processes, such as PVD, may be required. When deposition temperatures are low,

adatoms are kinetically frozen at the substrate, preventing diffusion and allowing easy access to metastable phases [110, 111, 112, 108].

Due to the enhanced solubility inherent in ESOs, researchers have new tools to study competing internal charge, spin, structural, and orbital order/disorders that can develop new functional frustrations (e.g. the phenomena that occurs in relaxor ferroelectrics). Using these new degrees of freedom, materials can be engineered with new properties arising from different disordered length scales. Existing techniques for the study and synthesis of thin-film correlated oxides, such as multiferroics [37, 2], take advantage of a number of thin film paradigms such as layer-by-layer growth [7] and interfacial control [113, 114, 55, 58] making tunability and precise control of structure and stereochemistry critically important. This means fabrication of these materials is generally limited by solubility, as chemistries can only be controlled a limited amount within the enthalpies of mixing. This may be the significant opportunity for ESOs, as not only does the structure appear to be robust and controllable, showing crystallinity within growth windows spanning hundreds of degrees and pressures [108, 115], but entropy engineering vastly increases the potential phase space where materials can be discovered. This significant tunability of structure and chemistry coupled with recent observations of functionality in HEO/ESOs [12, 116, 117], opens opportunities for studying the interplay between charge, spin, lattice, and orbital degrees of freedom in highly disordered crystalline materials.

Chapter 2:

Disorder-Engineered Enhancement of Magnetostriction

Magnetoelectric multiferroic systems [3, 77, 118, 31, 30] have emerged as promising materials for low-energy, beyond-CMOS memories [45, 4] and extremely sensitive magnetic field sensors [119, 43]. This has motivated research on both single-phase [41, 120, 7] and composite [77, 31, 76, 121, 69] multiferroic materials which exhibit magnetic modulation driven exclusively by electric field. While single-phase multiferroics may show strong antiferromagnetic-ferroelectric coupling, they are rare at ambient conditions [7]. Alternatively, strain-mediated composite multiferroic heterostructures offer increased magnetoelectric coefficients and device utility [3, 30] through the combination of a wide array of magnetostrictive ferromagnets (Ni, FeGa, Terfenol-D, etc.) and piezoelectric substrates (PZT, PMN-PT, etc.) or commercially-available piezoelectric transducers. While existing composites show impressive electrically-driven magnetic reorientation capabilities, device performance has been limited by the magnetostrictive properties of the magnetic layer. It has recently been noted that a significant need in the field is the engineering of magnetostrictive magnets [5], as existing materials systems have small coefficients, such as Ni and CoFeB, or are expensive and difficult to process, as is the case of rare-earth-based magnetic alloys (Terfenol-D). Here, we present a means to boost the magnetostriction of FeGa alloys by as much as 20x through disorder engineering and utilize this to demonstrate bipolar, 90° switching of magnetization via electric field in a device with exceptional

performance. Our results demonstrate that by engineering epitaxial materials into an extended phase space, high performance magnetostrictors and magnetoelectric multiferroics can be achieved.

In bulk, FeGa undergoes a phase transition at 18% Ga from a disordered A2 phase, at low concentrations of Ga, to an ordered BCC phase ($D0_3$) [122, 74]. Until this point, the magnetostriction of FeGa increases with increasing Ga incorporation, but sharply drops after 18% due to the formation of the parasitic intermetallic phase [123]. Previous reports have shown that the formation of this D03 phase can be suppressed by quenching, extending the range of the A2 phase and increasing the peak magnetostriction coefficient [73]. We hypothesize that a similar effect can be achieved in thin films, as a distinct advantage of epitaxial growth is the potential to access metastable phases, allowing us to promote the chemically disordered BCC (A2) phase in our film at high (20-30%) gallium concentrations. Furthermore, we aim to leverage the second phase change of FeGa at 30% Ga and the accompanying lattice softening to further increase the magnetostriction.

2.1 Material Structure

Our samples consist of epitaxial (001)-oriented, 15 nm A2 (α-Fe) phase, magnetostrictive $Fe_{1-x}Ga_x$ (x = 0.23, 0.245, 0.30) single crystal films on (001)-oriented PMN-PT substrates deposited by molecular beam epitaxy (Figure 1a). High-angle annular dark-field scanning transmission electron (HAADF-STEM) micrographs (Figure 2.1b) reveal the deposition of single crystalline, phase-pure FeGa films on PMN-PT with a clean and coherent interface. We observe the epitaxial orientation relationship [100]s PMN-PT//[110] $Fe_{1-x}Ga_x$ with a 45° in-plane rotation between FeGa and PMN-PT from a cube-on-cube orientation relationship. This relationship is shown schematically in Figure 2.1c. Select area electron diffraction (SEAD) images show only peaks with even Bragg indices (Figure 2.1d), indicating the films are in a disordered body centered cubic (BCC) crystal structure (α-Fe phase) due to the absence of ordered superlattice peaks. The relative Ga:Fe concentration was measured to be 21.5 ± 3%Ga using quantitative electron energy loss spectroscopy (EELS) based on Hartree-Slater in-

elastic cross sections described below. Notably, the studied concentrations are well beyond the formation threshold of the ordered FeGa intermetallic phase at 18%Ga, yet our films remain in the A2 phase, showing that epitaxy allows us to extend the stability of the region.

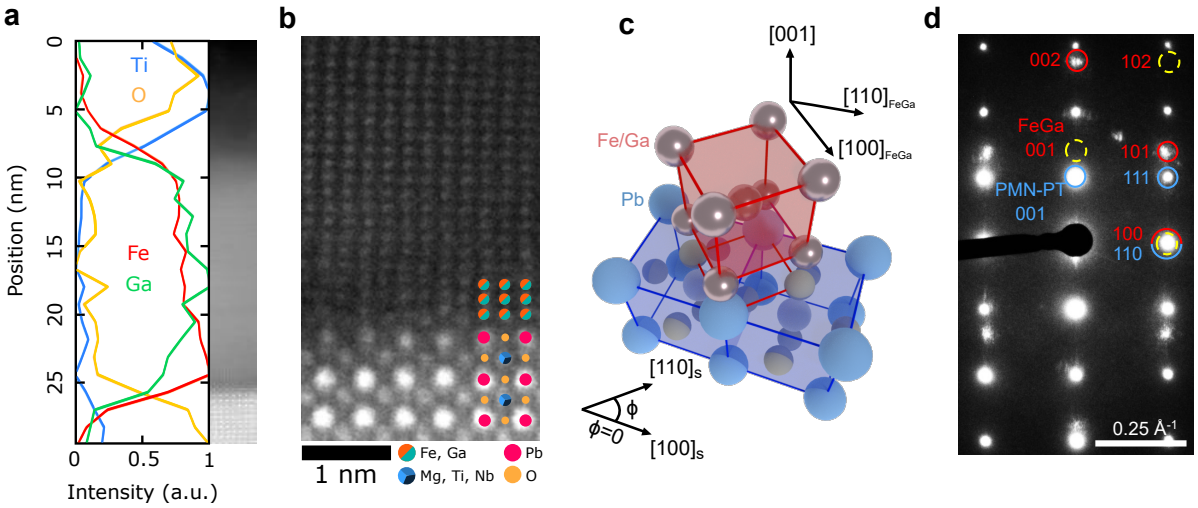

Figure 2.1: Epitaxial stabilization of A2 FeGa on (001) PMN-PT. a Electron energy loss spectroscopy (EELS) of the PMN-PT substrate and FeGa film as a function of film thickness, showing abrupt concentration edges and a nominal thickness of 15 nm for the FeGa film. Ti signal comes from the capping layer to prevent oxidation. **b** High-angle annular dark-field scanning transmission electron (HAADF-STEM) micrographs along the PMN-PT [100] / FeGa [110] zone axis, showing the single crystalline, epitaxial relationship along the $[100]_s$ (substrate) direction. **c** Diagram showing the epitaxial relationship of PMN-PT (blue) and FeGa (red) normal to the interface ([001] direction), marking the crystallographic directions of the film and the substrate. **d** Interfacial select area electron diffraction (SAED) confirming that the FeGa thin film is in the disordered A2 phase due to the absence of superlattice peaks which would appear in the ordered $D0_3$ phase. Bragg peaks of the FeGa (red) only appear when the sum of reciprocal lattice indices are even (missing peaks shown as yellow dashed circles), indicating a solid solution BCC crystal structure. Parts **a,b**, and **d** are collected from a representative 30% Ga sample. Adapted from ref. [14].

The FeGa thin films presented were grown by molecular-beam epitaxy in collaboration with R. Steinhardt, the process of which is described in the methods section of ref. [14]. HAADF-STEM, EELS, and EDS data were collected in collaboration with S.H. Sung, which is also described in ref. [14].

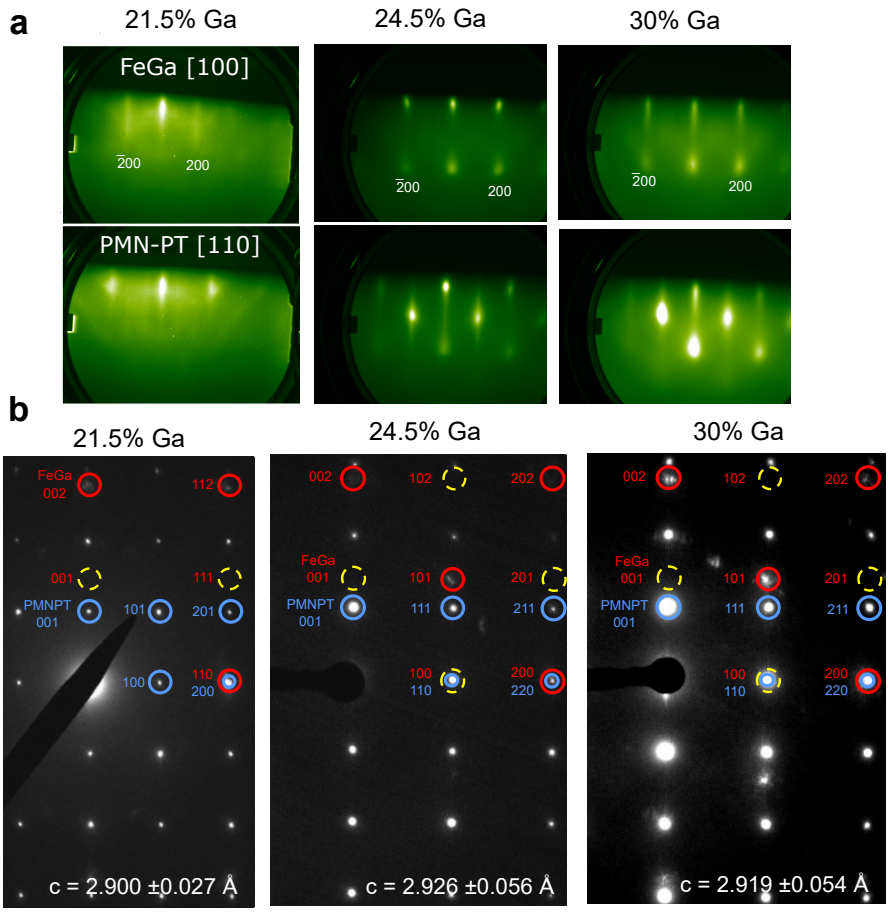

Figure 2.2: Diffraction data from FeGa. a In-situ reflection high energy electron diffraction (RHEED) data on the $[110]_s$ azimuth of the PMN-PT substrate and the [100] of the FeGa film. RHEED data shows no signal corresponding to the 100 peak of the FeGa, indicating that the films are in the disordered, A2-like phase. **b** Select area electron diffraction (SAED) pattern of FeGa thin films, which confirms FeGa thin film is in the A2 phase rather than intermetallic B2 or $D0_3$ across different Ga concentrations. FeGa Bragg peaks FeGa (yellow dashed line) is extinct when sum of reciprocal lattice indices are odd, which occurs only in the A2 phase. The out-of-plane lattice constants of the FeGa film calculated from diffraction images are shown in the table with error bars. Adapted from ref. [14]

2.2 Magnetoelectricity

To study how the magnetostriction of the FeGa films is influenced by the phase and Ga concentration, we utilize magnetotransport measurements to extract the values from multiferroic performance. The films are lithographically patterned into 10 μm × 50 μm devices, as shown in Figure 2.3a, oriented along the substrate [100] or FeGa [110] direction, the experimentally determined magnetic easy axis of the FeGa (Sup. Figure 4). Electric fields were applied across the entire substrate thickness using the device as the ground and a back contact for the hot lead. Anisotropic magnetoresistance (AMR) measurements were carried out as a function of angle and magnetic field to determine the direction of the magnetization and magnetic anisotropy. Under an electric field of +/-4 kV cm^{-1}, low magnetic field (50 Oe) AMR scans show a 90° phase shift of the sinusoidal resistance (Figure 2.3b) revealing a 90° separation of magnetization directions for the two applied electric fields. When saturated at +(-)4 kV cm^{-1}, the magnetization lies approximately +(-)45° from the current direction, meaning the magnetization is pulled along the substrate [110] ([1$\bar{1}$0]) direction. This is the hard axis of the as-grown FeGa layers, indicating that the magnetization direction is dominated by an external voltage-controlled anisotropy. Figure 2.3c shows the direction of the magnetization, relative to the x-direction, versus electric field. From this measurement we infer that the non-volatile ferroelastic strain from the substrate is oriented along the [110] and [1$\bar{1}$0] directions, depending on the applied voltage, and is strong enough to overcome the intrinsic anisotropy barrier of the FeGa.

The magnetization direction versus electric field loop can first be used to quantify an effective converse magnetoelectric coefficient, $|\alpha_{\text{eff}}|$, of our epitaxial composite multiferroic. We define $|\alpha_{\text{eff}}|$ from the expression for the magnetoelectric coefficient,

$$\alpha = \mu_0 \frac{\mathrm{d}M}{\mathrm{d}E}, \tag{2.1}$$

demonstrative of a magnetization emerging from an applied electric field, to also include the vector rotation of magnetization in the frame-of-reference of the device,

$$M = \mathbf{M} \bullet \mathbf{l} = M_{\text{S}} \cos(\phi), \tag{2.2}$$

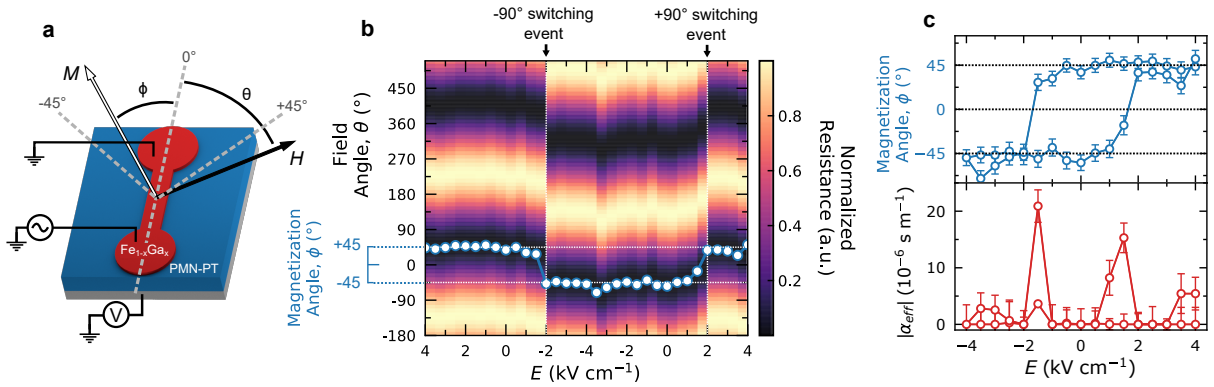

Figure 2.3: Magnetoelectric switching of FeGa. a Schematic of the FeGa/PMN-PT device. Voltage is applied across the substrate, using the device as a top ground, and resistance is measured along the bar as a function of magnetic field strength and direction (ϕ). **b** Color map of low-field (50 Oe) AMR curves fit to $\cos(2\theta)$, showing the normalized resistance as a function of magnetic field direction (θ) and applied electric field. The overlain points correspond to the calculated phase shift from the data, which is the direction of magnetization, ϕ. The two saturated polarization states of the ferroelectric show a 90° phase shift in the curve, demonstrating a 90° switching of magnetization. **c** Hysteresis of the anisotropy axis, with respect to the direction of the device (x), as a function of electric field, and effective converse magnetoelectric coefficient ($|\alpha_{\text{eff}}|$), reaching a maximum value of 2.0 • 10^{-5} s m^{-1} during switching. Parts **b** and **c** show the representative 30% Ga sample with the largest magnetoelectric coefficient. Adapted from ref. [14].

where **l** is the direction of current. Additionally, we only report the absolute value of this quantity as the high field AMR measurements preclude the handedness of magnetization rotation and the sign of the magnetoelectric coefficient. This definition then allows for

$$|\alpha_{\text{eff}}| = \mu_0 M_S \frac{\partial \cos\phi}{\partial E}, \tag{2.3}$$

where μ_0, M_S, and E are the vacuum magnetic permeability, the saturation magnetization, and the applied electric field, respectively. Applying this to our magnetoelectric hysteresis loops, we see that the converse magnetoelectric coefficient can reach the giant value of 2.0 • 10^{-5} s m^{-1} in our highest Ga concentration samples (Figure 2.3d).

2.3 Analytical Model

The magnetostriction of thin films historically has only been extracted indirectly from their magnetoelastic coupling coefficients [124]. This is done by analyzing strain-induced change in magnetic anisotropy (or easy-axis reorientation) using analytical

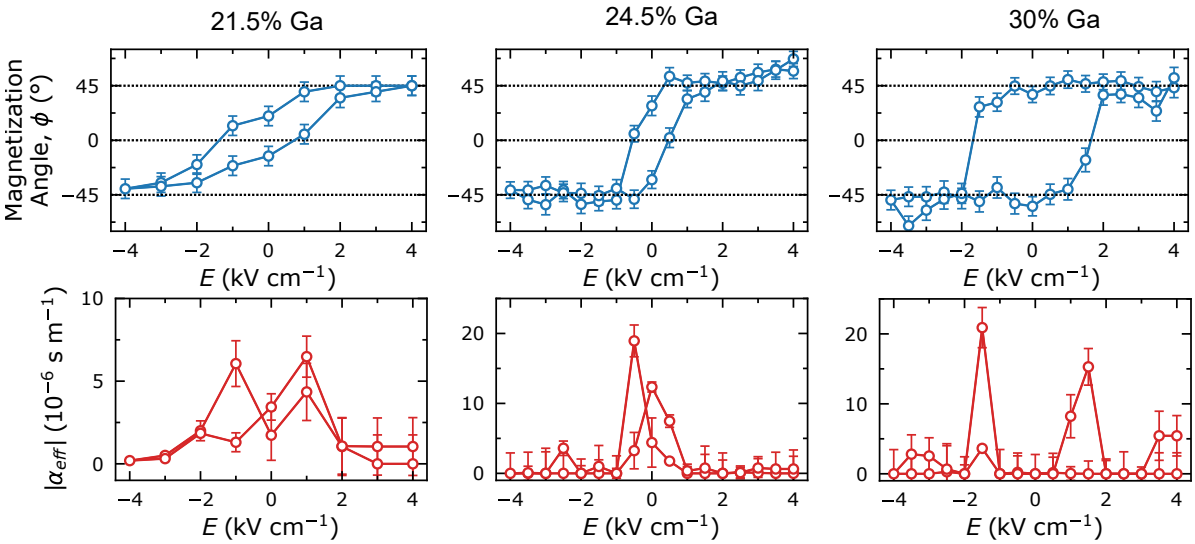

Figure 2.4: Complete magnetoelectric switching data. Example data taken at an electrical bias of up to +/-400 V across the sample, used to reconstruct the hysteresis in magnetization direction and converse magnetoelectric coefficient. AMR curves taken as a function of field angle are fit to cos(2θ) where the phase shift corresponds to the direction of magnetization, ϕ. The two saturated polarization states of the ferroelectric show a 90° phase shift in the curve, demonstrating a 90° switching of magnetization. This measurement is done by poling the magnetization along the easy axis and using low-field directional AMR to probe the rotation of the uniaxial, strain-induced anisotropy. Thus, the apparent handedness is a result of the direction used in easy-axis poling and not indicative of the device itself, but is a direct probe of the anisotropy direction. Adapted from ref. [14].

models[125, 126]. Our approach is in the same vein as these well-established methods [124, 125, 126], except that the strain is applied dynamically via the piezoelectric layer, which is a more complete analysis than the deposition of films on different static substrates to obtain different residual epitaxial strains. We extract λ_{100} from the magnetization versus electric field loop in Figure 2.4 with an analytical model to estimate the magnetoelastic energy required to switch between the easy- and hard-axes of the magnet.

Associated with an in-plane coherent magnetization switching in the crystallographic reference frame of a (001) FeGa film, the change in the total magnetic free energy density ΔF_{tot} can be approximated [128] as

$$\Delta F_{\text{tot}} = K_1 m_1^2 m_2^2 + \frac{1}{2}\mu_0 M_s^2 (N_{11} m_1^2 + N_{22} m_2^2) + B_1 (m_1^2 \epsilon_{11} + m_2^2 \epsilon_{22}) + B_2 m_1 m_2 \epsilon_{12}, \quad (2.4)$$

where K_1 = -5255, -7434, -6717 J m^{-3} for the 21.5%, 24.5%, and 30% Ga samples, respectively, is the magnetocrystalline anisotropy constant (extracted from the

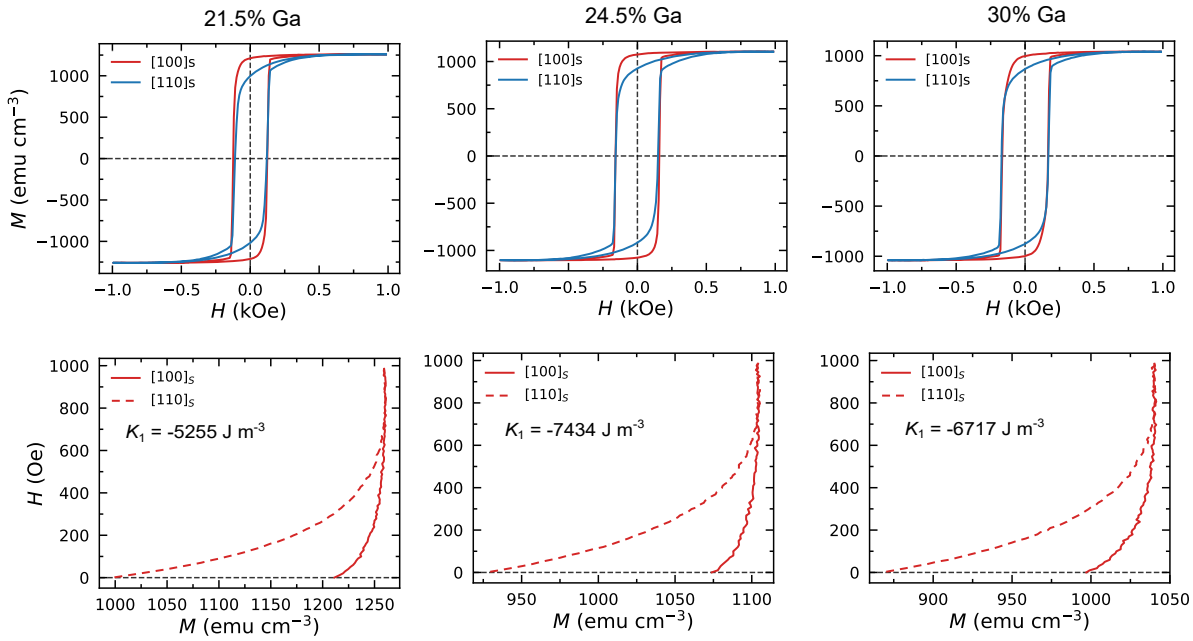

Figure 2.5: Calculation of anisotropies. Magnetic hysteresis loops of FeGa samples and schematic of the integral, $A_{ijk} = \int_{M_r}^{M_S} H dM$, used to determine the magnetic anisotropy energy [127] through $A_{110} - A_{100} = K_1/4$. The values for anisotropy energy were used in the analytical solution as the required energy produced by strain at the switching voltage. Adapted from ref. [14].

experimentally measured magnetic hysteresis loops, Figure 2.5); μ_0 is the vacuum permeability, and M_S is the saturation magnetization. For our FeGa film (10 µm x 50 µm x 15 nm in dimension) whose in-plane dimension is much larger than its thickness, the demagnetization energy difference between the short and long axes is calculated from AMR of the virgin sample to be 0.21 kJ m^{-3}, approximately 20x smaller than K_1, thus we assume the demagnetization tensor components $N_{11} \approxeq N_{22} \approxeq 0$, meaning the second term in Eq. 2.4 can be omitted. $B_1 = -1.5\lambda_{100}(c_{11} - c_{12})$ and $B_2 = -3\lambda_{111}c_{44}$ are magnetoelastic coupling coefficients (where λ_{100} and λ_{111} are magnetostrictive coefficients; c_{11}, c_{12}, and c_{44} are elastic stiffness coefficients), $m_i = \frac{M_i}{M_S}(i = 1, 2)$ are direction cosines of the magnetization vector, and $\epsilon_{11}, \epsilon_{22}, \epsilon_{12}$ are the average normal and shear strains in the (001) FeGa. Using the PMN-PT substrate as the reference system and assuming a complete strain transfer across the coherent PMN-PT/FeGa interface (which is assumed in accordance with Figure 2.1b) without loss, one has $\epsilon_{11} = \epsilon_{[1\bar{1}0]}$ and $\epsilon_{22} = \epsilon_{[110]}$.

Writing ΔF_{tot} as a function of the direction of the magnetization, β (where $m_1 = \cos\beta$, $m_2 = \sin\beta$) and minimizing $\Delta F_{tot}(\beta)$ with respect to β, we derive an analytical

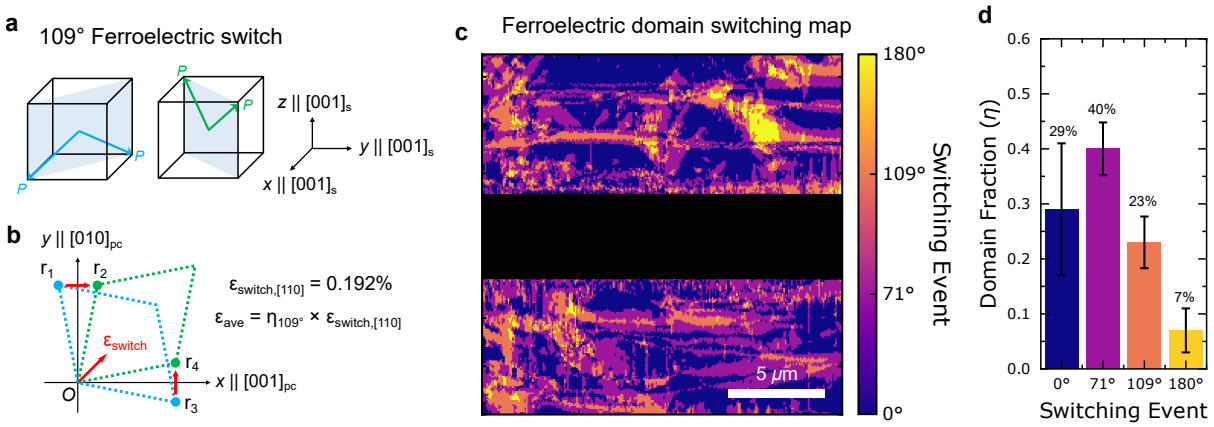

Figure 2.6: Local shear strains arising from 109° polarization switching in PMN-PT. a Polarizations within the $(110)_s$ (substrate) plane, blue, and the $(1\bar{1}0)_s$ plane, green, are associated with shear distortion in the $(001)_{pc}$ plane, **b**, indicated by the blue and green dashed frame. The corresponding shear strain arising from a 109° polarization switching can be calculated based on the coordinates of points r_i (i=1,2,3,4), where the translation from r_1 to r_2 results in a 0.192% shear strain per unit cell. This is then scaled by the fraction of ferroelectric domains that undergo a 109° switch ($\eta_{109°}$) to calculate the total strain seen by the device. **c** PFM switching map that allows us to experimentally determine $\eta_{109°}$. This map is made by overlaying PFM micrographs before switching (+4 kV cm-1) and after switching (-4 kV cm-1) and calculating the 3D switching angle per pixel. The directions of the ferroelectric vectors were determined by combining in-plane and out-of-plane piezoresponse patterns before and after rotating the sample by 90° to allow for the determination of in-plane directionality. The full data set is shown in Fig. 2.7. **d** Histogram of the switching events from 14 composite images, with standard deviations shown as error bars. The analysis indicates that 23% ±4% of the domains undergo 109°switching. Adapted from ref. [14].

formula on the orientation of the in-plane magnetization vector at equilibrium, with azimuthal direction denoted β_{eq}, as a function of in-plane strains ϵ_{ij} (i,j = 1,2).

$$\phi_{eq} = \beta_{eq} - 45^\circ = \frac{1}{2}\cos^{-1}\left(\frac{-B_1(\epsilon_{[110]} - \epsilon_{[1\bar{1}0]})}{K_1}\right) - 45^\circ \tag{2.5}$$

Due to the 45° lattice misalignment between the (100) planes of the FeGa film and PMN-PT substrate, $\beta = \phi + 45^\circ$ (see definition of ϕ in Figure 2.1c). Through experimental results, we observe that the bound values for ϕ of +/- 45° are achieved at electric fields at or below $E = +/-4$ kV cm^{-1} (Figure 2.3c and 2.4), we can conclude that here the heterostructure achieves a strain of state $\epsilon_{[110]} - \epsilon_{[1\bar{1}0]} = K_1/B_1$, where the magnetoelastic energy B_1 can overcome the natural anisotropy K_1 and force the magnetization along the hard axis/direction of strain. We can then use the definition of λ_{100} above with Equation 2.5 to extract magnetostriction, using the strain $\epsilon_{[110]} - \epsilon_{[1\bar{1}0]}$ at $E = +/-4$ kV cm^{-1} and the mechanical pre-factor $\frac{1}{2}(c_{11} - c_{12})$.

Mechanistically, it has been observed that a hysteretic shear strain is created in (001)-oriented PMN-PT crystals when the local polarization, P, switches by 109° (Figure 2.6a) from down (E = –4 kV cm^{-1}) to up (E = 4 kV cm^{-1}) [129, 130, 87]. This distortion can be more clearly visualized by a top-down projection of the unit cell, which corresponds to the plane of device (Figure 2.6b). Using the lattice parameters and distortion angle of rhombohedral PMN-PT [131], we analytically calculate this shear strain to be 0.192%, which corresponds to biaxial normal strains in the (001) plane of FeGa along the [110] and [1$\bar{1}$0] substrate directions, (ϵ_{switch} = 0.192%). This calculation is further detailed in Ref. [14]. We note, however, that that this ϵ_{switch} only describes the local deformation from the 109° switching of one single ferroelectric domain of the underlying PMN-PT [132]. The average strain seen by the FeGa device is this strain multiplied by the fraction of domains that undergo 109° switching, η_{109}, thus $\epsilon_{\text{ave}} = \epsilon_{[110]} - \epsilon_{[1\bar{1}0]} = \eta_{109}\epsilon_{\text{switch}}$ (Figure 2.6c). We experimentally measure this fraction η_{109} by comparing composite piezoelectric force microscopy (PFM) micrographs at fields both before and after the magnetoelectric switching event. An example of this switching map is shown in Figure 2.6d. From histograms of the counted switching fraction (Figure 2.6e), we see that $\eta_{109} \approxeq 20\%$ in all three cases, consistent with published values in (001) PMN-PT substrate [129, 130, 87] determined through in situ Reciprocal Space Mapping.

In bulk FeGa, the pre-factor $\frac{1}{2}(c_{11} - c_{12})$ can range from 28 GPa to 7 GPa due to the variation of the Ga composition [123, 134] (from 17% to 27.2%). $\frac{1}{2}(c_{11} - c_{12})$ values from our own DFT simulations of disordered FeGa agree with these published values to within the error bar of the simulation, justifying their use here for our analytical solution (Figure 2.8). With these values of $\frac{1}{2}(c_{11} - c_{12})$, we calculate a λ_{100} ranging between 300 ppm (21.5% Ga) and 4000 ppm (30% Ga, shown in Figure 2.9), significantly higher than reported bulk values [123] where $\lambda_{100} \approxeq 150$ ppm. This result demonstrates our ability to stabilize the disordered A2 phase in our system far beyond the bulk threshold [73]. Furthermore, we plot our extracted values against the λ_{100} values for bulk FeGa, noting that our peak value of magnetostriction coincides with the lattice softening at approximately 30% Ga. This implies that we are not only able

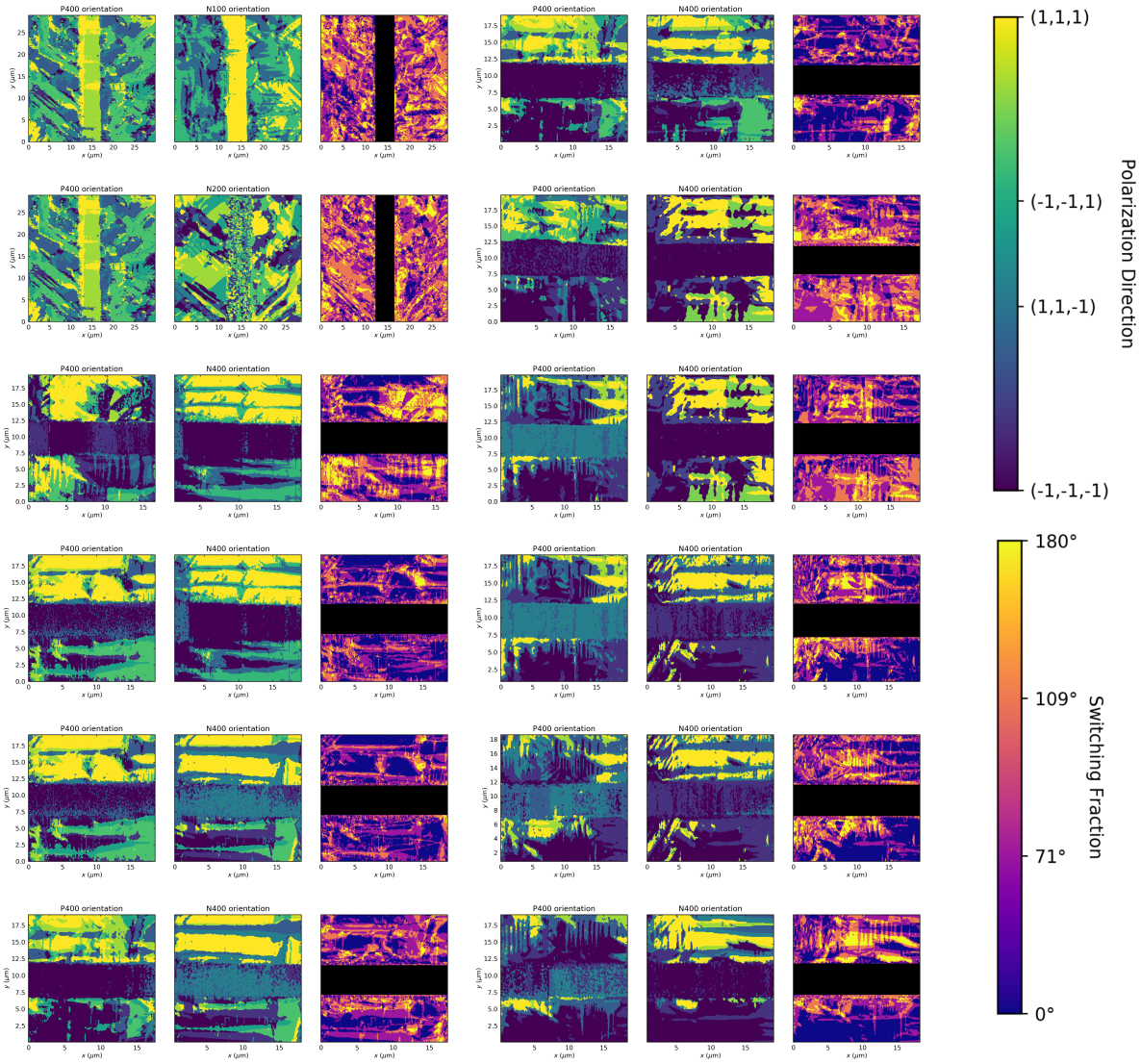

Figure 2.7: Domain fraction of ferroelectric switching. PFM switching maps that allows for experimental determination of η_{109°. This map is made by overlaying PFM micrographs before switching (+4 kV cm^{-1}) and after switching -4 kV cm^{-1}) and calculating the 3D switching angle per pixel. The directions of the ferroelectric vectors were determined by combining in-plane and out-of-plane piezoresponse patterns before and after rotating the sample by 90° to allow for the determination of in-plane directionality. Adapted from ref. [14].

to prevent the formation of the parasitic intermetallic phase [72], but by engineering disorder in the ally we leverage the inherent phase space to reach record values. Comparing these numbers to existing magnetostrictive materials in Figure 2.9b, we see that our peak values are 2x higher than top-performing, rare-earth-based magnetostrictive alloys. We note that this enormous enhancement of the magnetostriction is largely a function of the mechanical coefficients, as the magnetoelastic energy, B_1, remains largely invariant.

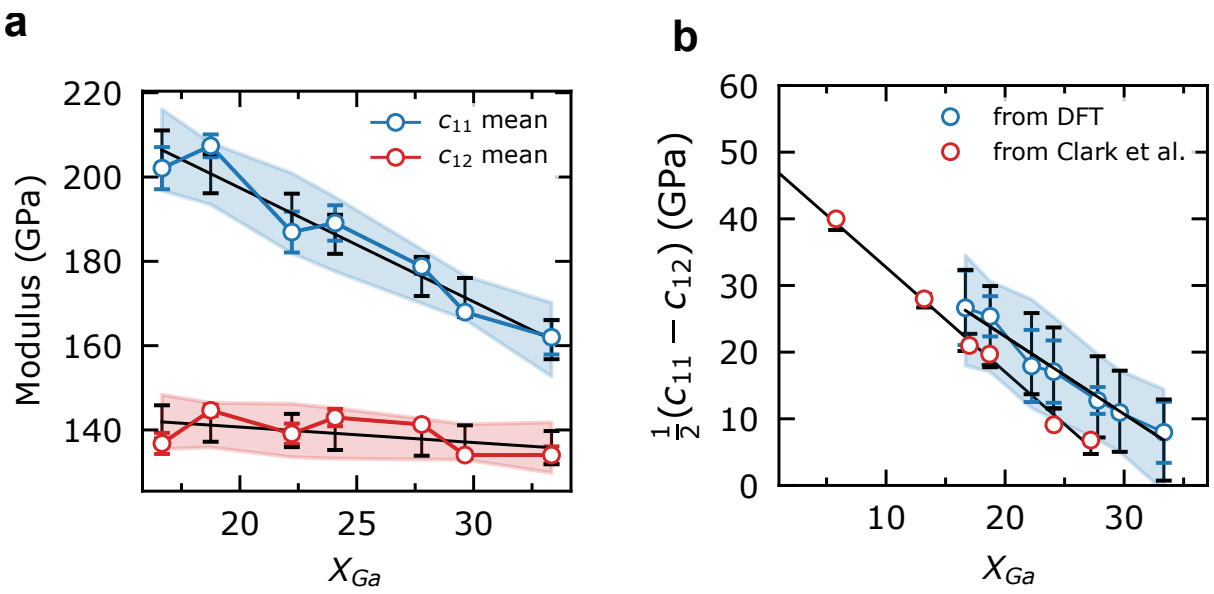

Figure 2.8: Density functional theory simulation of shear modulus. a Simulated stiffness coefficients c_{11} and c_{12} from DFT of solid solution FeGa alloys with varying Ga composition. The blue error bars correspond to the error of the calculation, the black error bars are one standard error of the linear fit, and the shaded area is the sum of the errors fixed about the trendline. **b** Comparison of the calculated shear modulus values to bulk data extracted from ref [123]. The error bars correspond to the sum of the same quantities in part **a**, propagated through to $\frac{1}{2}(c_{11}-c_{12})$. Our device is operated at room temperature, so the addition of temperature to the DFT results is simulated using a linear regression of compositionally dependent c_{11}, c_{12} data from ref. [133]. Because 1) the trend of the bulk values are replicated extremely well, 2) the bulk data is within the error bars of the DFT calculation, and 3) experimental values should be more precise than DFT results, the use of the experimental bulk mechanical values is justified for the calculation even though the bulk material is in a different phase. Adapted from ref. [14].

The primary sources of error in the calculation of λ_{100} are 1) the magnetocrystalline anisotropy, 2) the values for strain, and 3) the stiffness tensor components c_{11} and c_{12}. For the anisotropy constant K_1, a 5% relative error is appropriate from tool calibration/misalignment. Regarding the switching fraction, we can empirically determine the uncertainty by comparison to bulk values. In refs. [129, 130], the authors report 20% 109° switching and ref. [87] reports 26% switching. Including our values, the standard deviation σ_η = 2.6%, which is used to calculate the error bars in λ. We use the bulk values of c_{11} and c_{12} because we believe that they present a more accurate estimate of the real stiffness coefficients than can be obtained from DFT calculations. While the DFT reproduces the trend and approximate order of magnitude well, the values themselves may not be accurate, motivating us to pull more precise values from literature. As no uncertainty values are reported in ref. [123], where we obtain the c_{11}, c_{12} values, we use the standard error of the linear trendline in Figure

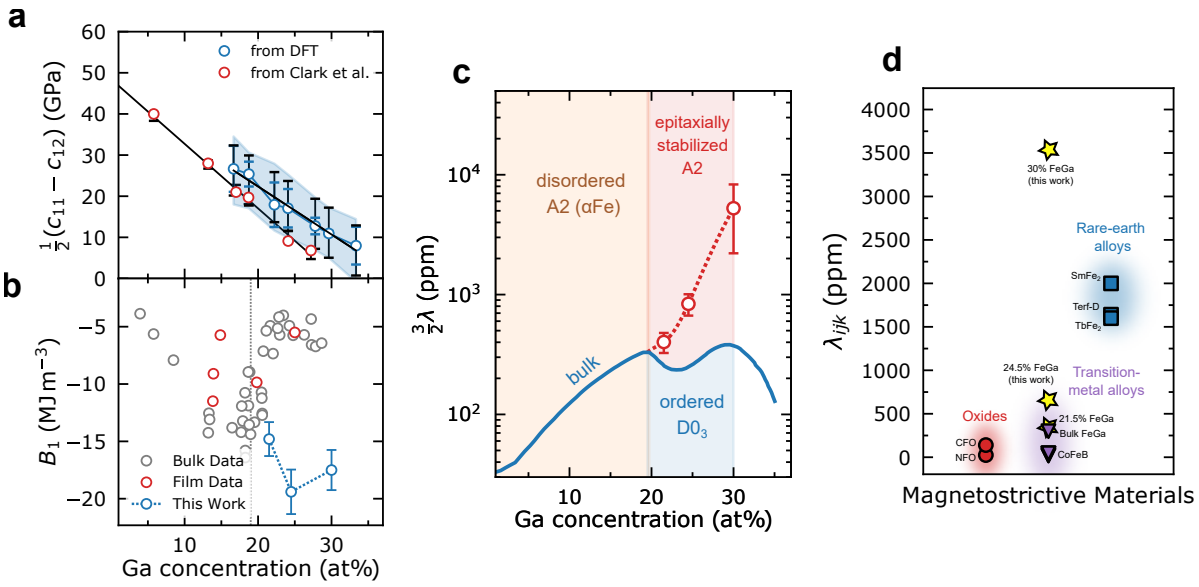

Figure 2.9: Enhanced magnetostriction coefficient through epitaxial stabilization. a Plot of mechanical coefficient $\frac{1}{2}(c_{11} - c_{12})$ extracted from literature (red) and simulated here with DFT (blue). Both data sets follow approximately the same trend and show no deviation from the linear trend following the 19% phase limit. Literature values are from ref. [133]. **b** Plot of magnetoelastic coefficients (B_1) taken from previous thin film (red) and bulk (grey) works compared to our measured values. We note that in previous works, there is a sharp decline in B_1 following the phase change at 19% Ga (dotted line), which we do not observe. Bulk values (grey) are from refs. [123, 122] and film (red) values are from ref. [135]. **c** The extracted magnetostriction values as a function of Ga concentration with our values (red, open circles) compared to the measured bulk coefficients (blue) from ref. [123]. The values from this work are plotted as $\frac{3}{2}\lambda_{100}$ to facilitate comparison with the bulk, polycrystalline values. Above 19% Ga, we do not observe a decrease in the magnetostriction associated with the formation of the ordered D0$_3$ phase as we extend the regime of the disordered A2 phase via epitaxial stabilization. As the concentration approaches the second phase change at 30% Ga, the shear modulus $c_{11} - c_{12}$ approaches 0, leading to extremely large values of the magnetostriction. **d** Comparison of the magnetostriction coefficients from this work to other magnetostrictive materials. The largest magnetostrictive tensor component λ_{ijk} of each respective material is plotted here for ease of comparison. Comparative data in **d** is from refs. [136, 137, 138, 139, 140, 97, 141, 142, 143]. Adapted from ref. [14].

2.8 as the error for $(c_{11} - c_{22})/2$. The uncertainty in λ_{100} can then be defined as:

$$\sigma_\lambda^2 = \left[\frac{1}{3}\frac{K_1}{\varepsilon}\frac{1}{c^2}\right]^2 \sigma_c^2 + \left[\frac{1}{3c\varepsilon}\right]^2 \sigma_{K_1}^2 + \left[\frac{1}{3}\frac{K_1}{c}\frac{1}{\varepsilon^2}\right]^2 \sigma_\varepsilon^2 \tag{2.6}$$

where $\varepsilon = \eta\varepsilon_{\text{switch}}$ and $c = \frac{c_{11}-c_{12}}{2}$

In this section, we have discussed how inducing disorder in a ferroic material can significantly enhance functional properties. By using epitaxy to stabilize the disordered phase of FeGa, we increase the magnetostriction to record values. It is not

completely understood in this case why disorder allows us to achieve these values, but several theoretical works posit that it is due to better orbital mixing between Fe and Ga in the solid solution phase, tending towards mechanical isotropy, a larger spin-orbit coupling, and potentially unique electronic features in the band landscape [72, 74, 99]. Using disorder as a parameter to tune ferroic properties is normal in materials science, perhaps most obviously in relaxor ferroelectrics, where properties are achieved through frustration of the ferroelectric order parameter [144, 145]. The use of disorder to illicit completely new chemical and functional phenomena, however, is a rathesr novel idea, with the field of entropy stabilized/high entropy materials appearing only around a decade ago. Entropy stabilized/high entropy materials are highly disordered many-component crystals, where the phase may be only allowed through the entropy term of the free energy of formation. This idea, that entropy can be tuned to engineer new phases and properties of materials, particularly ferroic oxides, is an exciting idea that motivates the next few sections.

Chapter 3:

Novel Phases Enabled by Disorder

High-entropy materials are often defined by their large entropy of mixing (ΔS in $\Delta G = \Delta H - T\Delta S$) stemming from a large number (i) of constituent species where the entropy ΔS_{conf} goes as $k_B \sum_1^N x_i \ln(x_i)$, N being the number of species and x_i their compositions. Potentially the most exciting prospect of these materials, is that this entropic term can actually override a positive enthalpy of mixing, allowing access of novel phases. Pioneering work by Rost et al. [15] demonstrated that this is the case in the multicomponent entropy-stabilized rocksalt oxide (MgCoNiCuZn)O, which emerges as a solid solution from a phase separated rocksalt-spinel mixture at high temperatures. Experimentally, the evidence for entropic stabilization can come from 3 main observations. 1. The transition temperature of the phase change follows the resulting change in entropy as the relative compositions of the constituent elements are varied. 2. The phase change is reversible and endothermic. 3. The entropy-stabilized phase is chemically homogeneous.

This is an exciting development, because the implication is that entropy-engineering can be use to force normally immiscible species into novel oxide phases. In the study by Rost et al. it was observed that typically immiscible concentrations of cationic species, namely Cu and Zn in the case of the rock salt, can be dissolved into the crystal in atypical coordination. Neither Cu^{2+} nor Zn^{2+} is happy in an octahedral environment, i.e. rock salt, in the observed concentrations. Figure 3.2a illustrates this observation for the case of (MgCoNiCuZn)O, where the solubility of Cu^{2+} and Zn^{2+}

is enhanced in the ESO rocksalt crystal, in contrast to the tetrahedral coordination of their equilibrium binary phases. This ability to realize new phases and stereochemistry, along with the control of disorder, has opened new space for the synthesis and design of oxide materials.

Prior to the seminal work in 2015 that nucleated the high-entropy oxide field [15], there were only a few reports exploring high-entropy transition metal nitrides as an extension of the metals community [146, 147, 148]. This is now no longer the case, as the synthesis of new oxide compositions in pursuit of novel structural, chemical, and electronic functionalities is proving to be an exciting and rapidly growing field. This is shown in figure 3.1a, which plots the number of publications on the topic, circa early 2021, which were found using title keywords "high-entropy" or "entropy-stabilized" and "oxides" or "ceramics" in Web of Science. The number of publications has increased exponentially since inception, which is a clear indicator of its potential impact.

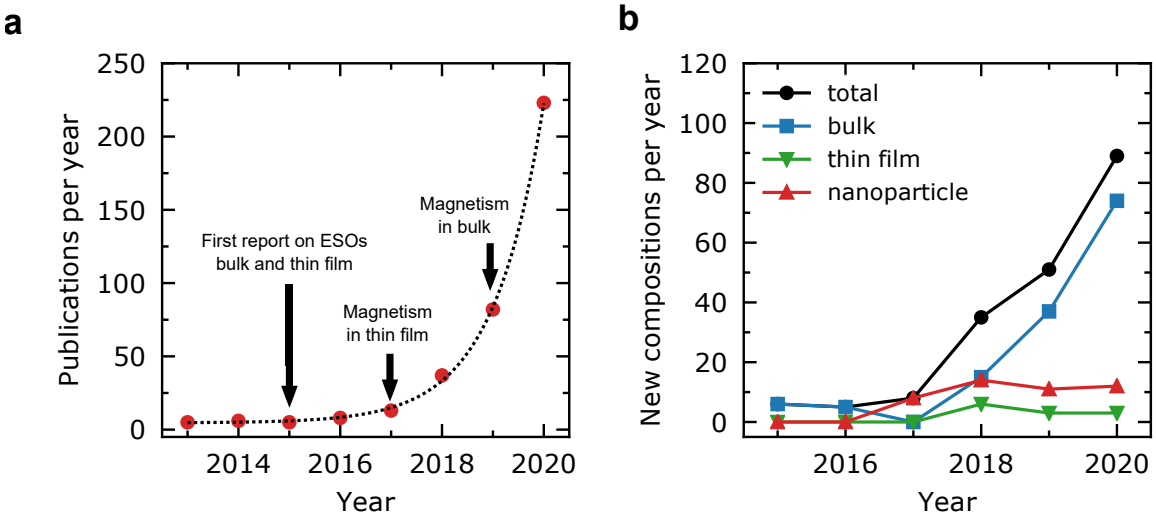

Figure 3.1: Growth of the HEO field. a Publications per year using title keywords "high-entropy" or "entropy-stabilized" and "ceramics" or "oxides" retrieved from Web of Science. The dashed line is a fit of the data to an exponential function, $y = Aexp(Bx)$. **b** Number of new high entropy oxide compositions over time and broken down by synthesis method. Data for part **b** is from refs [149, 150, 151, 152, 153, 154, 155, 156, 157, 158, 159, 160, 161, 162, 163], compositions with 3 components or less are not counted. Figure adapted from ref [164]

3.1 Unique Features and Prospects for HEOs

The first (MgCoNiCuZn)O entropy-stabilized oxide studied by Rost et al. was synthesized by traditional solid-state methods (mill, press, sinter), with thermodynamic stabilization of the equimolar phase occurring at approximately 900 °C [15]. Bulk techniques have since been used to synthesize a number of new HEO compositions and currently remains the most pervasive method for the discovery of novel phases (Figure 3.1b). This technique may, however, be limited in the long run by thermodynamic considerations as certain compositions may require static sintering temperatures above what is accessible at furnace conditions. Further, these materials must be rapidly quenched from high temperature to maintain the phase at room temperature. For this reason, non-equilibrium synthesis processes, such as nanoparticle synthesis or PVD, may be highly preferable for the discovery of new phases. Indeed, these are also popular methods for phase stabilization and have yielded a number of compositions not achievable in bulk due to the kinetic fixing of the synthesis [110, 111, 112, 108]. As the number of new material compositions has increased dramatically, the number of thin film reports have grown at a much slower rate (Figure 3.1b). While films are the least represented in the literature currently, we do not see this as the case moving forward.

In the same initial work by Rost et al., it was demonstrated that single crystal thin films of (MgCoNiCuZn)O could be deposited on (001)-oriented MgO substrates by pulsed laser deposition (PLD) [15], which was later further corroborated by other groups [11, 13]. Despite the large estimated strains (up to 4.5% in some cases [11]) and anticipated lattice disorder, (MgCoNiCuZn)O and compositional variant films on MgO substrates are incredibly high quality [108, 11, 165, 12] with commensurate epitaxy and rocking curves as narrow as that of the underlying substrate [15, 11]. In this vein, a significant advantage of HEOs remains their structural tunability observed with composition and kinetics [11, 166, 167, 168] and, at least for ESOs, the ability to be grown on a variety of substrates [110, 168], including amorphous materials. A laser ablation deposition study by Kotsonis and colleagues observed that the kinetic energy of species (1s-10s of eV, $T_{\text{eff}} \approxeq 10^4 - 10^5$ K) dictated whether the film was in the ESO phase or the phase-segregated rocksalt-spinel mixture [110]. Their findings suggest

that the extreme kinetic energy and quenching associated with PVD will further open the composition space for ESOs relative to near-equilibrium bulk techniques. The use of thin film growth techniques broadens the stabilization space, where films can be deposited on a wide variety of substrates and the need for a large effective quench favors the low temperature deposition for BEOL (back-end of line) compatibility.

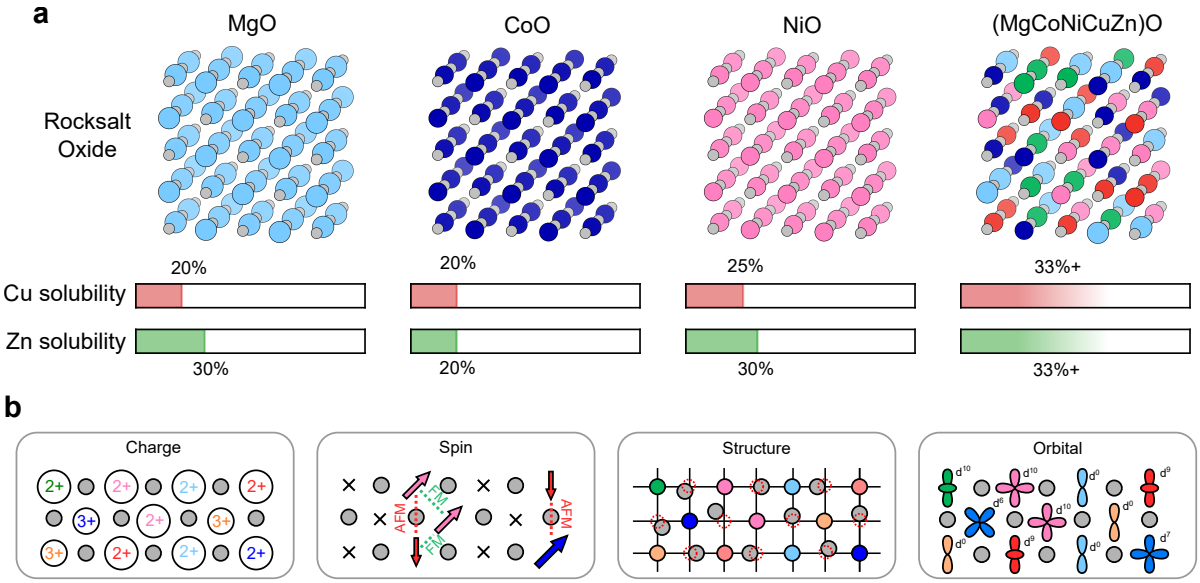

Figure 3.2: Degrees of freedom in HEOs. a Illustration of the enhanced solubility of cations into ESOs. The solubility of Cu and Zn, both cations with different preferred coordination (tetrahedral) and crystal structure (tenorite and wurtzite, respectively), are shown by the solubility bars for the binary rocksalt and ESO solvent systems. The solubility is significantly enhanced in the ESO. Even more so, the phase diagram of (MgCoNiCuZn)O has not been investigated, so the solubility limit may be even higher than yet reported [15]. The solubilities given are taken from bulk phase diagrams [169, 170, 171, 172, 173] at 1000° C, the approximate stabilization temperature of (MgCoNiCuZn)O with 33% Cu or Zn. **b** Illustration of the disorder in HEOs, where new properties can be engineered and tuned using the interplay between local charge, spin, structural, and orbital degrees of freedom. Figure adapted from ref [164].

Due to the enhanced solubility inherent in ESOs, researchers have new tools to study competing internal charge, spin, structural, and orbital order/disorders that can develop new functional frustrations (e.g. the phenomena that occurs in relaxor ferroelectrics). Using these new degrees of freedom, materials can be engineered with new properties arising from different disordered length scales. For instance, the structural distortions caused by Jahn-Teller active Cu^{2+} can drive oxidation state changes in other cations, which in turn effects the spin-dependent properties [12]. The significant tunability of structure and chemistry coupled with recent observations of functionality

in HEO/ESOs [12, 116, 117], opens opportunities for studying the interplay between charge, spin, lattice, and orbital degrees of freedom in highly disordered crystalline materials. For the remainder of this chapter, I will focus on summarizing the research in the field related to these ideas with a primary focus on dielectric and magnetic behavior.

3.2 Disorder-Driven Properties

3.2.1 Dielectricity and Charge-Lattice Coupling

Dielectric and ferroelectric oxides have long been a group of technologically relevant materials that have a unique relationship with chemical disorder. In many cases, it is desirable for these materials to exist in a very precipitous phase space to maximize the ferroelectric and piezoelectric response. This is often done through chemical substitution in lead-based perovskites such as PZT ($Pb(ZrTi)O_3$), PZN ($Pb(ZrNb)O_3$), and PMN-PT ($Pb(MnNb)O_3$-$PbTiO_3$) to promote competition between ferroelectric phases and/or crystalline phases [174, 175, 176, 145]. This is desirable because lattice softening at the phase boundary increases the polarizability and charge-lattice coupling of the crystal, and local chemistry can modify the phase stability of the oxide [177, 178]. Recently, modern techniques such as diffuse neutron scattering, a technique able to probe local, inelastic scattering events, has been used to show the even more important role of disorder in relaxor ferroelectrics due to the formation of polar nanoregions (PNR) [179]. PNR form due to frustration from competing ferroelectric orders in the material (Figure 3.3) that significantly increase the piezoelectric response of the crystal due to coupling with lattice phonons [174, 180] and polarization of the nearby ferroelectric matrix [181]. These two effects, phase instability and frustrated ferroic orders, are clear possibilities in high entropy oxides where the material can conceivably be made from constituent species with differing preferred crystal structures and ferroic orders, while being coerced into a metastable phase by entropy. Illustrated in Figure 3.3d, the inclusion of Jahn-Teller active Cu^{2+} cations works to create local structural distortions because of the frustrated stereochemistry. This results in a crystal that is disordered on an atomic scale, potentially allowing contributions to a dielectric response. This

effect has been explored further in regards to the magnetism of the oxides [12], which will be discussed further below.

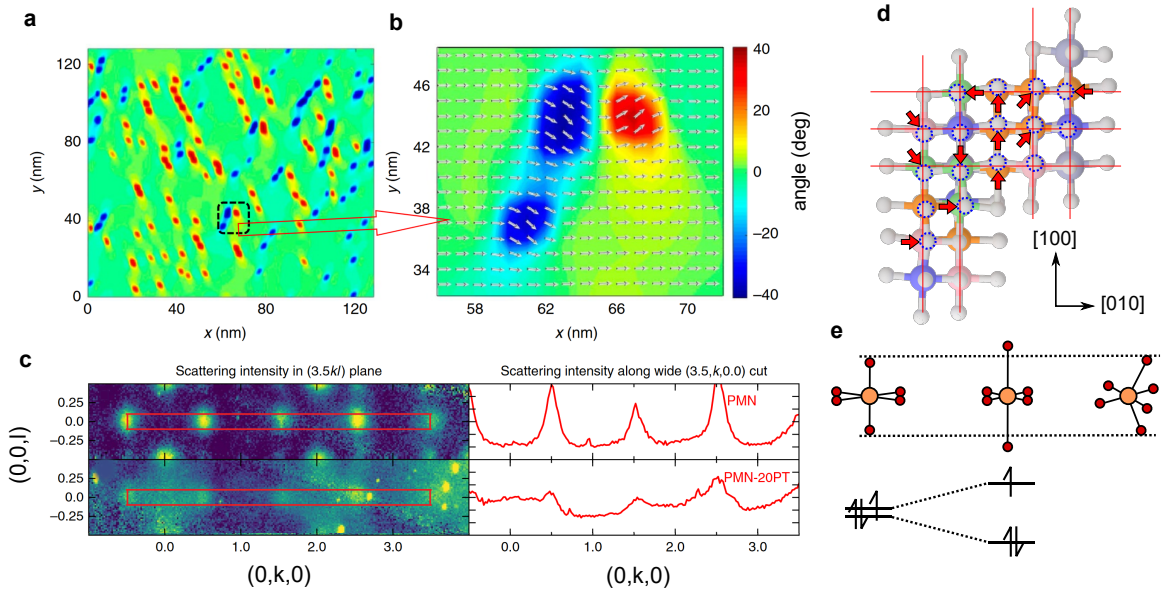

Figure 3.3: Frustrated ferroelectricity. **a** and **b** Phase field simulation of polar nanoregions (PNR) arising in PMN-PT due to frustration from antiferroelectric and ferroelectric orders. The PNR show up as polar particles that are separate from the ferroelectric matrix, which couple to it to increase local polarizability. **c** Diffuse neutron scattering data showing the local antiferroelectric response in PMN-PT, demonstrating experimentally that relaxor behavior is a result of competition between ferroelectric and antiferroelectric orders. **d** DFT calculated structure showing the random structural disorder and lattice frustration of (MgCoNiCuZn)O, where the distortions of the oxygen atoms from the ideal planes (red lines) are highlighted by the red arrows. **e** Illustration showing an intuitive guide to how the Jahn-Teller distortion of Cu^{2+} creates structural defects in the crystal. Parts **a,b** from ref [181]. Part **c** from ref [174]. Part **d** from ref [12]. Figure adapted from ref [164].

The extreme tunability of the structural lattice in rocksalt ESOs has been demonstrated [12, 182, 183] with the systematic inclusion of Jahn-Teller active species into rocksalt (MgCoNiCuZn)O, where the inclusion of Cu^{2+} cations works to frustrate the stereochemistry. This effect generates disorder on local and global scales, observable through density functional theory simulations [12, 182] (Figure 3.4a,b), analysis of bulk diffraction intensities [183] (Figure 3.4c), and local scattering effects [12]. Particularly in bulk ceramics, the Jahn-Teller effect imparts a rhombohedral or tetragonal distortion to the lattice, which is seen as a decrease in intensity of the highest symmetry (200 planes) diffraction peaks, which will be most strongly affected as local symmetry is low-

ered. Beyond investigations of the parent rocksalt, structural tunability has also been observed in perovskite HEO Ba(ZrSnTiHfNb)O_3, which is subject to random structural distortions due to competing cation sizes [168] and possible preferred local coordinations. The component phases are a selection of competing displacive ferroelectric ($BaTiO_3$) and well known paraelectric ($BaZrO_3$, $BaHfO_3$) oxides, which may drive frustrated behavior. Raman signatures of thin film Ba(ZrSnTiHfNb)O_3 show identifying features of random atomic distortions [168] which, in $BaTiO_3$ based ferroelectrics, can be correlated to relaxor-like characteristics [184]. A manifestation of charge-lattice coupling in these materials is the exceedingly low thermal transport that approaches the amorphous limit in phase pure, crystalline samples [110, 185, 186, 115]. The entropy will favor dense phases, which could be linked to short stiff bonds, but uses charge, bond, and mass disorder to quench the thermal conductivity. In HEOs, local chemical and structural disorder, e.g. the frustrated stereochemistry of Cu^{2+} sites, work to scatter phonons and result in short mean-free paths [186] that drop the thermal conductivity to values close to 2 W m^{-1} K^{-1} at room temperature in high-quality, crystalline specimens. Through a combination of experimental extended X-Ray fine structure (EXAFS) measurements and charge distributions found from density functional theory (DFT) calculations [187], the authors report that the anomalously low thermal conductivity is dominated by Rayleigh scattering from cation sites of differing bond and charge states. From EXAFS, a distortion of the O octahedra about the Co cation sites was observed, which agrees with the observation of charge disorder seen on the Co cation in other works [12, 115] and is complemented by a similar observation of distortion about the Cu site in thin films [165]. All of these works agree that the structural disorder seen in these materials is concentrated on the oxygen sublattice, with the cations remaining in their approximate equilibrium positions. Recent reports of ultra-low thermal conductivity have been observed in other entropy-stabilized crystal structures [188, 189] beyond the 5-component rock salt oxides and even other high entropy systems [185, 190], which indicates that it may be an intrinsic and emergent property caused by the additional degrees of freedom (charge and structural disorder) in high-entropy materials.

ESOs have indicated that they their structure may be extremely sensitive to small

changes in chemistry [11] and deposition conditions [115], with the lattice constant of deposited films shifting by as much as several % strain. This was seen with our films in ref. [11] with small changes in the concentration of Co cations, and has recently been observed by Kotsonis et al. with constant composition, but differing deposition temperatures ($T = 300^\circ - 600^\circ$ C). In samples deposited at low temperatures, the films display tetragonally-distorted lattice constants with $c > a$, and sample deposited at high temperatures the opposite is true, $c < a$. It was determined that the the Co oxidation state is the primary driver of this large structural transition, agreeing with other results [11, 12], where low temperature films contain primarily Co^{3+} and high temperature films are almost pure Co^{2+}. This effect clearly demonstrates the large charge-lattice coupling inherent to ESOs, and belies the large degree of stereochemical control with relatively small processing changes.

Recently, Brahlek et al. have reported control of concerted orthorhombic structural distortions in La(CrMnFeCoNi)O_3 due to competing phases from the constituent B-site cations [191]. Of the bulk oxides, $LaCrO_3$, $LaMnO_3$, and $LaFeO_3$ are orthorhombic, while $LaCoO_3$ and $LaNiO_3$ are rhombohedral due to differences in octahedral tilt angles. This concerted distortion has also been seen in high entropy nickelate (LaPrNdSmEu)NiO_3, in which the material goes through a low temperature metal-insulator-transition [167] due to a concerted octahedral rotation, much like the parent rare earth nickelates with the exception of $LaNiO_3$. This transition is structural in nature and agrees with the rule-of-mixtures estimation from the high entropy A-site, importantly showing that existing site-specific correlated phenomena can be preserved in the presence of entropy engineering. The transition, however, is broadened in temperature compared to the parent material, potentially indicating the presence of local variances of the concerted distortion and associated metal-insulator-transition. These works demonstrate that entropy, beyond the creation of new phases, can be a valuable knob to tune structural correlations.

Relatively early in the history of entropy-stabilized oxides, Berardan et al. reported on the observation of a large dielectric constant (order of 104) in both (MgCoNiCuZn)O and select compositional variations containing Li and Ga [16]. In these studies, how-

ever, the largest dielectric constant lies at frequencies of 1 kHz or less with temperature dependent loss tangents on the order of 1-10 at room temperature. This work was followed up by the same group reporting on the superionic conduction of Li in these same compositions [17], which they attribute to large space created in the lattice by uncorrelated atomic displacements. Since the observation of superionic transport, other works have explored the use of ESOs for battery materials [192, 193, 194, 195] and catalysts [196, 197], motivated by the material's disordered surface structure and anomalous thermodynamics. More recent studies on the dielectric behavior in perovskite oxides have shown dielectric constants on the order of 40-80 up to approximately 106 Hz with much lower loss tangents [163], in the neighborhood of 0.1.

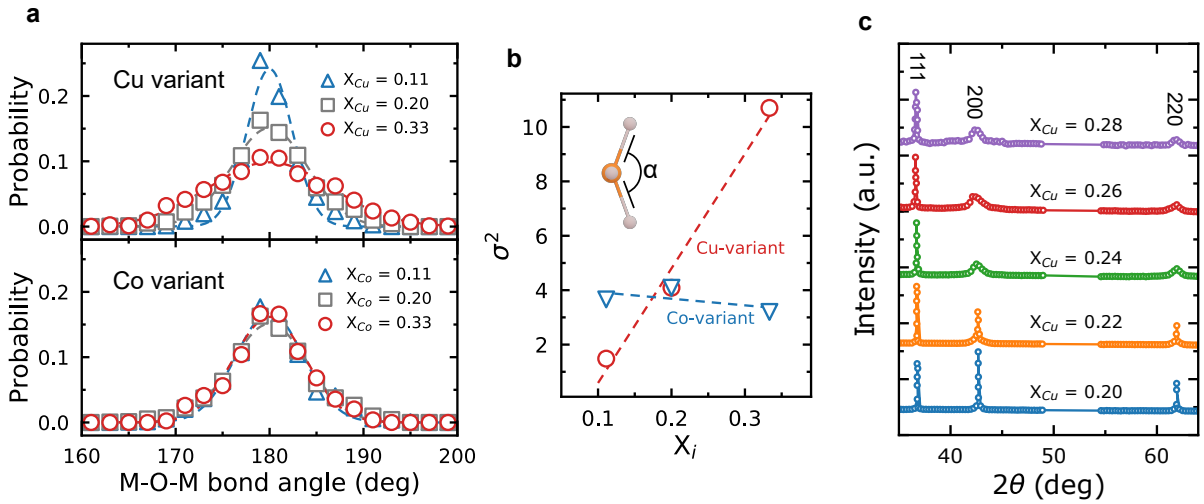

Figure 3.4: Lattice frustration in HEOs. a Histogram of the M-O-M bond angle α from DFT calculations, showing the change in structural frustration as a function of Cu cation concentration (X_{Cu}), a Jahn-Teller active cation that will force rhombohedral distortions in the rock salt lattice. **b** Plot of the M-O-M bond angle variance, demonstrating the tunability of the structure via stereochemistry of the cation site. **c** X-ray diffraction pattern of bulk (MgCoNiCu$_x$Zn)O high entropy oxides while varying the relative composition of Cu. As X_{Cu} increases, the ratio between the 111 and high-symmetry 200 diffraction peaks changes due to the Jahn-Teller distortion effecting the highest symmetry reflection. Parts **a,b** from ref [12]. Part **c** from ref [183]. Figure adapted from ref [164].

Other recent bulk studies on ESOs have explored the possibility that this electronic behavior is partially mediated by oxygen or cation vacancy formation, and the role of such defects in the high entropy system [198, 199, 200]. Grzesik and colleagues have concluded that the (MgCoNiCuZn)O ESO lattice can harbor a large number of oxygen defects (up to 7% at equilibrium) which are localized to the cation species which have

the largest strain fields and unfavorable local thermodynamics [198, 199]. These high number of defects could work in concert with local structural disorder to create sites for electronic and ionic transport, helping to explain the material's conductive-leaning transport properties. This is in agreement with previous work from the high entropy alloy community, which, working with amorphous oxide materials naturally containing a significant number of defects, has observed a very low electrical resistivity [201, 202]. Further work on (CeLaPrSmY)O_2 high entropy fluorite has demonstrated that the band gap and crystalline structure of the material can be tuned via the oxygen stoichiometry due to hybridization of the O and rare earth atoms [203].

3.2.2 Magnetism

In oxides, the magnetic exchange between two transition metal cations involves the nonmagnetic oxygen anion as an intermediate. The atomic magnetic moments are realized by the partially filled 3i shell and Hund's exchange. However, the interatomic exchange is mediated through the fully occupied 2*p* shells of the doubly charged O^{2-} anions. The interatomic exchange occurs by the hopping or virtual hopping of electrons between the filled 2*p* shell of the oxygen and the partially occupied 3*d* shell of the transition metal, these are the so-called double exchange and superexchange interactions, respectively. Double exchange can be found in mixed-valence manganites and leads to ferromagnetic order and conduction [204]. However, superexchange leads to antiferromagnetic or ferrimagnetic insulators which is most prevalent in magnetic oxides. Thus, the superexchange interaction will primarily be our focus. The strength and sign of which is dependent on the degree of 3*d* orbital filling of the metal cations and the bond angle between the 2*p* and 3*d* shells as described by Goodenough-Kanamori-Anderson rules [204, 205, 206]. Perhaps most critically for our discussion, as the superexchange interaction is short-range, the emergence of magnetic order is critically dependent on the density of magnetic cations, which must exceed a percolation threshold, and bonding, which can be frustrated by the lattice topology and disorder [12, 207, 113, 208]. Naturally, the magnetic dilution can be changed with composition but the local and global structure of high-entropy oxides can also be tuned through deposition conditions and composition, thus providing pathways to investigate and tune

the magnets and roles of disorder in high-entropy systems. Frustrated magnetism has attracted recent study due to the computational applications and rich physics of spin glasses [209, 210], spin ices [9, 211], and spin liquids [212, 213]. These phases generally arise due to strong localization of electrons and competing magnetic interactions, such as in a trigonal lattice or between ferromagnetic-antiferromagnetic nearest neighbor exchange [214]. Being a disorder driven physical property, this presents an opportunity for HEOs, as these have already been shown to present concerted phenomena [191], as well as show strongly localized physics [215] and frustrated magnetic interactions [12, 116, 216]. Below we review recent work that investigates the magnetic ordering and frustration in magnetically dilute entropy-stabilized oxides and its tunability with magnetic dilution and disorder.

The rocksalt (MgCoNiCuZn)O entropy-stabilized oxide consists of three magnetic binary constituents (monoclinically-distorted rocksalt CoO, rhombohedrally-distorted rocksalt NiO, and tenorite/rocksalt CuO). The magnetic order in binary rocksalt oxides with more than half-filled 3*d*-shells is typically antiferromagnetic due to the strong antiferromagnetic superexchange interaction along the 180° metal-oxygen-metal bonds [204]. This order, however, depends critically on the density of magnetic cations exceeding a percolation threshold and frustration of the antiferromagnetic bonding by lattice topology. In fact, rocksalt CoO, NiO, and CuO are all antiferromagnetic with a strong antiferromagnetic interaction along the 180° metal-oxygen-metal bonds, while tenorite CuO is monoclinic with long range antiferromagnetic order. As only three of the five cations are magnetic and the disorder of the oxygen sublattice due to cation radii differences and the Jahn-Teller distortion from the Cu^{2+} cation [12, 182, 183] (Figure 3.4a,b), the anticipated ground state magnetic order becomes unclear.

Further work from two independent research teams on bulk polycrystalline specimens of (MgCoNiCuZn)O using neutron, X-ray synchrotron, and magnetometry measurements corroborated the prior work and shed new light on the details of the ordering [116, 117]. Neutron diffraction revealed ferromagnetic 111 planes that are antiferromagnetically coupled between neighboring planes and magnetic moments oriented along $\langle 11\bar{2} \rangle$ directions. Interestingly, this is the same magnetic order (G-type) observed

in NiO. The ordering was found to emerge below 120 K demonstrating the emergence of long-range G-type antiferromagnetic order with the cation moments oriented along the $\langle 11\bar{2} \rangle$. A sluggish change in the order parameter and the lack of a sharp peak in the heat capacity measurements through the magnetic transition temperature identified by both neutron diffraction [116] (Figure3.5 and muon spin resonance experiments [216] also indicates a glassy/disorder element to the magnetic transition.

Meisenheimer et al., reported on the magnetic ordering, anisotropy, and ordering temperature in (MgCoNiCuZn)O [11] and compositional variants using thin films. This was done using thin film "exchange bias" heterostructures which consist of a thin soft ferromagnetic layer, such as permalloy (Py), on top of a 70 nm thick (MgCoNiCuZn)O single crystal film. In exchange bias, the hard spins at the surface of the antiferromagnet will interact with the relatively soft spins in the ferromagnetic layer, allowing magnetic information to be read from the AFM using magnetometry. This technique is not only extremely sensitive to disorder, being driven by the uncompensated spins at the surface which are allowed to interact, but is one of the few methods for characterizing insulating thin film antiferromagnets. In these thin film exchange coupling measurements, the magnetic order and ordering temperature can be inferred by the modification of the soft ferromagnet's anisotropy at the onset of magnetic ordering in the oxide layer [12, 217, 218]. This coupling manifests as a broadening (coercivity enhancement) and horizontal shift (exchange bias) of the soft magnet's hysteresis loop as well as a divergence of the field cool and zero field cool moment versus temperature curves at the ordering temperature.

Temperature dependent magnetometry measurements of the heterostructure performed along differing crystallographic direction reveal long range antiferromagnetic order in the entropy-stabilized oxide below 165 K [11]. The antiferromagnetic nature of the oxide is made from the observation of anisotropic magnetic exchange bias between the [100] and [110] directions and the exchange coupling disappearing at the ordering temperature. It was also observed that the exchange bias observed at low temperature reached approximately 10x the exchange bias observed in a CoO/Py control sample. Exchange bias is mediated by pinned uncompensated spins in the

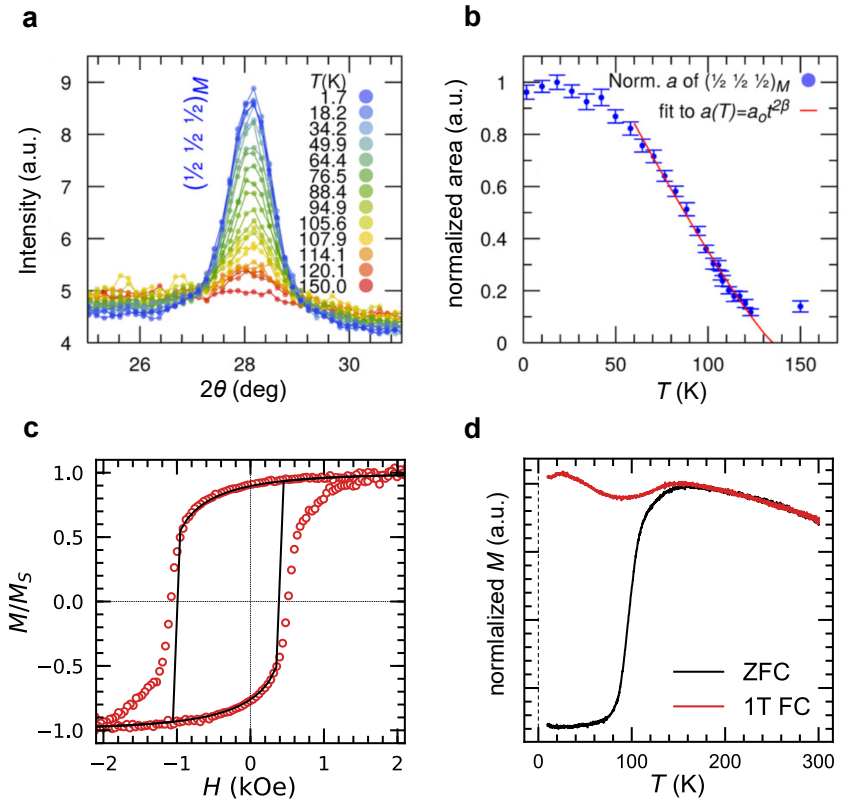

Figure 3.5: Antiferromagnetism of rock salt (MgCoNiCuZnO)O. a Neutron diffraction spectrum of a bulk sample showing the development of the (½ ½ ½) magnetic diffraction peak across the Néel temperature. **b** Normalized area of the peak in **a**, showing the same long glass-like transition to the antiferromagnetic state. **c** Exchange biased hysteresis loop from thin film permalloy/(MgCoNiCuZn)O at 10 K along [100] showing that it is antiferromagnetic with a large uncompensated moment. **d** Moment versus temperature curve of the same sample, showing the long, glassy transition to the antiferromagnetic state. **a,b** from ref [116] **c,d** from ref [12]. Figure adapted from ref [164].

antiferromagnetic layer at or near the interface. Thus the inclusions of non-magnetic cations and structural disorder may be responsible for this extreme behavior [12].

The magnetic properties have been characterized in other oxide crystal structures including spinels [219, 162, 220] and perovskites [221, 215]. In spinels, the Néel temperature and magnetic saturation tends to follow continuum trends, where as the magnetic lattice is diluted, the ferrimagnetic transition temperature and the saturation magnetization both decrease. Ferrite-based spinels of the type (MgCoNiCuZn)Fe_2O_4 tend to be magnetically soft, with coercive fields on the order of $\approx$ 100 Oe, whereas, more interestingly, chromite-based spinels are much harder, with coercive fields on the order of as much as 1 T, and display magnetic inconsistencies that belie their glassy nature. For example, (MgCoFeNiCu)Cr_2O_4 spinels show a large field dependent Néel

temperature and magnetization, which changes from 70-120 K under different training fields [220] (cooled in 1000 Oe and 100 Oe respectively). Musicó and colleagues attribute this observation to the existence of ferromagnetic regions before the critical temperature which, when saturated, increase the net magnetization and compete with overall ferrimagnetic order.

A similar result is reported for La(CrMnFeCoNi)O_3-type perovskites, where an intrinsic exchange bias-like effect is attributed to the formation of small local ferromagnetic regions contributing to the magnetization. The authors confirm this using Mossbauer spectroscopy, showing that the Fe moments in the HEO are in a mix of ferromagnetic and antiferromagnetic states (Figure 3.6) caused by competing superexchange and double exchange reactions between neighboring cations [215]. This is an exciting result because it is directly analogous to the formation of ferroelectric PNR discussed above, providing evidence that these magnetically analogous phenomena may be possible in an HEO and indicating the presence of competing ferroic orders. It was also found that, as the A site cation size changes and the structure deviates away from the ideal cubic perovskite, the frustration of the magnetic lattice (read through the Néel temperature) increases in a quasilinear manner. It is argued that this is due to increasing frustration of the octahedral cage, paralleling the complementary result found in the seminal ESO rock salt in reference [12]. When these same materials were deposited as single crystalline films with varying strain states [168], it was found that saturation magnetization scales with the in-plane strain, seemingly supporting this conclusion. These observations provide evidence of frustrated and disordered magnetism in HEOs, with direct analogues to existing relaxor materials. This indicates that engineering of the magnetic phase in HEOs should be achievable with both new and existing synthesis techniques. In the short term, the natural extension of these materials to frustrated magnetic systems such as spin glasses and liquids is promising.

Frustrated magnetism in spin glasses has been targeted due to its similarity to biological computing, with the study of spin glasses spurring advancement in the fields of neuromorphic computing and machine learning [209, 222, 223, 224]. This is because a magnetically frustrated system, caused by competing ferromagnetic and antiferromag-

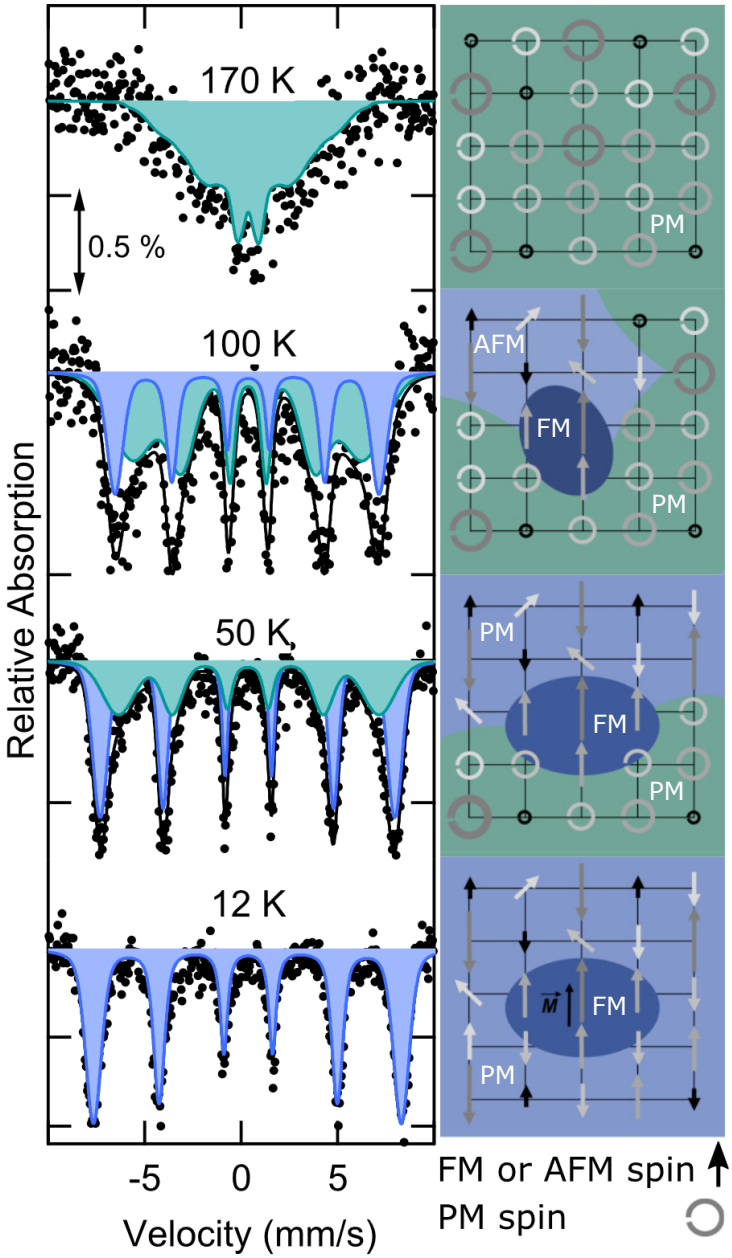

Figure 3.6: Magnetic nanoregions. Fe Mossbauer spectroscopy showing the magnetic structure of La(CrMnFeCoNi)O_3 below the Néel temperature, in which ferromagnetic nanoclusters are embedded in the AFM/PM matrix through the broad transition. From ref. [215]. Figure adapted from ref [164]

netic interactions within the material, has a large number of possible frozen metastable states, with coherence times that can be on the order of hours to days [210, 225]. As the materials is cooled below its transition temperature, the spins will freeze into a disordered configuration that is not only a function of the input (magnetic field, cooling rate, etc.) but will still respond slowly to an external stimulus. Due to a nonlinear phase response (i.e. a different frozen spin configuration due to differences in magnetic field,

cooling temperature, time, etc.), these systems have long been used to understand processes of neural network computing [226, 227] and dynamics in other metastable-phase analogs [210, 228, 229, 230].

From a materials perspective, these materials can be characterized by a frequency dependent response to AC magnetic field (much like relaxor ferroelectrics), long, field dependent transition periods, and slow, nonlinear time evolution [114, 231, 8, 232]. This glassy response to magnetic field has been observed in bulk antiferromagnetic ESOs [116] (in Li containing rocksalt oxides), where a small frequency dependence was seen in in the transition temperature between 100 Hz and 10 kHz. This should be a natural extrapolation of the current knowledge about magnetism in these materials, as local superexchange interactions will compete between ferromagnetic and antiferromagnetic depending on the neighboring species [11, 215]. Theoretical work [233] on (MgCoNiCuZn)O observes that the dilute magnetism in these materials behaves much like their antiferromagnetic rock salt counterparts CoO and NiO, which go through multiple magnetic phase transitions as the cation lattice is diluted with diamagnetic species [234, 235]. As both of these materials demonstrate frustrated AFM and true spin glass regions, it is reasonable to conclude that this same phenomena is reproducible in the HEO. Indeed this idea of using exchange bias from a spin glass to explore and tune the magnetic disorder in the system was explored recently [11], showing that the magnetic exchange in these materials can be controlled over a very large range, opening a pathway for further understanding of these phenomena.

HEOs is a nascent field and guidance can be drawn from the high-entropy alloy (HEA) community that has existed for close to 20 years. Much of the work in HEAs is concerned with mechanical behavior [236, 237, 101, 105, 109], however, there exists a body of work on magnetism [238, 239, 240], phase stability [241, 242], and defect formation/transport [243, 244] that is directly relatable to discussions on correlated materials. For instance, it has been observed in HEA CoCrMnFeNi that a FCC-HCP phase change can be driven using high magnetic field [242], showing a distinct spin-lattice coupling that may be valuable to the study of disordered magnetic materials. HEOs have been composed of constituents with different structures and magnetic interac-

tions, however the potential structural and magnetic diversity within existing transition metal HEAs is much greater than the HEOs studied currently. Expanding the number of competing magnetic and structural parent phases should increase frustration and potentially create nearly degenerate ground states for the formation of spin glasses, ices, and liquids or controllable phase transitions.

3.3 Concluding Remarks

HEOs are an emerging field of materials that show significant promise, not only for mechanical applications [186, 188], but for correlated electron behavior, a field where oxides display a wide range of fantastic properties [2, 212, 174, 175]. A significant draw of high-entropy effects is the enhanced solubilities of typically immiscible cations, which allows for stabilization of species in typically unfavorable environments due to competing stereochemistry [12, 182, 183], charge [186, 187], or magnetic ordering [116, 117, 233]. This effect can even be further extended by carefully controlling the kinetics with modern materials techniques such as nanoparticle synthesis or PVD, further extending the potential phase space of these many-component materials and offering an unparalleled tunability of charge, spin, orbital, and lattice degrees of freedom. Combined with the fact that oxides already offer an exciting playground for the study of new physical phenomena and technologically important properties, the advancement of the field is a direct opportunity for engineering and studying HEOs as an avenue for correlated electron systems. In addition to their unprecedented structural tunability [11, 245, 167, 168] HEOs display the ability to be grown on a variety of substrates [110, 221], including amorphous materials, resulting in a substrate versatility for potential applications. This combined with their relatively low deposition temperatures may make these materials extremely valuable for the electronics industry.

There are still a number of questions to be answered about HEOs, namely the role of disorder in functional phenomena [12, 186], the role of defects [198, 199], and the stability of new phases and compositions [246, 247]. Though the field is still developing, inspiration can come from existing work on functionality in the high-entropy alloy

community on magnetism [238, 239, 240], defect formation/transport [243, 244], and phase stability [241, 242]. HEOs have the exciting potential to become an extremely functionally relevant class of materials by incorporating new methods to enhance solubility and disorder with existing materials synthesis knowledge and techniques.

Chapter 4:

Disorder-Driven Enhancement of Interface Exchange

Entropy-stabilized materials are stabilized by the configurational entropy of the constituents, rather than the enthalpy of formation of the compound. A unique benefit to entropy-stabilized materials is the increased solubility of elements, which opens a broad compositional space with subsequent local chemical and structural disorder resulting from different atomic sizes and preferred coordinations of the constituents. Known entropy-stabilized oxides contain magnetically interesting constituents, however, the magnetic properties of the multi-component oxide are not obvious. Significant frustrations in the chemical, structural, and magnetic lattices of the oxide, arising from composition, preferred coordination, and magnetic dilution respectively, may lead to novel or enhanced functional phenomena. In this chapter, we examine the role of disorder and composition on the exchange anisotropy of permalloy/$(Mg_{0.25(1-x)}Co_xNi_{0.25(1-x)}Cu_{0.25(1-x)}Zn_{0.25(1-x)})O$ heterostructures. Anisotropic magnetic exchange and the presence of a critical blocking temperature indicates that the entropy-stabilized oxides considered here are antiferromagnetic in spite of the significant dilution from nonmagnetic elements. Changing the composition of the oxide tunes the disorder, exchange field and magnetic anisotropy. I show that this tunability can be exploited to enhance the strength of the exchange field by a factor of 10x at low temperatures, when compared to a canonical exchange bias system such as permalloy/CoO. Significant deviations from the rule of mixtures are observed

in the structural and magnetic parameters, indicating that the crystal is dominated by configurational entropy. These results reveal that the unique characteristics of entropy stabilized materials can be utilized and tailored to engineer magnetic functional phenomena in oxide thin films.

4.1 Experimental Motivation

In an entropy-stabilized material, the configurational entropic contribution (Δi_{conf}) to the Gibbs' free energy, given by $\Delta G = \Delta H - T\Delta S_{conf}$, drives the formation of a single phase solid solution [102, 104], exemplified in Figure 4.1. These materials have attracted significant interest due to the apparent deviations from Gibbs phase rule and desirable properties such as increased hardness, toughness, and corrosion resistance [102, 248, 100, 249, 109]. In particular, high entropy materials have been targeted for use in extreme temperature applications, as entropy domination prevents phase segregation and inhibits defect formation at high temperatures [105, 250, 185, 251]. While this concept was initially discovered in oxides, recent work [15] has extended the space of high-entropy materials to include disordered binary oxides, where solid solution behavior is observed across the cation sites. As the magnetic and electronic properties of oxides are strongly correlated to their chemistry and electronic structure [252, 253, 59], the increased solubility of species and disorder inherent to entropy stabilization could lead to exotic and colossal functional properties. Here, we propose to take advantage of the inherent chemical and structural disorder in entropy stabilized oxides to enhance the exchange bias in ferromagnetic/antiferromagnetic heterostructures.

Due to the chemical disorder, entropy-stabilized oxides provide a system for investigating the contribution of configurational entropy to magnetic structure and interface exchange. The exchange bias effect is thought to be driven by frustrated or uncompensated spins near the ferromagnet (FM)/antiferromagnet (AFM) interface [254, 255], thus the local chemical disorder inherent to high entropy materials may result in a large increase of the interface exchange coupling through frus-

trated superexchange and uncompensated spin creation via the incorporation of non-magnetic species [256, 114, 257, 258]. In the parent composition, rocksalt $(Mg_{0.2}Co_{0.2}Ni_{0.2}Cu_{0.2}Zn_{0.2})O$, three of the five binary oxide constituents are antiferromagnetic, with Néel temperatures of 289 K, 523 K, and 230 K for CoO (rocksalt), NiO (rocksalt), and CuO (tenorite) respectively. Additionally, two of the species, Cu and Zn, prefer tetrahedral coordination which may lead to a large degree of structural disorder in the material [165, 183, 182]. Considering these observations, here I present a study of FM/$(Mg_{0.25(1-x)}Co_xNi_{0.25(1-x)}Cu_{0.25(1-x)}Zn_{0.25(1-x)})O$ exchange bias thin film heterostructures that reveals the studied films are antiferromagnetic with properties which are strongly dependent on Co concentration, and by extension the degree of disorder. Due to compositionally-driven changes to the magnetic structure, the exchange field can be increased by a factor of 10x at low temperatures [254, 259, 260], when compared to a more conventional permalloy/CoO heterostructure.

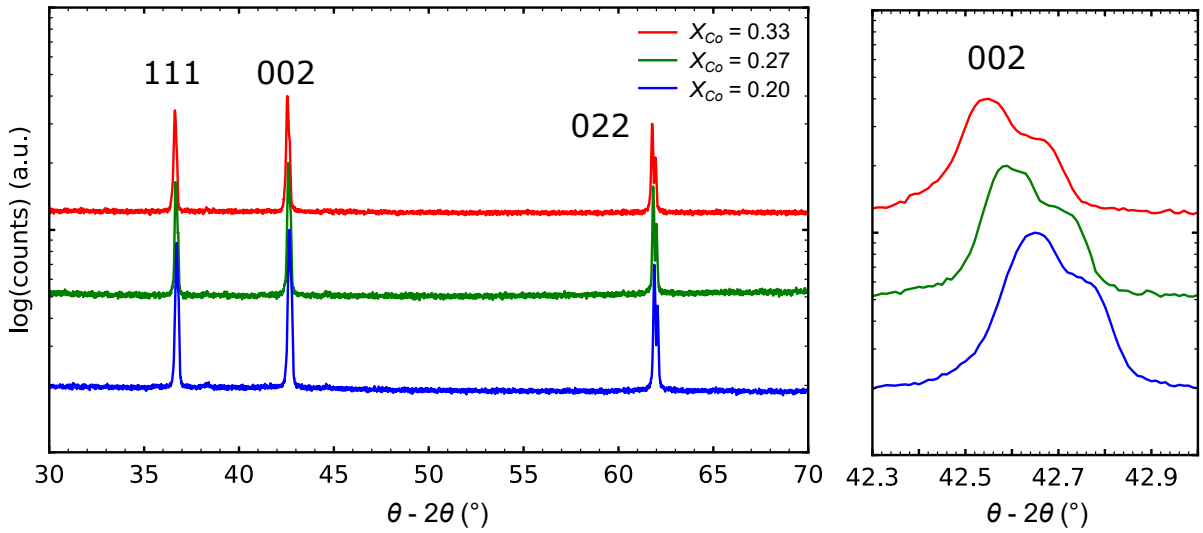

Figure 4.1: X-ray diffraction of Co-series films. $\theta - 2\theta$ X-ray diffraction of the targets of varying composition in the range of the 111, 002, and 022 diffraction peaks. These curves were obtained on a diffractometer that has Cu $K\alpha_1$ and Cu $K\alpha_2$ radiation. Lattice parameters were determined from the Cu $K\alpha_1$ peaks using Cohen's method. Comparing the measured lattice parameters from the targets to those of the films, we retrieve our out-of-plane strain values of -2.2%, -3.6%, and -4.5%.

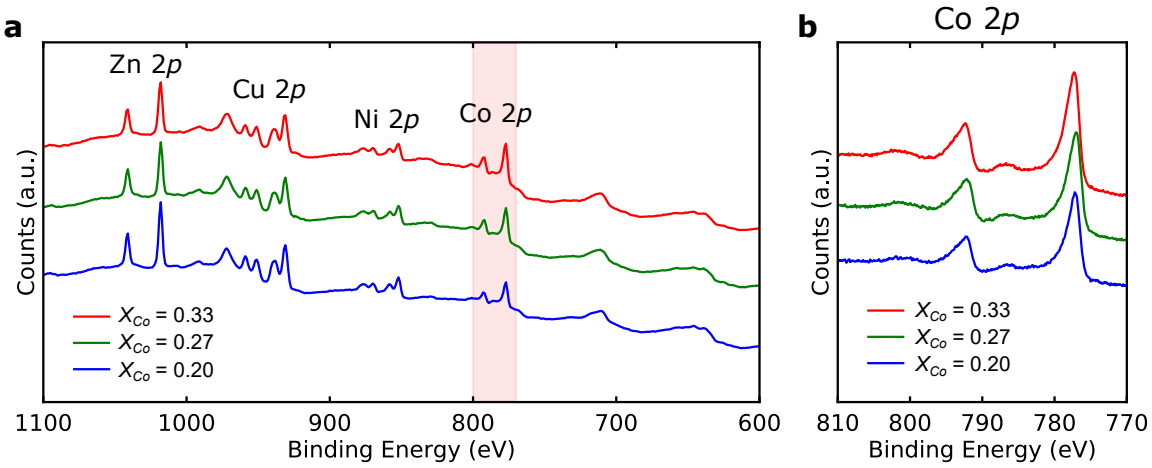

Figure 4.2: XPS of Co-series films. X-ray Photoelectron Spectroscopy (XPS) of bare entropy-stabilized oxide films showing **a** the full spectrum and **b** a high-resolution scan about the Co 2p peak. The included table shows the quantification of the mole fractions from the XPS spectra above. The differences in concentration from the expected amounts are within the error of the scan resolution. The Co concentrations are highlighted for visibility. The shapes and positions of the XPS peaks are invariant for all the compositions in this study, indicating that there are no changes in the oxidation state as the composition is varied.

Table 4.1: Concentration in Co-series films. Calculated from Fig. 4.2

Element	X_{Co} = 0.20	X_{Co} = 0.27	X_{Co} = 0.33
Co	0.199 ± 0.026	0.273 ± 0.013	0.329 ± 0.027
Ni	0.196 ± 0.025	0.180 ± 0.008	0.170 ± 0.014
Cu	0.204 ± 0.032	0.180 ± 0.022	0.164 ± 0.033
Zn	0.201 ± 0.029	0.180 ± 0.013	0.162 ± 0.018

4.2 Sample Deposition

Thin films of $(Mg_{0.25(1-x)}Co_xNi_{0.25(1-x)}Cu_{0.25(1-x)}Zn_{0.25(1-x)})O$ ($x = 0.2, 0.27, 0.33$), hereafter denoted $X = 0.20, X = 0.27$, and $X = 0.33$, were grown by pulsed laser deposition on single crystal MgO (001) substrates and the nominal composition was confirmed using X-ray photoelectron spectroscopy (XPS) (Figure 4.2). A varying composition of Co was chosen to evaluate the effect of entropy and magnetism in these samples because CoO is a well-studied AFM that has a Néel temperature of 289 K, conveniently near room temperature and accessible for our measurements. Above 0.33 mole fraction Co in the samples, the growth conditions begin to drift and the films are no longer of comparable quality and thus not studied here ($X = 1$ = CoO being the exception). A schematic of the structure is shown in Figure 4.4a. This

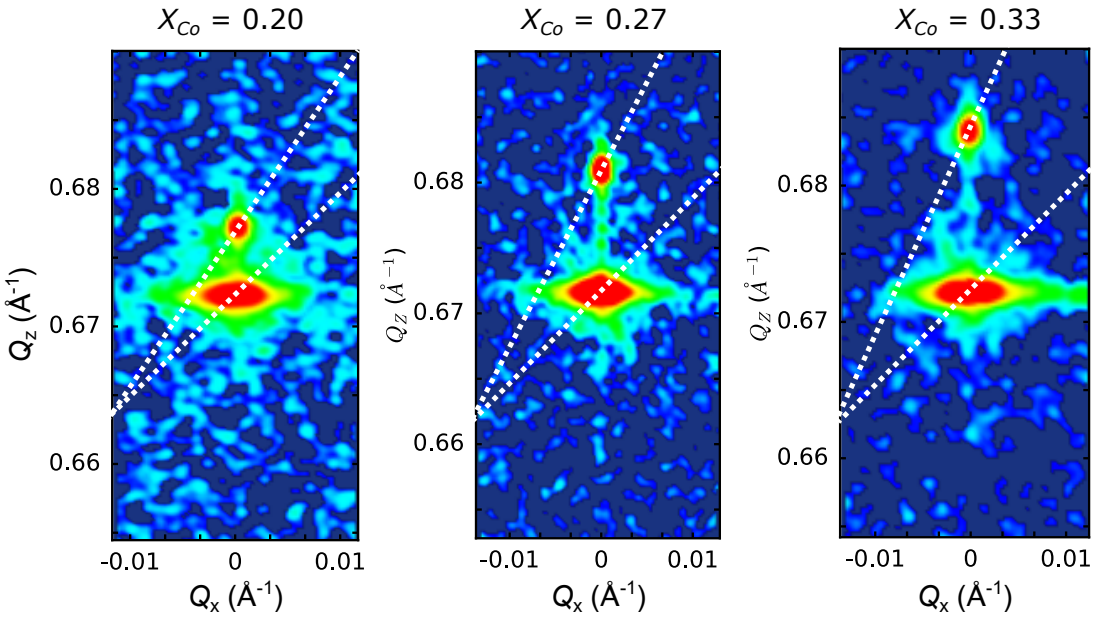

Figure 4.3: RSM of Co-series films. Reciprocal space maps of the film heterostructures about the 022 diffraction peak. The noncollinearity of the peaks with respect to the [202] reciprocal space vector (illustrated by the dashed lines) shows that the in-plane lattice constant of the film is pinned by the substrate. Using the $2\theta - \omega$ values taken at Q_X=0, the in-plane lattice constant of the film was determined using Cohen's method. In all three cases, there is an approximately 0.01% difference between the substrate and film, agreeing with the observation that the peaks lie at the same Q_X position.

geometry was chosen to minimize thickness effects in the AFM and to maximize exchange coupling [217].

X-ray Diffraction $2\theta - \omega$ scans, Figure 4.4b, show that our films are single phase, single crystalline, and epitaxial to the (001)-oriented MgO substrate. The Laue oscillations about the film peaks in Figure 4.4b show that the film surfaces are smooth. The period of the Laue oscillations about the 002 diffraction peak (Figure 4.4b) and X-ray reflectometry (not shown) agree with our expected thickness of 75-80 nm. As we increase the mole fraction of Co in our oxide films, an approximately linear decrease in the out-of-plane lattice constant is observed, shown in Figure 4.4c, while the in-plane lattice constant remains approximately constant due to epitaxial clamping from the substrate (Figure 4.3). Curiously, this is the opposite trend from what would be predicted using Vegard's law, using a weighted average of the ionic radii of the constituent species. For this calculation, all cations were assumed to be in a 2+

Table 4.2: Measured lattice constants of Co-variant samples. Calculated from Fig. 4.3

	c_0 (out-of-plane, Å)	a_0 (in-plane, Å)	Difference (in-plane, %)
X_{Co}=0.20			
substrate	4.205 ± 0.0021	4.205 ± 0.0021	
film	4.141 ± 0.0021	4.205 ± 0.0021	0.011
X_{Co}=0.27			
substrate	4.208 ± 0.0022	4.208 ± 0.0022	
film	4.091 ± 0.0022	4.207 ± 0.0022	0.0090
X_{Co}=0.33			
substrate	4.207 ± 0.0022	4.207 ± 0.0022	
film	4.056 ± 0.0022	4.208 ± 0.0022	0.0091

oxidation state based on XPS spectra (Figure 4.2) and either all octahedrally (red) or with Cu^{2+} and Zn^{2+} tetrahedrally (purple) coordinated [261]. Interestingly, the bulk lattice parameter (blue points) is in fair agreement with Vegard's law with all cations octahedrally coordinated. It has been observed in entropy-stabilized oxides that the lattice is locally distorted due to the presence of species that tend to Jahn-Teller distort, specifically Cu^{2+}, which prefers a tetrahedral coordination to break orbital degeneracy [183]. Tetrahedrally coordinated Cu^{2+} and Zn^{2+} are much smaller (0.71 Å and 0.74 Å respectively [261]) than octahedral Cu^{2+} and Zn^{2+} (0.87 Å and 0.88 Å respectively), potentially leading to a much smaller expected lattice constant. This does not, however, explain the negative trend with increasing Co incorporation seen in the lattice constant. This trend is also opposite to what would be expected from strain effects: as Co is the largest of the constituent cations, increasing the concentration of Co should create a larger compressive strain in-plane due to clamping and the film would be expected to expand out-of-plane in accordance Hooke's law [262]. The contraction observed in the films is very large, corresponding to a strain of -2.2%, -3.6%, and -4.5% with respect to the bulk for X = 0.20, X = 0.27, and X = 0.33 respectively (Figure 4.3). If the observed trend in the lattice constant cannot be explained by potential changes in chemistry or epitaxial strain, we assert that it may be due to the structural distortions caused by the preferred coordination of the Cu atoms locally expanding the lattice. If this were the case, as a similar effect has been observed in some Perovskite systems [263, 113], reduction in the concentration of Cu could be expected to shrink the lattice constant faster than the increase due to

higher concentration of larger (0.885 Å) Co^{2+} atoms. As the strain values observed from XRD are large, we expect physical distortion from the ideal rock salt structure is large and thus there is a significant corresponding influence on the distortion driven interface exchange coupling [264, 265].

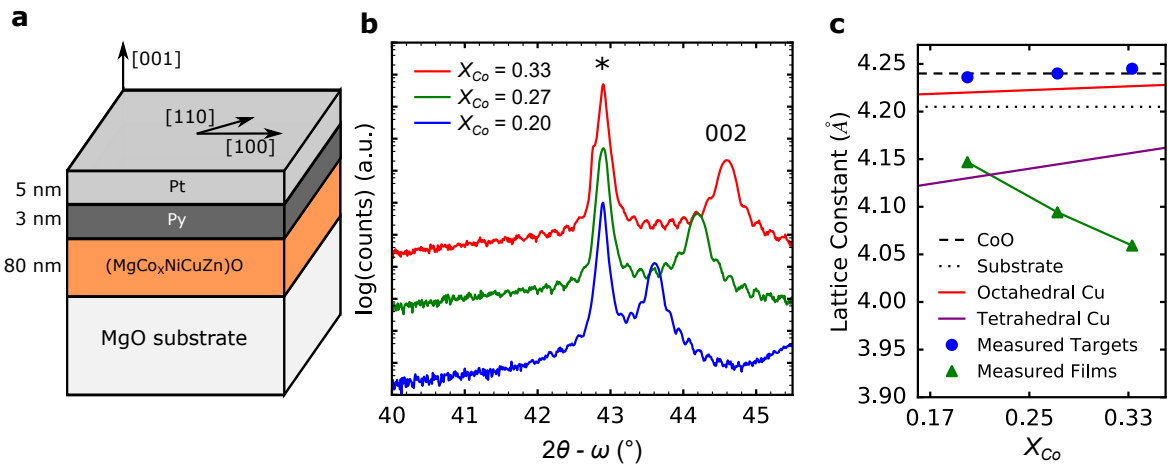

Figure 4.4: Structural characterization of exchange bias stacks. a Diagram showing the exchange bias heterostructure grown by pulsed laser deposition. $(Mg_{0.25(1-x)}Co_xNi_{0.25(1-x)}Cu_{0.25(1-x)}Zn_{0.25(1-x)})O$ is denoted as $(MgCo_xNiCuZn)O$ in the schematic. **b** $2\theta - \omega$ X-ray diffraction (XRD) data showing the substrate peak at 42.9°, marked with *, and film 002 peaks at 43.6°, 44.19°, and 44.59° for $x = 0.20$, 0.27, and 0.33, respectively. The films are single crystal and epitaxial with out-of-plane lattice constants that are dependent on Co concentration. The Laue oscillations about the film peaks show that the interfaces are flat and agree with our expected thicknesses of approximately 80 nm. The peak at 46° in the $x = 0.20$ sample belongs to Pt 002 and results from a slightly thicker capping layer on the structure (7 nm, as opposed to 4 nm). **c** Lattice constant derived from part **b** and from the bulk (target) materials (Figure 4.1) plotted as a function of increasing Co concentration. Lattice constants were determined using Cohen's method with calculated uncertainty smaller than the marker. The films display an opposite trend than would be expected from Vegard's law using the ionic radii values of either octahedrally (red) or tetrahedrally (purple) coordinated Cu^{2+} and Zn^{2+}, where the lattice constant should linearly approach that of CoO (dashed line). Interestingly, bulk values are in fair agreement with Vegard's law with all cations octahedrally coordinated. The deviation may be due to thermodynamic defects as a result of high temperature quenching.

4.3 Magnetic Analysis

A bias field and coercive field enhancement are the hallmarks of exchange bias behavior in FM/AFM bilayers. To explore the possibility of exchange bias in FM/entropy-stabilized oxide bilayers, field-dependent magnetometry measurements

were made on the Pt/Py/($Mg_{0.25(1-x)}Co_xNi_{0.25(1-x)}Cu_{0.25(1-x)}Zn_{0.25(1-x)}$)O samples presented in Figure 4.4. Upon cooling the samples from 350 K to 10 K in a 2 T magnetic field, a significant exchange bias (0.5-1 kOe) and coercive field (1.5-2.5 kOe) are observed along [100] and [110] crystallographic directions at 10 K (Figure 4.5). Consistent with exchange bias bilayers, the bias field changes sign with reversed cooling field polarity and the coercivity is enhanced with respect to that from a Pt/Py/MgO control sample at 10 K (0.14 kOe). Magnetic anisotropy is present in all cases with the [110] axis being the easier axis. This becomes more pronounced as the concentration of Co is increased. The ratio of the relaxation energies between the [110] and [100] crystallographic directions, A_{110}/A_{100} , changes from 0.26, to 0.23, to 0.12 for X = 0.20, 0.27, and 0.33 respectively, revealing that [110] becomes the more favorable axis as Co concentration increases. For the X = 0.27 and X = 0.33 samples, the loops along the [110] axis become sharp indicating a [110] easy axis. The observed anisotropy indicates the presence of long range magnetic order within the entropy-stabilized oxide and, with exchange bias, is suggestive of antiferromagnetism.

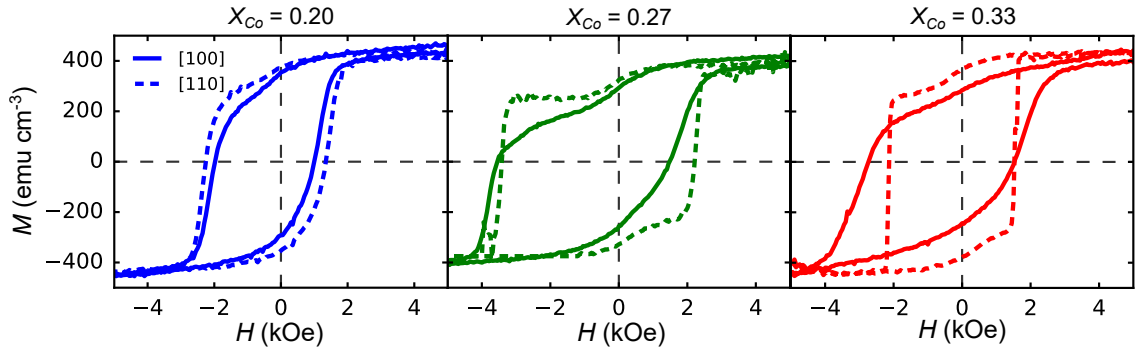

Figure 4.5: Magnetic hysteresis of Co-variant exchange bias samples. Plots of magnetic hysteresis at 10 K showing the exchange bias of the entropy-stabilized oxide exchange bias heterostructures containing varying compositions of Co. An increase in the concentration of Co changes the magnitude of the bias field and the anisotropy. The [110] easy axis anisotropy increases with molar fraction of Co.

In exchange bias FM/AFM systems, the coercivity enhancement and exchange bias must vanish at the blocking or Néel temperature. Figures 4.7a and b show temperature dependent exchange bias and coercive fields, along with those obtained from Pt/Py/CoO/MgO and Pt/Py/MgO reference samples, extracted from isothermal hysteresis loops taken every 25 K. Above approximately 200 K, the bias field and

enhanced coercive field (with respect to a Pt/Py/MgO control sample) vanish for the entropy-stabilized oxide bilayer samples. For a more accurate determination of the blocking temperature (T_B) as a function of Co concentration, field cooled (FC) and zero field cooled (ZFC) moment versus temperature curves (Figure 4.6) were measured. T_B was determined by the intersection of the FC and ZFC curves and reveals the onset temperature of the interaction between the two magnetic layers. A linear increase in T_B is observed (Figure 4.7b) with increasing Co incorporation. The vanishing of the exchange bias field and coercive field enhancement above the blocking temperature, combined with the observation that films with no Py layer show no measurable magnetic moment, indicates that these entropy-stabilized oxides are antiferromagnetic. The results of Figures 4.5 and 4.7 also show that as the concentration of Co is increased, the entropy-stabilized crystal can be engineered to take on properties of the constituents, such as increased anisotropy and blocking temperature [257, 258, 266], while still utilizing the increased disorder inherent to the system.

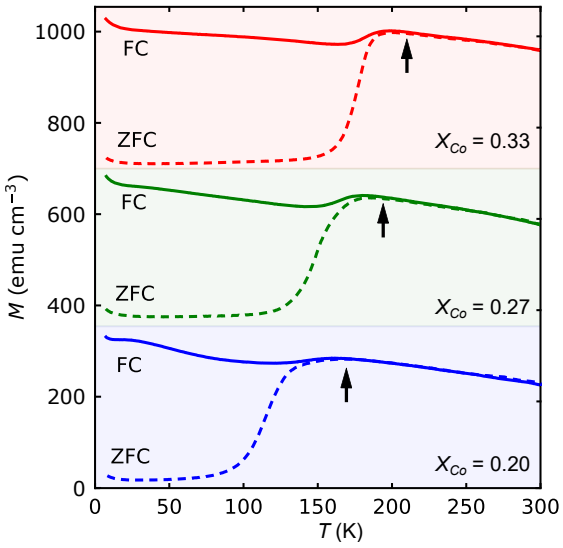

Figure 4.6: MVT curves of Co-variant exchange bias samples. Field cooled (FC) and zero field cooled (ZFC) moment versus temperature curves for the exchange bias samples. The curves are offset vertically for clarity. We can directly extract the blocking temperature (T_B) of the samples from the temperature where the FC and ZFC curves differentiate beyond the noise floor, noted by the black arrows. The curves are very wide, spanning approximately 50 K, indicative of a sluggish phase change.

In all our studied entropy-stabilized oxides, the exchange bias is significantly

greater than what is observed in the Pt/Py/CoO/MgO heterostructure (Figures 4.7a and 4.7b). Our measured values for the Pt/Py/CoO/MgO sample agree with published results [254, 266], in which it was concluded that the spins on the (001) interface of CoO are well compensated and thus result in a small exchange bias (approximately 0.1 kOe), even at low temperatures. Since it is known that there is significant local structural and chemical disorder in entropy-stabilized oxides [165], it would be expected that the magnetic lattice becomes frustrated on a local scale. This could result in a significant increase in the exchange strength, as it has been observed that exchange bias is strongly influenced by the density of disordered magnetic moments at the FM/AFM interface [254, 255, 267, 208, 232]. We also suspect that this is the cause of the anomalous shape in the hysteresis curves shown in Figure 4.5. According to the domain state model for exchange bias, a strong interfacial coupling between the FM and AFM can result in a large number of uncompensated moments at the interface which show hysteretic behavior in a shape similar to that of our experiments [268]. Additionally, in accordance with the domain state model, chemical dilution is predicted, and experimentally seen, to increase exchange bias due to the reduced energy cost for domain formation on impurity sites in the antiferromagnet [269, 256].

The blocking temperature of the system is expected to be dominated by the number (relative total fraction) of magnetic ions in the AFM and the strength of the superexchange interaction between them. This trend is expected and agrees, in terms of direction, with an estimation using the rule of mixtures from the Néel temperatures of the constituent oxides, which assumes that the Cu^{2+} sites will tend to distort and impart properties similar to those of the tenorite phase (i_N = 230 K) instead of a possible rocksalt phase, which may have a higher Néel temperature based on the trend shown by MnO (T_N = 122 K), FeO (T_N = 198 K), CoO (T_N = 289 K), and NiO (T_N = 523 K) rocksalts [270, 271]. The measured T_B, however, is lower than would be predicted and could be due to the local distortions inherent to the material which break local symmetry and could frustrate superexchange interactions. A potentially higher T_N from Cu^{2+} in an octahedral coordination would only increase the observed disparity. Additionally, a peak in both the coercive field and the bias field for X = 0.27

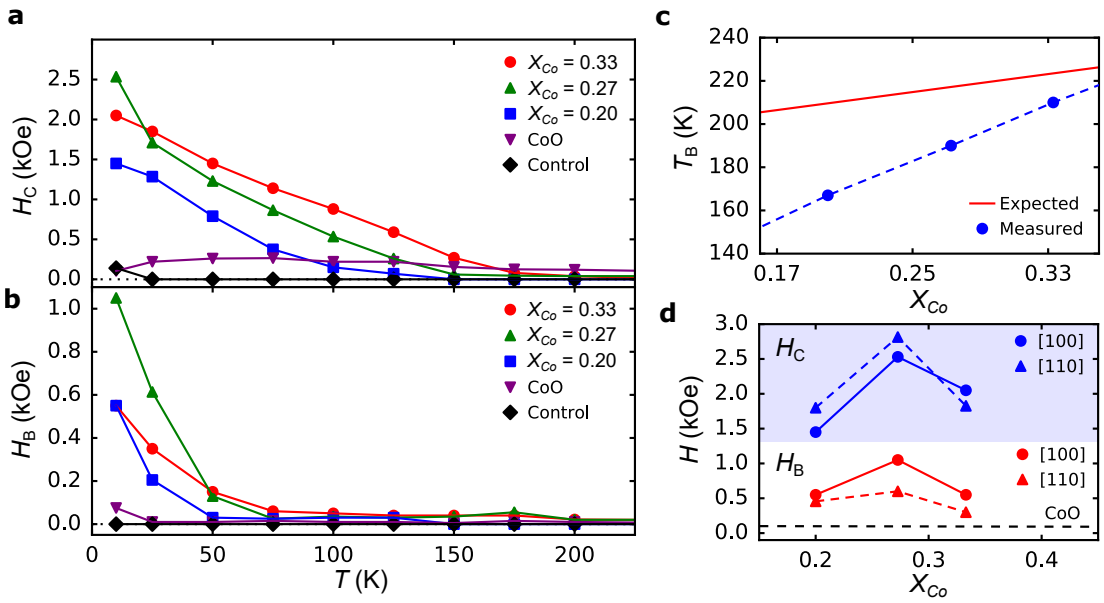

Figure 4.7: Magnetic parameters of Co-variant samples. Plot of **a** coercive field and **b** exchange bias field, measured along the [100] crystallographic axis, versus temperature for entropy-stabilized oxide exchange bias heterostructures containing varying compositions of Co, plotted with a Pt/Py/CoO/MgO heterostructure (labeled CoO in the figure) and Pt/Py/MgO control sample. **c** The blocking temperatures (T_B) extracted from Figure 4.6 (Measured), along with our prediction using the rule of mixtures (Expected), obtained by taking a weighted average of the individual Néel temperatures of the constituent binary oxides. The blocking temperature deviates significantly from the rule of mixtures, but approaches the expected value as the concentration is increased. The dashed line is provided as a guide to the eye. **d** Plot showing the change in coercive (H_C) and bias (H_B) fields as a function of Co concentration along both the [100] and [110] crystallographic directions at 10 K. The dashed line at 75 Oe corresponds to the bias field in the Pt/Py/CoO/MgO control sample. Error bars are smaller than the points for all plots.

is observed in Figure 4.7d. This could be due to a balance between the disorder inherent to the entropy stabilized system, which would increase the exchange bias, and a larger percent of magnetic ions, which would also be expected to increase the exchange bias [269, 272, 256]. As the mole fraction of Co is increased, the percentage of magnetic ions is greater, but the entropy of the structure decreases and thus an optimal Co concentration for maximizing the exchange coupling is expected.

In summary, we show that by utilizing the inherent chemical and structural disorder of entropy stabilized oxides, we can engineer a 10-fold increase in the exchange coupling with a ferromagnetic Py layer. Additionally, this phenomenon is strongly dependent on the concentration of Co in the sample, showing a relationship between chemical disorder and the density of uncompensated spins at the FM/AFM interface.

Our results indicate that there are competing factors, degree of local disorder and concentration of magnetic ions, resulting in conditions that give rise to a maximum exchange coupling. As the concentration of Co in the samples is increased, we see an increase in the magnetic anisotropy along the [110] direction showing that, even with this large degree of disorder, entropy stabilized oxides can be intelligently engineered to take advantage of properties possessed by the constituent oxides while utilizing the inherent advantages of entropy stabilization.

Chapter 5:

Stereochemical Control of Magnetic Frustration

Entropy-stabilized oxides possess a large configurational entropy that allows for the unique ability to include typically immiscible concentrations of species in new configurations. Particularly in oxides, where the physical behavior is strongly correlated to stereochemistry and electronic structure, entropic stabilization creates a unique platform to tailor the interplay of extreme structural and chemical disorder to realize unprecedented functionalities. Here, we control stereochemically-driven structural disorder in single crystalline, rocksalt, (MgCoNiCuZn)O-type entropy-stabilized oxides through the incorporation of Cu^{2+} cations. We harness the disorder to tune the degree of glassiness in the magnetic structure. Structural distortions driven by the Jahn-Teller effect lead to a difference in valence on the Co cation sites, which extends to dilution and disorder of the magnetic lattice. A spin glass model reveals that the fractional spin ordering of the magnetic lattice can be tuned by 65%. These findings demonstrate entropy-stabilization as a new tool for control of functional phenomena.

5.1 Experimental Motivation

Highly disordered, chemically homogeneous, single phase metallic and ceramic solid solutions have attracted significant interest in recent years due to the observation of enhanced physical properties and new emergent phases [102, 236, 109, 248, 101]. In

high-entropy and entropy-stabilized materials, crystals with typically 5 or more species, the large configurational entropy is thought to be a critical factor in the stabilization of the phase [100, 273, 237, 106]. ESOs enable an unprecedented new degree of chemical control in materials, as the technique can be used to incorporate typically immiscible concentrations of cationic species in an atypical coordination. As the properties of oxides are strongly correlated to their stereochemistry and electronic structure [274, 208, 37, 211], ESOs thus present the opportunity to tune charge [186], lattice [165, 182, 13], and spin [11, 116] disorders to new extremes in a single-phase, single-crystalline material.

In a conventional binary rock salt oxide, such as MgO, NiO, or CoO, the cation species sit on octahedrally-coordinated sites. The (MgCoNiCuZn)O-type rock salt ESOs studied here, however, are expected to deviate from this ideal configuration due to the presence of disordering species. Specifically, Cu^{2+} cations will tend to undergo a tetragonal distortion from an octahedral configuration in order to break the e_g orbital degeneracy present in a d^9 system (i.e. the Jahn-Teller (JT) effect). In (MgCoNiCuZn)O, however, the Cu^{2+} cations are forced into the rock salt structure, in competition with the JT effect, leading to a frustration of the atomic positions around the site. This competition is expected to significantly impact the functional properties and disorder [11]. Here we find that the crystalline lattice of (MgCoNiCuZn)O ESO thin films is structurally distorted by this stereochemical frustration and drives a change in the fraction of 3+/2+ Co cation oxidation states. We find that this structurally driven change in oxidation state corresponds to the disorder in magnetic structure. Our results reveal that the unique characteristics of ESO single crystal thin films can be tuned to large degrees to control of structural and chemical disorder and engineer magnetic functional phenomena.

To this end, copper variant $(Mg_{0.25(1-x)}Co_{0.25(1-x)}Ni_{0.25(1-x)}Cu_xZn_{0.25(1-x)})O$ (x = 0.11, 0.17, 0.20, 0.24, 0.27) and cobalt variant $(Mg_{0.25(1-x)}Co_xNi_{0.25(1-x)}Cu_{0.25(1-x)}Zn_{0.25(1-x)})O$ (x = 0.20, 0.27, 0.33) ESO thin films were investigated to probe the interplay of chemical and structural disorder on magnetic order. These compositions were chosen systematically because Cu^{2+} cations will tend to distort the octahedral

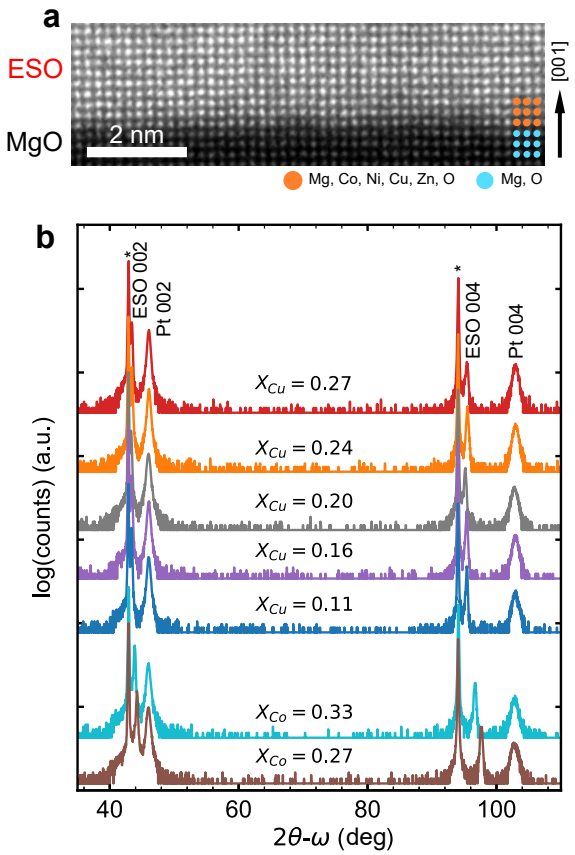

Figure 5.1: Structural characterization of Cu-variant samples. a Atomic resolution cross-section HAADF-STEM micrograph of 90 nm thick ESO film on MgO substrate. **b** $2\theta - \omega$ XRD spectra of Cu and Co variant ESO thin films. Only the 002 and 004 peaks from the ESO film are present, showing phase purity and epitaxy. * indicates MgO 002 and 004 substrate peaks.

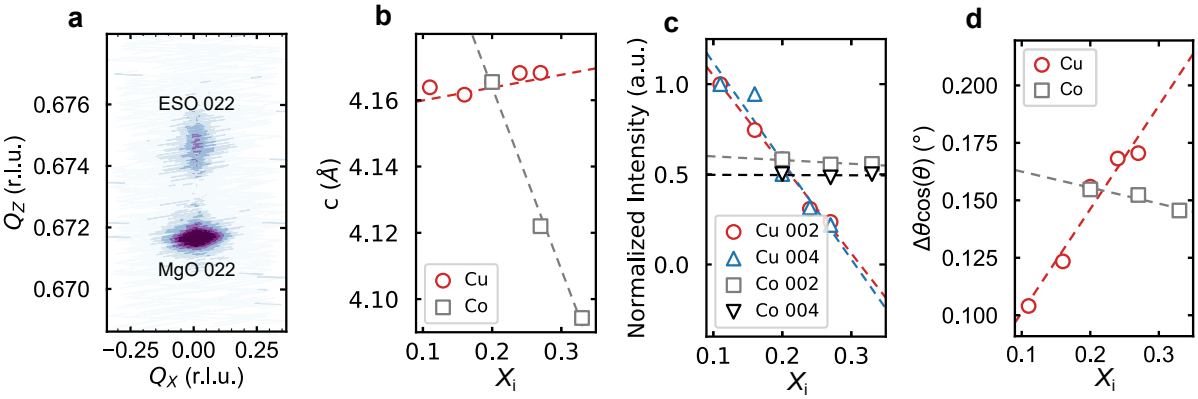

Figure 5.2: Diffraction analysis of Cu-variant samples. a Reciprocal space map of equimolar, x = 0.20 ESO, showing that the film is clamped to the substrate in the Q_x direction (in-plane). **b** Out-of-plane lattice constants of the Cu variant and Co variant ESO films determined using Cohen's method. **c** Normalized peak intensities of the ESO 002 and 004 peaks, showing a decrease in the peak intensity with increasing Cu. **d** Full-width at half-max ($\Delta\theta$) of the 002 peaks in Fig. 5.1b, deconvolved with peak position, showing a significant increase in the peak width with increasing Cu concentration and a small decrease with Co composition.

site, creating a mechanism of structural disorder. This effect has been observed both in bulk [183], from diffraction analysis, and previously in thin film form [165] using extended X-ray absorption fine structure. Because these active sites are spread across the crystal in large concentrations (1/5 of cation sites in an equimolar, 5-component ESO), we hypothesize that this will create a concerted effect and drive structural frustrations across the whole system [183, 275]. In contrast, Co^{2+} prefers octahedral coordination, minimizing structural disorder, and changes the average magnetic moment significantly (1.6 to 1.9 μ_B cation^{-1}) [11]. Bulk $(Mg_{0.2}Co_{0.2}Ni_{0.2}Cu_{0.2}Zn_{0.2})O$ was previously shown, through neutron and AC susceptibility, to be antiferromagnetic (AFM) with a degree of glassiness manifested in the sluggish paramagnetic (PM)/AFM transition and temperature dependence of the peak in susceptibility [116]. This material was also shown in the previous chapter to be AFM as a thin film, possessing a large ferromagnetic (FM)/AFM exchange coupling [11] when capped with permalloy (Py) in a heterostructure. As exchange bias is especially sensitive to magnetic frustration [276, 268] and provides an ideal method for studying magnetic disorder in these systems, since the magnetic disorder of the oxide can be read out through effects on the exchange interaction. Through this novel technique, we show that the Cu^{2+} concentration can be directly correlated to lattice, charge, and spin disorder in ESO thin films, while the structure retains a high degree of crystallinity and phase purity.

Previous work has shown that the dominant exchange in ESO thin films is antiferromagnetic [11, 116, 117], thus we deposited FM/ESO bilayers in order to probe the exchange effects and evolution of magnetic order with chemical and structural disorder in the ESO films. 80 nm thick single crystalline epitaxial films of$(Mg_{0.25(1-x)}Co_{0.25(1-x)}Ni_{0.25(1-x)}Cu_xZn_{0.25(1-x)})O$ (x_{Cu} = 0.11, 0.17, 0.20, 0.24, 0.27) (hereafter referred to as Cu variant) and $(Mg_{0.25(1-x)}Co_xNi_{0.25(1-x)}Cu_{0.25(1-x)}Zn_{0.25(1-x)})O$ (x_{Co} = 0.20, 0.27, 0.33) (Co variant) were deposited on (001)-oriented MgO single crystal substrates. All ESO films show excellent crystalline quality and phase purity by high-angle annular dark-field scanning transmission electron microscopy (HAADF-STEM) and X-ray diffraction (Figs. 5.1 and 5.3). The targeted composition was confirmed by X-ray photoelectron spectroscopy (Fig. 5.4) to within the measurement resolution and the

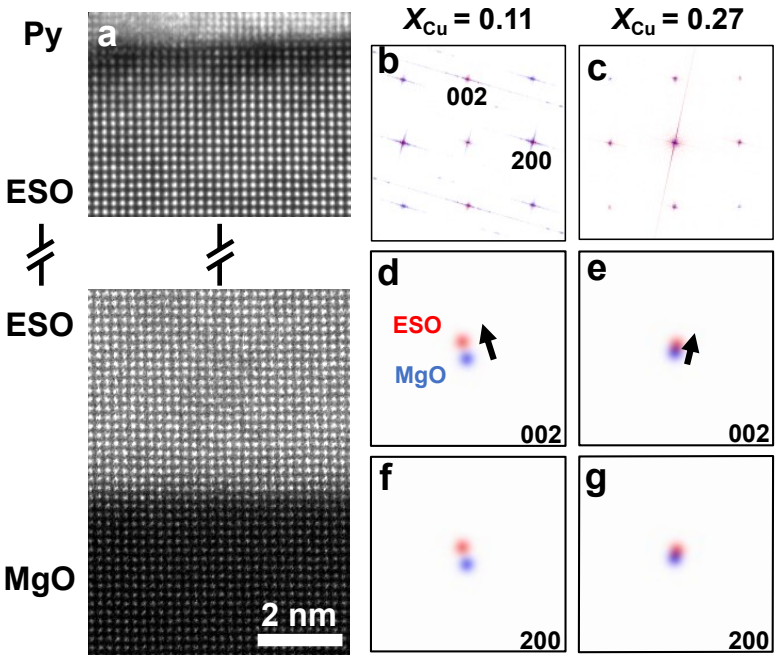

Figure 5.3: STEM analysis of Cu-variant samples. a Atomic resolution cross-section HAADF-STEM micrograph of 90-nm-thick ESO film on MgO substrate. **b, c** Color composite FFT of HAADF-STEM image shows epitaxial relationship between layers. **d-g** Non-linear regression analysis of 002 and 200 peaks showing the tetragonal distortion along the 002 (out-of-plane) direction in both x_{Cu} = 0.11 and 0.27. **h** EELS spectrum averaged over ESO film region confirming the presence of Mg, Co, Ni, Cu, Zn, and O peaks.

Table 5.1: Composition of Cu-variant samples. Calculated from Fig. 5.4

Element	x_{Cu} = 0.11 (%)	x_{Cu} = 0.16 (%)	x_{Cu} = 0.20 (%)	x_{Cu} = 0.24 (%)	x_{Cu} = 0.27 (%)
Co	27.9 ± 3.2	26.9 ± 0.9	24.9 ± 0.7	24.1 ± 0.6	21.2 ± 1.0
Ni	28.8 ± 2.1	27.2 ± 0.4	24.4 ± 0.9	23.7 ± 1.3	21.6 ± 1.3
Cu	15.2 ± 1.3	19.1 ± 1.5	25.6 ± 1.7	25.6 ± 3.4	34.8 ± 0.8
Zn	28.1 ± 0.6	26.8 ± 1.0	25.2 ± 0.6	22.6 ± 0.6	22.4 ± 0.8

film surface roughness was determined to be approximately 100 pm RMS or less by atomic force microscopy. The ESO films were capped with 3 nm of Py as a FM layer, and approximately 20 nm of Pt to prevent oxidation of the Py [11]. We measure a saturation magnetization of approximately 800 emu cm^{-3} for our permalloy films, agreeing with the bulk value.

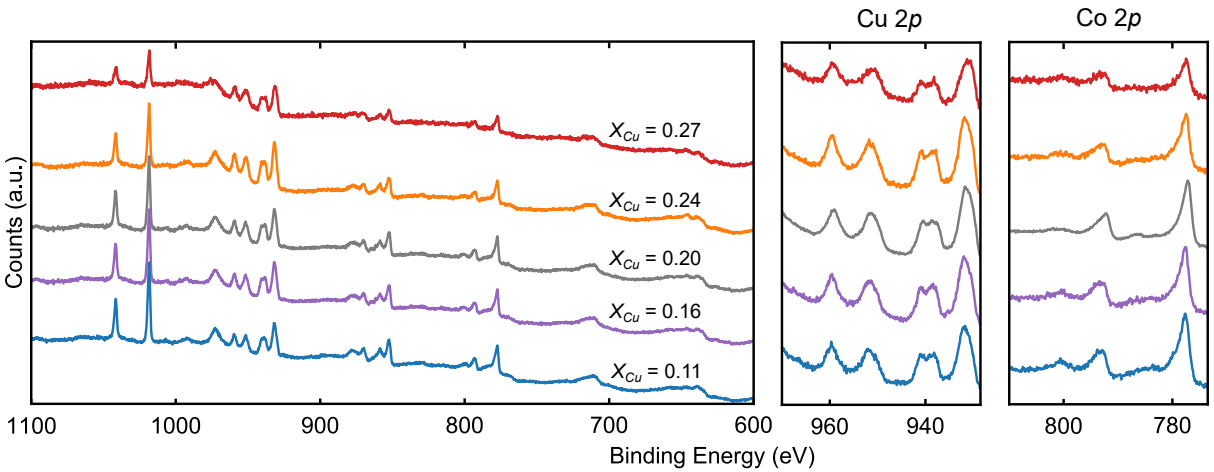

Figure 5.4: XPS composition of Cu-variant films. XPS shows that compositions are nominal to within 1% based on fits to the data. This does not, however, take into account the calibration error of the instrument which is approximately 3%. XPS spectra were obtained using a Kratos Axis Ultra XPS with monochromated Al source and using a charge neutralizer. Spectra were taken from 1200 to 10 eV and high-resolution scans were taken about the Co, Ni, Cu, and Zn 2*p* peaks. These high-resolution scans were used for quantification.

5.2 Tuning of Structural Disorder

In the typical Jahn-Teller distortion of Cu^{2+}, the axial bond will elongate and the basal bonds will contract in order to break the octahedral symmetry and remove the degeneracy of the unpaired electron in the eg orbital [275]. This, naturally, gives rise to a bimodal distribution of bond lengths and a tetragonal distortion of the cation site. From our XRD spectra, we observe this structural distortion as a function of Cu composition. The peak intensities of the 002 and 004 film diffraction peaks, normalized to the substrate peak intensity and then scaled, show a linear decrease with increasing concentration of Cu (Fig. 5.2d), consistent with an increasing tetragonal or monoclinic distortion of the lattice that breaks symmetry about the 002 peak [183]. Additionally, the peak width increases with the concentration of Cu (Fig. 5.2d), implying a large degree of correlated disorder in the system [277]. In contrast, the relative intensity and peak widths of the 002 peaks for the Co variant films remain invariant (Fig. 5.2c,d). Here, the broadening of peaks is consistent with atom displacements that are larger near an impurity atom in a randomly dilute solid solution (Huang scattering [278]). Uncorrelated displacements (known as Debye-Waller scattering [279, 280]) and uncorrelated chemical disorder (known as Laue monotonic scattering [281]) do not broaden Bragg peaks in the same fashion, therefore we are able to directly tie and

tune the degree of global structural disorder in the material to the concentration of the Jahn-Teller species.

Atomic-resolution HAADF STEM of the ESO film (Fig. 5.1a and Fig. 5.3) confirms single crystal growth and one-to-one atomic epitaxy at an atomically sharp interface with the substrate. We observe that crystal symmetry is broken through a contraction, relative to the substrate, of the lattice along the growth direction (tetragonal distortion) as seen by an expansion of the 00n lattice peaks in Fourier space. This change in lattice constant is correlated to Cu concentration, as the out-of-plane lattice constant increases measurably when comparing the 27% Cu sample to the 11% Cu sample. The Fourier transform was measured over a 20 nm^2 field of view, and in this sense, is a local representation of the film structure. STEM was done in collaboration of Sung S.H., J. Gim, and R. Hovden, referenced in [12].

From density functional theory (DFT) calculations of our Cu variant ESOs, we can observe this structural distortion on an atomic scale. DFT calculations were performed based on the projector augmented wave (PAW) method [282, 283] using the Vienna Ab initio Simulation Package (VASP) [284, 285, 286, 287]. Utilized pseudopotentials included 9, 2, 12, 10, 11, and 6 valence electrons for Co, Mg, Zn, Ni, Cu, and O respectively. A 900 eV plane-wave cutoff and Monkhorst-Pack k-point grids with a density of at least 20 k-points $Å^{-1}$ were used to obtain energy convergence of under 1 meV/atom. Ion relaxations with fixed lattice constants were performed using the functional of Perdew-Burke-Ernzerhof [288]. Forces on atoms were relaxed to within 1 meV $Å^{-1}$. Random alloys were modeled using Special Quasi-random Structures (SQSs) generated with the Alloy Theoretic Automated Toolkit [289] taking into account pair correlations up to 6 Å. Supercells contained 24, 60, and 36 atoms for the 33% Cu and 33% Co, equimolar, and 11% Cu and 11% Co compositions, respectively. Structural data was assembled from SQSs that were relaxed using multiple magnetic configurations, including antiferromagnetic along (111) planes, ferromagnetic, and multiple random magnetic configurations. As sampling of roughly random alloy configurations produces structural probability distributions with clear trends based on composition, and the individual supercell distributions were qualitatively similar, we

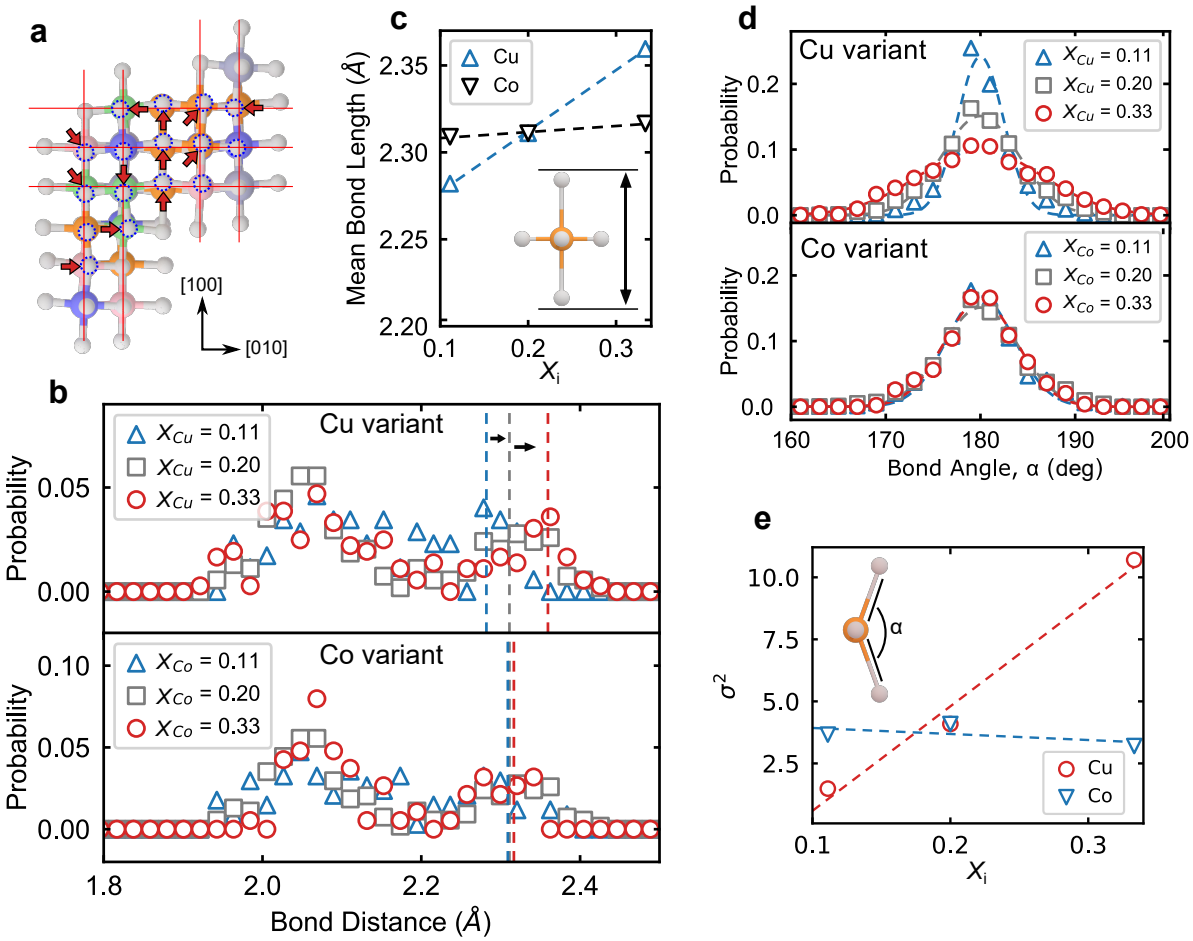

Figure 5.5: Simulated bond lengths of Cu- and Co-variant samples. a 94-atom supercell of Cu-rich ESO relaxed using DFT. Ideal planes of atoms are overlaid in red, highlighting the structural distortions (emphasized by arrows) most clearly on the oxygen anion sites (shown in grey). The Cu cations are shown in orange. **b** Histograms of bond lengths on the Cu-cation sites for $x_{Cu,Co}$ = 0.11, 0.20, 0.33 ESOs, demonstrating the characteristic double peak of a Jahn-Teller distorted cation. **c** Axial bond length of the Cu site in Cu variant (Cu) and Co variant (Co) ESO. As the concentration of Cu is increased in the material, we observe an increase in the length of the z (extended)-axis on the Cu cation site, implying that the degree of distortion is sensitive to the local environment about the Cu site and the total concentration of Cu. **d** Histogram of cation-anion-cation bond angles, α, for Cu variant and Co variant ESOs calculated from DFT. **e** Variance (σ^2) of the Gaussian fits to the data in **d**. As the concentration of Cu cations is increased, the variance of the calculated bond angle changes significantly in a linear fashion while the Co variant samples remain approximately constant.

believe that the observed trends are real and expect them to be present in the physical system. DFT simulation was done in collaboration with L. Williams and E. Kioupakis, referenced in [12].

The relaxed atomic coordinates (Fig. 5.5a) show a large spatial deviation from the perfect rock salt structure. The histogram of the bond lengths in our simulated

ESO supercells exhibits the characteristic bimodal distribution of the Jahn-Teller effect (Fig. 5.5b). Interestingly, we also observe a shift in the peak length of the extended axial bond with increasing concentration of Cu (Fig. 5.5b, c). In the case of varying Co concentration, the peak-length shift is negligible. This shows that Cu is responsible for the structural distortion. Additionally, our analysis demonstrates that the disorder-driving sites are working in a concerted manner, agreeing with our observation in Fig. 5.2 of a concerted symmetry breaking.

Further, our first-principles calculations of the structures for the Cu and Co variant ESOs also show a significant variation in bond angle (up to nearly 20°) that is correlated to increasing Cu incorporation (Fig. 5.5d, e). As the concentration of Cu in the supercell is increased, the variance of the bond angle distribution increases sharply, by 10x over the relatively small compositional space. This linear trend also agrees with the compositional disorder observed in our XRD measurement from the FWHM of the film diffraction peaks [277] (Fig. 5.2d). The bond length and bond angle disorder can influence cation charge state (through strain) and magnetic interaction, as superexchange is particularly susceptible to changes in orbital overlap [290, 291, 292, 293] and coordination. Thus, we probe the evolution of the cation charge and AFM character by X-ray absorption and X-ray linear dichroism.

5.3 X-ray Absorption

It has been previously observed that charge disorder can be fundamentally tied into structural effects in ESOs [186, 183, 17]. From X-ray absorption spectroscopy (XAS) measurements, we observe a significant fraction of low spin Co^{3+} in the oxide for all compositions (Fig. 5.6a). As the concentration of Cu is increased, we observe an approximately linear change in the ratio of high spin Co^{2+} to low spin Co^{3+} (Fig. 5.6b). At higher concentrations of Cu, there is a smaller fraction of Co^{2+}. As the only process variable changing in our experiment is the concentration of Cu sites, and thus the structural homogeneity that is proportional to Cu inclusion, we posit that that the observed change in charge state is influenced by the Cu^{2+} JT effect. We find that the

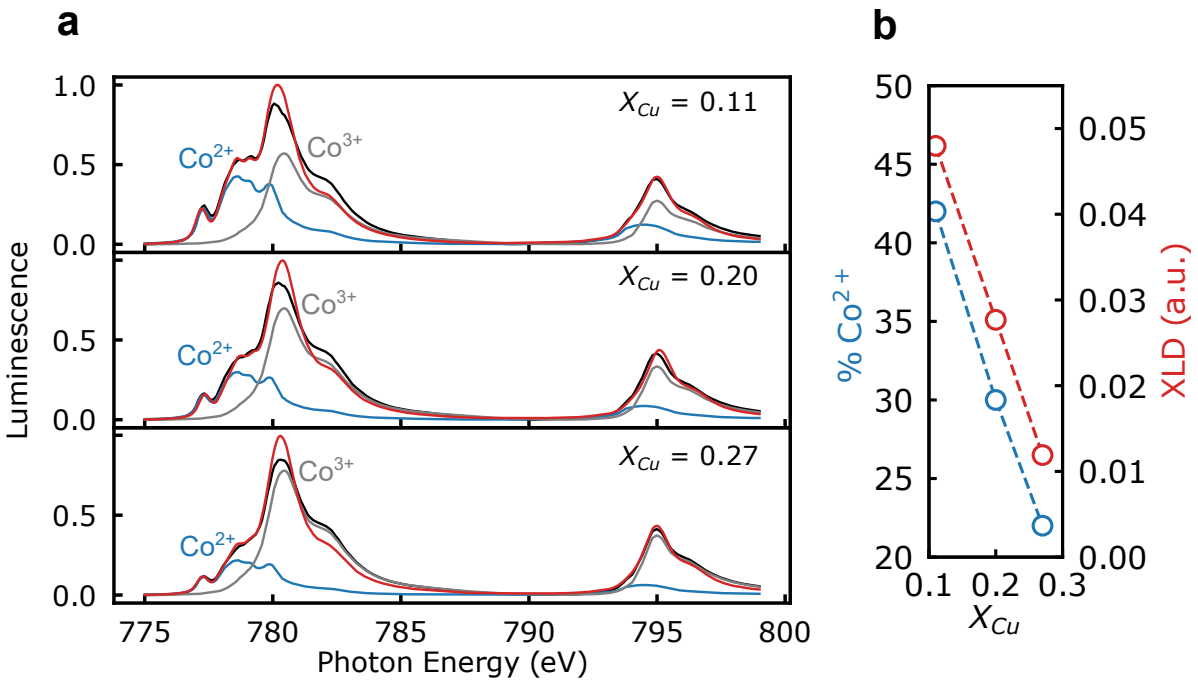

Figure 5.6: XMLD analysis of Cu-variant samples. a Evolution of Co XAS lineshapes from X-ray luminescence in the Cu-series samples showing a gradual change in ratio of high spin Co^{2+} (blue) to low spin Co^{3+} (grey) proportional to the Cu content of the sample. Measured spectra are shown in red, with fits in black. Spectra were fit to a linear combination of the Co^{2+} (high spin), Co^{3+} (low spin), and Co^{3+} (high spin) peaks taken from ref. [41]. The Co^{3+} fraction was eliminated as a result of the fitting and is therefore not shown. **b** Plot of Co^{2+} fraction from the coefficients of the linear combination in **a** alongside measured X-ray linear dichroism (XLD) from samples in **a**. As the Cu concentration of the samples is increased, the fraction of the 2+ oxidation state decreases proportionally. Additionally, the dichroic signal on the Co cation sites decreases with the same trend. XLD was measured at room temperature and 80 K, above and below the Néel temperature respectively to observe structural and magnetic components.

charge state of the other cations remains invariant to within experimental resolution (Fig. 5.7).

XAS and X-ray linear dichroism (XLD) spectra were measured at the Advanced Light Source at Lawrence Berkeley National Laboratory on beamline 4.0.2. XA and XLD data were recorded at both room temperature and 80 K, above and below the Néel temperatures of the samples. Full spectra at 80 K are shown in Fig. 5.7. Spectra were normalized over 8 scans per element, and data reported here shows the X-ray absorption that was calculated using luminescence yield collected from samples. This detection mode uses a photodiode to collect visible luminescence from the substrate (i.e., scintillator) to measure the intensity of X-rays transmitted through the film. X-ray

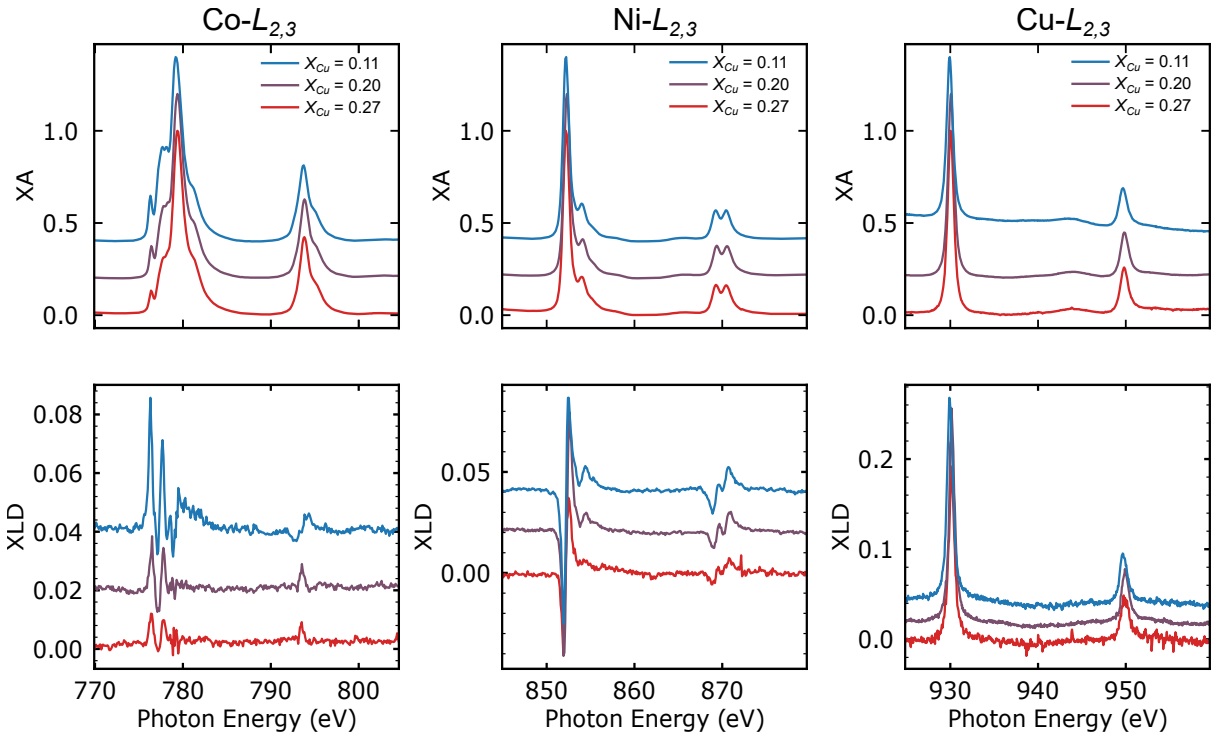

Figure 5.7: XAS analysis of cations in Cu-variant samples. X-ray absorption spectroscopy and X-ray linear dichroism (XLD) of ESO samples at 80 K. From the data, we see that there is a significant evolution of both the peak shape and the dichroic signal of the Co L-edge data. This corresponds to a decrease in the ratio of Co^{2+} to Co^{3+} in the sample and a decreased magnetic signal, both with the increase of Cu composition. Curves have been offset vertically for clarity.

absorption data were fit to a linear combination of reference spectra for Co^{2+}, Co^{3+} (low spin), and Co^{3+} (high spin) from ref. [294] using a basin-hopping optimization technique as implemented in Scipy for Python3. The Co^{3+} fraction was eliminated as a result of the fitting and is therefore not shown. Coefficients from this fit are reported as cation fractions.

All spectra were measured with linearly polarized X-rays; both horizontal and vertical polarizations were used. At every photon energy, absorption intensity is scaled to the flux of incoming X-rays. Spectra are normalized so that their polarization-averaged intensity ranges from “0” to “1”, as shown in Fig. 5.6a and upper panels of Fig. 5.7. The XLD spectra in the lower panels of Fig. 5.7 are the difference of these normalized spectra that were measured with horizontal and vertical polarizations; i.e., XLD intensity = horizontal intensity – vertical intensity. The XLD values in Fig. 5.6b are the maximum values extracted from the corresponding Co XLD spectra in Fig. 5.7.

The modification of charge across parameter space can also be tied directly, through X-ray linear dichroism (XLD), to the strength of the magnetic interaction in the ESO. Best data fits suggest that Co^{3+} is in the low spin state, which is nonmagnetic, and thus Cu additions, which promote a growing Co^{3+} fraction, decrease in the strength of the AFM character of the system (Fig. 5.6b) as the fraction of Co^{2+} decreases. Collectively, structural frustration from changing bond angles, magnetic dilution due to conversion of Co^{2+} to Co^{3+}, and glassy AFM in bulk samples [116], motivates an exploration of FM/AFM exchange bias, as this is known to be particularly susceptible to frustration of the magnetic lattice [11, 256].

5.4 Magnetic Analysis

FM/AFM exchange bias is known to be dependent on magnetic frustration of the AFM layer[217]. The spin glass model for exchange bias [295, 296] argues that frustrated magnetic moments at the FM/AFM interface couple to the FM magnetization, creating the characteristic bias field. The pinned surface moments are hard and slow to move, resulting in the exchange bias itself, and the degree of disorder, directly proportional to the thickness of the glassy layer, is dependent on the intrinsic order and anisotropy of the magnetic lattice in the AFM [296]. This model can be expressed as an energy balance using the system of equations:

$$\frac{H\mu_0 M t_F}{-Jf}\sin(\theta-\beta)+\frac{1-f}{f}\sin(2(\beta-\gamma))+\sin(\beta-\alpha)=0 \tag{5.1}$$

$$\frac{K_{AF}t_{AF}}{fJ}\sin(2\alpha)-\sin(\beta-\alpha)=0 \tag{5.2}$$

Where H is the applied magnetic field, M and t_F are the magnetization and thickness of the FM layer, J is the interfacial exchange energy, f is the fractional spin ordering, θ is the angle between the applied field and the anisotropy axis of the FM, β is the angle between the FM magnetization and the FM easy axis, γ is the angle between the applied field and the preferred orientation of the glassy layer, α is the angle between the surface magnetization of the AFM and the anisotropy axis of the AFM, and K_{AF} and t_{AF} are the anisotropy energy and thickness of the AFM

layer. Use of the Radu model here is motivated by: 1) a sluggish AFM/PM transition has been observed in bulk [116, 117], consistent with the phase having a glassy component. 2) Magnetic dilution is known to increase a glassy component in AFM systems (for instance CuMn alloys). 3) Such a strong correlation of structure, charge, and measured magnetic data agrees with our expectations.

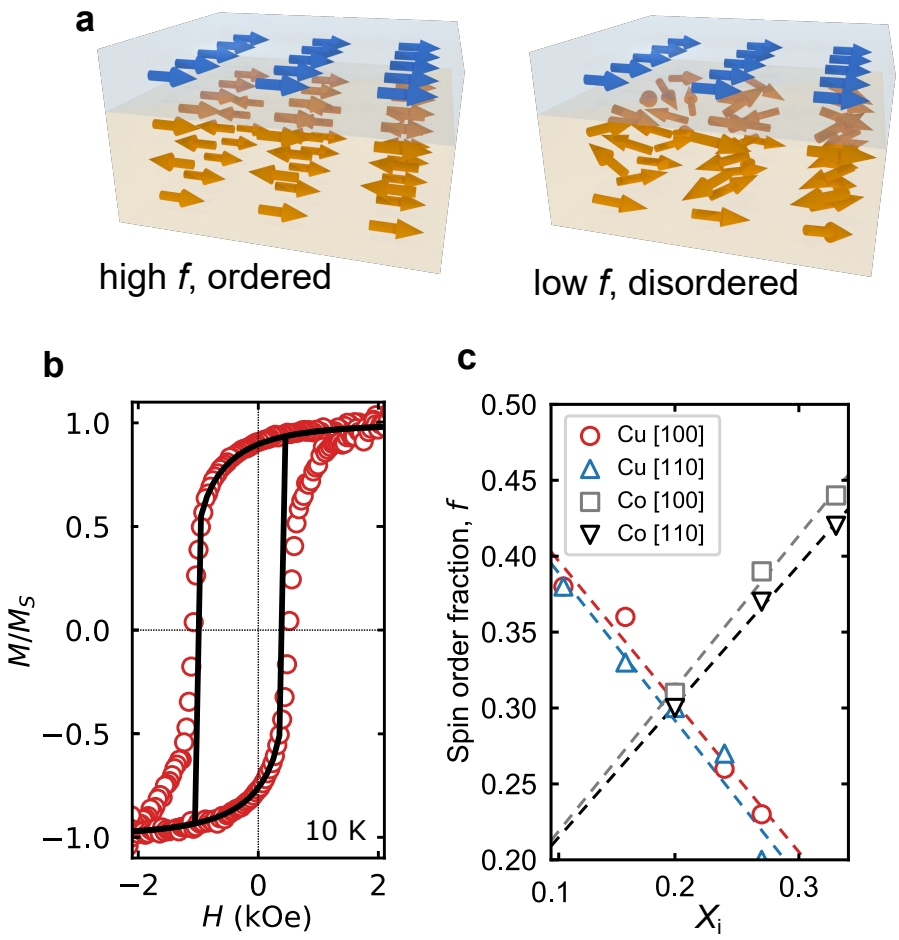

Figure 5.8: Magnetic distortion in Cu-variant films. a Schematic illustrating the spin lattice of the antiferromagnetic layer when it is highly ordered (high *f*, left) and highly disordered (low *f*, right). For simplicity the FM layer is depicted here in its saturated state. As the magnetic lattice of the AFM is frustrated, changes can be read out through the FM layer. **b** Normalized magnetic moment versus field for the equimolar composition at 10 K. Experimental data is shown with the open circles and the fit from the model is shown as a solid line. Fit corresponds to an R^2 parameter of 0.987. The sample was biased by cooling from 300 K in a 1 T magnetic field. **c** Spin ordering parameter *f* as a function of Cu and Co concentrations. As the concentration of Cu (red, blue) is increased, the magnetic lattice is increasingly disordered and as we increase the concentration of Co (grey, black), the degree of frustration decreases. Data is extracted from magnetic hysteresis loops taken at 10 K. Dashed lines are provided as guides to the eye.

To study magnetic disorder, we probe the parameter f, the fractional spin ordering at the interface, where $f = 1$ is the maximum ordering and $f = 0$ is the maximum disorder. This is shown schematically in Fig. 5.8a. For reference, the well-studied Co/CoO exchange bias system has shown a spin ordering of $f = 0.8$ [295]. Numerically solving the system of equations for the unknowns J, f, γ, and α (assuming $\theta, \beta = 0$) and fitting to experimental magnetometry data taken at 10 K, we obtain a quantitative measure of the magnetic disorder in our ESO exchange biased heterostructures. Fitting was accomplished by globally minimizing the goodness-of-fit (R^2) from approxiamtely 105 points in parameter space using least-squares analysis calculated in the region from large positive field until switching, and large negative field until switching. Approximately 10^5 solutions were calculated across the entire parameter space in a course, evenly spaced, grid to minimize R^2. This is then done again using a finer grid of points about the previously calculated minimum. List of parameters and visualization of the fits is available in Figs. 5.9 and 5.10. Anisotropy energies of the samples were calculated using the fits from above along the [100] and [110] crystallographic directions. An example of a fit hysteresis loop is shown in Fig. 5.8b. In all cases here, α is small ($\approx 0°$) and R^2 >0.94. As the concentration of Cu is increased in the oxides, we observe an approximately linear decrease in the spin ordering parameter, f (Fig. 5.8c). Our results indicate that the concentration of Cu is directly proportional to the degree of spin frustration in the magnetic lattice. This linear proportionality agrees with our results from XLD (Fig. 4.7b), which shows a linear decrease in the AFM character of the cation sites as Cu concentration is increased. Our observed value of f is small, even compared with the canonical spin glass, CuMn, studied in reference [232] (f = 0.65).

We posit that the significant magnetic disorder in the system is driven by the magnetic dilution and the superexchange interactions where tightly bound electrons in the oxide system are more easily frustrated by structural deformation than those of a delocalized, metallic antiferromagnet [297, 298]. Further, our experimental results correlate with the observed change in the bond angle distribution from theoretical calculations, providing evidence for this assertion, that the variance in cation-oxygen-metal bond angle is a primary driver of magnetic frustration in our ESO systems.

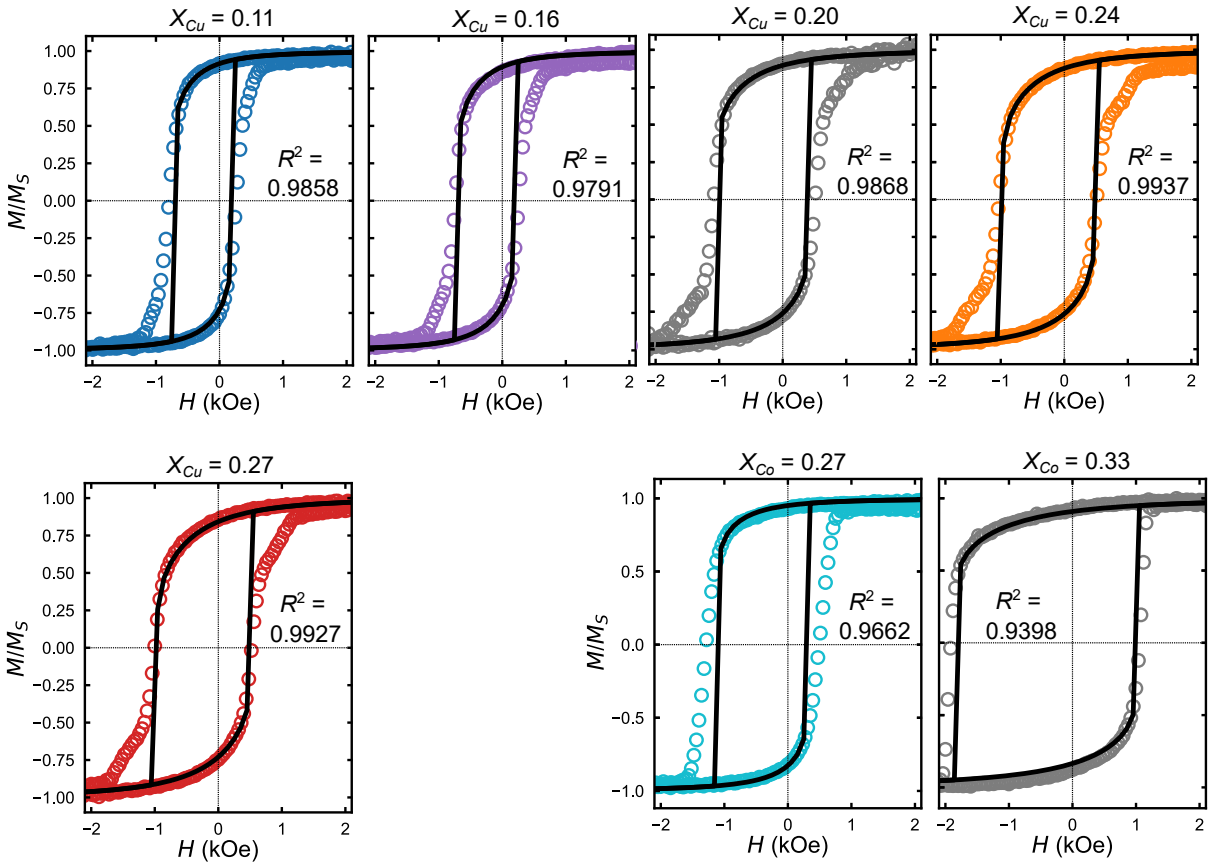

Figure 5.9: 100-oriented *M*v*H* loops of Cu- and Co-variant exchange bias stacks. Loops were taken at 10 K after cooling from 300 K in a 1 T magnetic field and after degaussing. R^2 values were calculated using the bottom leg of the hysteresis loop, from negative saturation field to the switching event at H_C^+.

This is also mediated by a difference in valence on the Co cation sites, driven by Jahn-Teller structural distortions, which results in dilution and disorder of the magnetic lattice. Additionally, inclusion of Co should result in the inverse effect as Co has a negligible influence on the structural disorder while increasing the number of AFM sites. Indeed, as the concentration of Co is increased in the Co variant samples, we observe an approximately linear increase in f, corresponding to a decrease in the spin disorder. This is complemented by XAS data showing that the Co^{2+}/Co^{3+} ratio becomes approximately invariant with Co incorporation, indicating that it primarily the change in average cation moment, rather than oxidation state, which is driving the observed trend.

This frustration can also be seen in the γ parameter extracted from the model, corresponding to the difference between the preferred orientation of the glassy layer

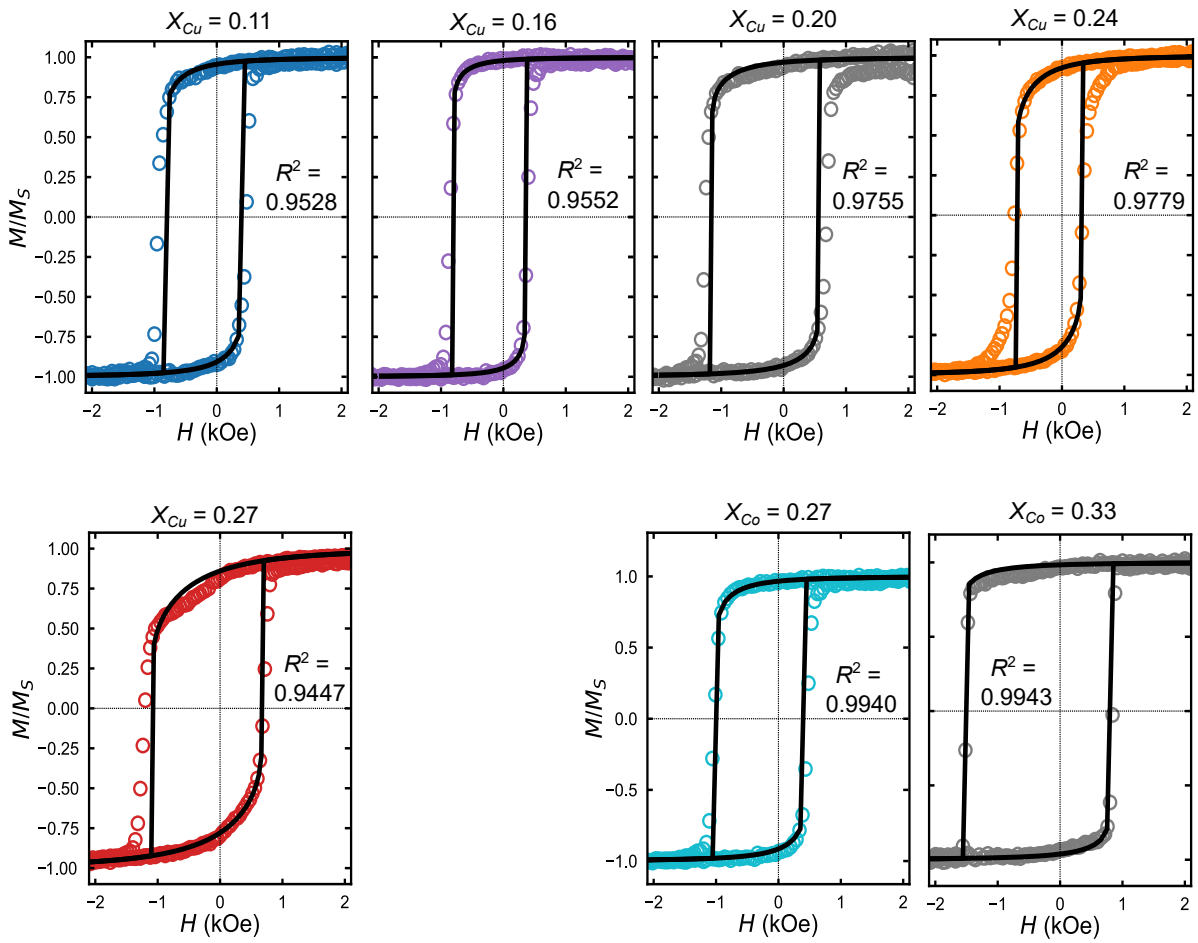

Figure 5.10: 110-oriented *M*v*H* loops of Cu- and Co-variant exchange bias stacks. Loops were taken at 10 K after cooling from 300 K in a 1 T magnetic field and after degaussing. R^2 values were calculated using the bottom leg of the hysteresis loop, from negative saturation field to the switching event at H_C^+.

and the measurement direction, similar to an enforced easy axis in the spin glass. As the concentration of Cu is increased in the oxide, the difference in γ along the [100] and [110] crystallographic axes approaches 0 (Fig. 5.11a). This indicates that the driving force for a preferred axis is weaker and the magnetic lattice becomes more isotropic with increasing Cu. Indeed, the anisotropy energies also show this, as the ratio A_{100}/A_{110}, the energies along the [100] and [110] directions respectively (calculated from $A_i = \int_0^{M_s} H(M)\mathrm{d}M$), approaches 1 with increasing Cu incorporation, showing that the ESO becomes more magnetically isotropic (Fig. 5.11b). Our data agree with our theoretically calculated bond angles in the ESO, as the bond angle is increasingly disordered in a linear fashion by the inclusion of Cu^{2+} (Figure 5.5e), and XAS data showing that the system becomes more magnetically dilute as Cu concentration increases.

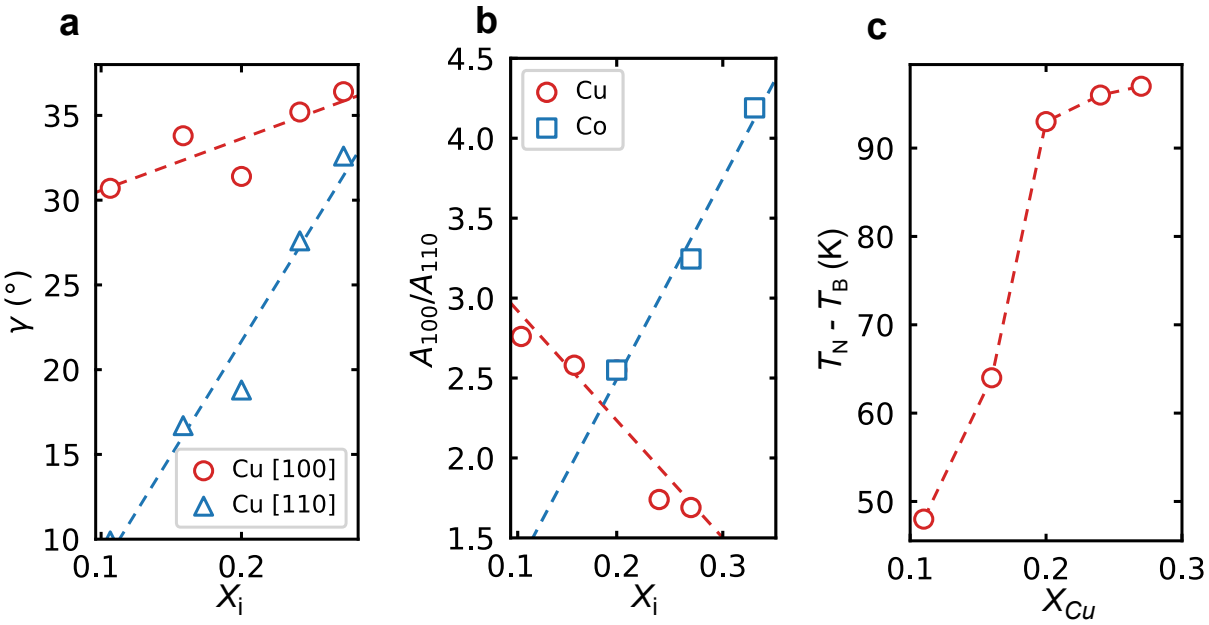

Figure 5.11: Magnetic anisotropy of Cu-variant samples. a Angle, γ, between the applied field and the preferred axis of the spin glass as a function of composition. As the concentration of Cu is increased, the difference between γ along the [100] and [110] directions approaches 0, showing that the magnetic lattice is tending toward isotropy with increasing Cu. **b**, Ratio between anisotropy energies for the [100] and [110] directions. As Cu concentration is increased, the ratio approaches 1 and the system tends towards isotropy. In contrast, as Co concentration is increased, the anisotropy becomes stronger and [110] becomes the preferred easy axis. Dashed lines in each plot are guides to the eye. **c**, Plot of the difference between T_N and T_B reveals the sluggishness of the transition, as a function of Cu concentration, indicating increasing glassiness in the ESO as Cu incorporation is increased.

Conversely, the ratio A_{100}/A_{110} increases with increasing Co inclusion, showing that spin frustration decreases and [110] becomes the easy axis. This agrees with previous results reported in ref. [11], as it was observed that the [110] axis becomes more favorable with increasing Co concentration. This is also in agreement with the magnetic structure observed in bulk experiments [116, 117] of the equimolar composition where an average G-type order with the Néel vector along the [111] emerges below the Néel temperature of approximately 135 K.

Moment versus temperature curves, Fig. 5.12, show a large separation between T_N and T_B, revealing sluggish paramagnetic/AFM transitions as observed in glassy systems [8] and in bulk (MgCoNiCuZn)O [116, 117]. The separation between these temperatures increases with increasing Cu concentration, illustrating that the system gets more frustrated with concentration (Fig. 5.11c) and providing further evidence of

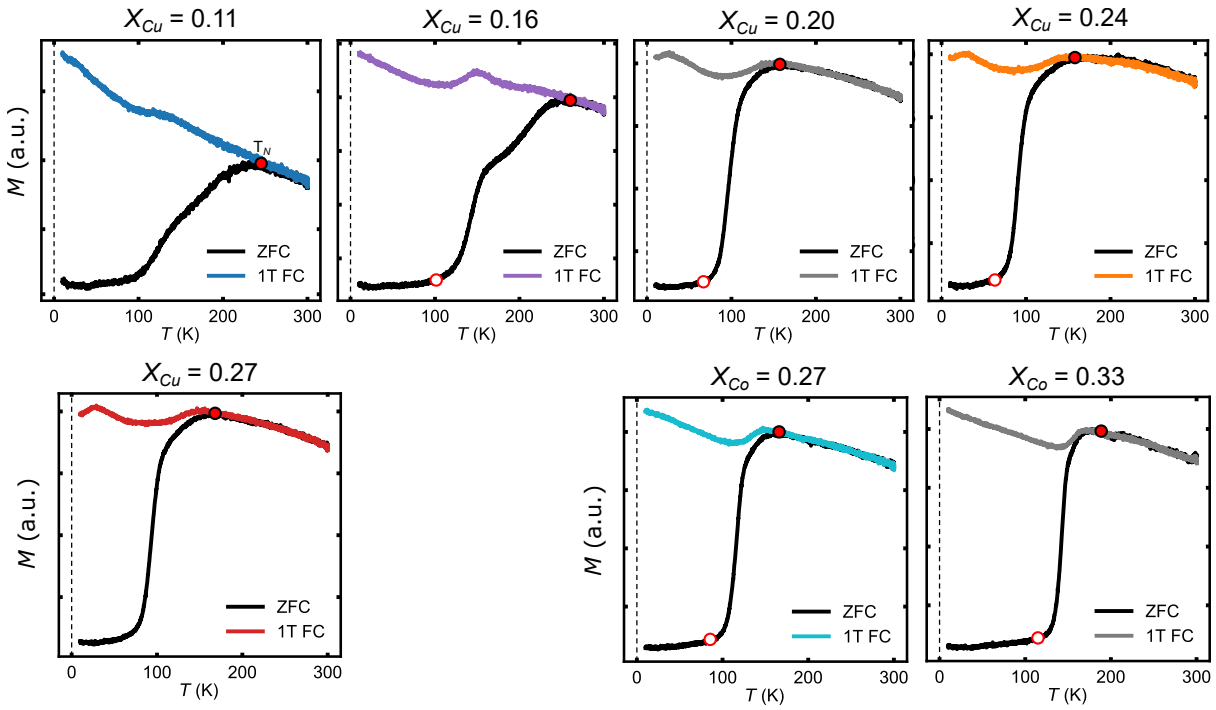

Figure 5.12: *M*v*T* of Cu- and Co-variant exchange bias stacks. The measured Néel temperatures (T_N) are marked with a closed circle and the blocking temperatures (T_B) are marked with an open circle. The high-Cu sample shows a nonlinear behavior at low temperatures that has been observed in glassy systems.

structurally driven glassiness. This observation is supported by the slow onset of the AFM state observed in bulk, as well as the broadening of the magnetic susceptibility peak from ref. [117] with the inclusion of increasingly frustrated cations.

In conclusion, we have demonstrated that using entropy-stabilized oxides, a large tunability of magnetic disorder can be achieved through correlations in lattice, charge, and spin disorder. By tuning the degree of stereochemical frustration in the material, we can tune the structural disorder to drive oxidation state changes in magnetically active cations and create a disorder in the magnetic lattice.

Chapter 6:

Conclusions and Future Directions for FeGa and ESOs

6.1 Summary of Results in Disordered Systems

The purpose of the work presented here has been to showcase how intentionally engineering disorder and frustration into materials can be used to tune functional properties in similar fashion to established thin film techniques like local chemical substitution [299] and epitaxial clamping [300, 301]. The results discussed within have demonstrated the ability to synthesize a novel, disordered phase of a magnetostrictive alloy, where this new phase boasts significantly enhanced magnetostriction, and the ability to control magnetic frustration in a relatively unexplored oxide chemistry.

In Chapter 2, I discuss my results on the synthesis of a disordered phase of FeGa, which demonstrates significantly enhanced magnetostriction when compared to the thermodynamic ground state. Part of the value in FeGa alloys comes from their relative sustainability and earth abundance, when compared to rare earth magnetostrictors like terfenol-D [14, 3]. A significant challenge in the use of FeGa for composite magnetoelectric applications, however, is that the magnetostrictive coefficient is limited by the phase diagram: λ increases with increasing Ga concentration up to approximately 19 at%, at which point the thermodynamically stable phase becomes an ordered in-

termetallic with lower magnetostriction. By depositing FeGa with low temperature epitaxy, I am able to kinetically freeze the disordered phase up to 30% Ga and prevent the magnetostriction from dropping. I measure the magnetostriction of the FeGa layer by observing the composite magnetoelectric behavior of the heterostructure and fitting that behavior to extract the relevant coupling coefficients. I find that, by stabilizing this disordered phase of FeGa, I can increase the magnetostriction by as much as 10x relative to bulk and reach magnetostriction coefficients competitive with, or better than, some of the best rare-earth-alloy magnetostrictors.

In Chapters 4 and 5, I discuss my results in tuning the magnetic frustration of HEOs with unexplored chemistries and properties. HEOs are a new class of materials that are often stabilized using the configurational entropy of a large number of cation species. In these systems, chemical, structural, electronic, and magnetic disorder are expected to be prevalent, but the youth of the field means that these structure-property relations oftentimes have yet to be explored. In my work, I investigate the ability to control functional disorder, in particular magnetic disorder, through the use of stereochemical frustrators. Because HEOs are stabilized with a significant contribution from entropy, typically immiscible species can be dissolved into the crystal to create new extremes of disorder and frustration. I observe that changes in the concentration of Cu in the system, a cation that will go through a Jahn-Teller distortion, progressively increases this structural disorder in the crystal. This, in turn, manifests as changes in the charge and magnetic lattices following the same trend, illustrating how intimately tied these phenomena are in the system a large degree of control with relatively small changes in chemistry. In contrast, changing the relative concentration of Co in the HEO, a cation that will happily sit on an octahedral site and is robustly magnetic, produces almost the opposite trend, where increasing concentration serves to decrease structural and magnetic disorder to an equivalent degree. This concept of entropy-stabilization provides a new tool to control the chemistry of materials and influence their associated functional phenomena.

In the remainder of this chapter, I will discuss the outlook for these material systems, as well as my own opinion on the next steps for advancement of the associcated

technologies, both with FeGa heterostructures and HEO magnets.

6.2 Scaling of FeGa Composite Materials

Through epitaxial stabilization of the disordered phase in FeGa, I have been able to show that a high-performance magnetostrictor, and thus a high-performance magnetoelectric, can be reliably synthesized [14]. Slow, low-temperature deposition of FeGa freezes the material into the disoredered A2, α-Fe-like phase. Preventing the formation of competing intermetallic phases allows the magnetostriction of the material to reach new heights, potentially becoming one of the best magnetostrictors in the field. The natural next step for the system, motivated by the potential to fabricate extremely-energy-efficient computing memory, is to scale the composite to characterize the magnetoelectric behavior at a more reasonable length scale. In Chapter 2, we discussed a device on the order of μm in size- for this composite material to be useful in computing applications, we have to start thinking about devices on a nm scale.

Extending the magnetoelectric behavior of the FeGa system discussed in Chapter 2 to a simulated device, we can use our μm-scale metrics to estimate an energy dissipation as these materials and devices are extended to more applicable, nm dimensions. Here, most of the energy dissipated per switch is during ferroelectric reorientation. This can be shown by simulating the energy dissipation during reorientation of the magnet using micromagnetics, for which details are given in ref. [14]. Simulations show that magnetic reorientation of a 45 x 45 nm^2 device, the smallest stable size where anisotropy is greater than thermal energy [4] (42 $k_B T$), is less that 1 aJ per 90° magnetic switching. The energy dissipation per switch from the ferroelectric can be extracted from the integrating half the ferroelectric hysteresis loop to result in approximately 2.9 mJ cm^{-2} per up-to-down switching event. This is using a ferroelectric substrate, but to reach more reasonable dimensions we can use a coercive field [302] of 30 kV cm^{-1} and aproximate the ferroelectric energy loss using $P_r V_C$ to estimate a switching energy of 5.9 μJ cm^{-2} for a 100 nm thick PMN-PT film. This value would give this system the best scaling of a normalized energy dissipation per switch

Table 6.1: Energy dissipation of beyond-Si techologies.

Technology	System	Energy Dissipation (μJ cm^{-2})
Spin torque	Co/Pt	4.4e4
Spin torque	TmIG/Pt	230
Single phase multiferroic	Co/BFO	280
Composite (FeGa) multiferroic	FeGa/PMN-PT	6

for a composite multiferroic [3], as shown below. Using this energy per area with our simulated device size, our ideal bit would have a switching energy of approximately 80 aJ, making these heterostructures competitive with other materials for beyond-CMOS technologies. To potentially reach these metrics, however, these devices must actually be realized, and that involves scaling both the magnetic layer and the ferroelectric layer.

In scaling the lateral dimensions of the magnet, electron beam lithography can be used to reach lengths on the 100s of nm. At this scale, however, measurement of devices is no longer trivial for a number of reasons including 1) simply contacting the devices, and 2) changes to longitudinal magnetoresistance may fall below the detection limit. In the measurements done in Chapter 2, devices are large and contact pads are on the order of 100 μm. this is because, with our testing apparatus, the sample must be wire bonded before it is measured and those bonds are on the order of 50-100 μm. This large of a contact would not be necessary with a probe station setup, but even then a 100 nm device is too small to land probes on. In this case, the FeGa nanopillar must be encapsulated in another large, nonmagnetic, Hall device that can be contacted more easily. This scheme has been used before in the spin torque community [303], where 200 nm diameter perpendicular magnetic nanopillars have been covered by a thin film of Pt to facilitate current collection. In this device, the Pt layer is functional and creates the spin-orbit torque to switch the nanodot, but in the case of the FeGa devices proposed here, it is a thin, conductive layer. In this device, enough current would be shared by the FeGa to give a measurable magnetoresistance. With a 5 nm Pt layer on top of a 15 nm FeGa film and a bar width of 5 μm, using the values for resistivity of FeGa extracted from the measurements in Chapter 2 ($\rho_{\text{FeGa}} \approxeq 133\text{e}{-6}\ \Omega$ cm) and Pt from [304] ($\rho_{\text{Pt}} \approxeq 20\text{e}{-6}\ \Omega$ cm), approximately 10% of the current is shared

by the FeGa through the cross section at the thickest point of a 200 nm cylinder.

In Chapter 2, the first order contribution to magnetoresistance is measured longitudinally, and thus the signal is a small deviation about a large offset resistance. In the case of the measured devices, this low-field AMR signal is approximately 0.05% of the measured offset (0.5 Ω deviation about a 1100 Ω signal). In the device suggested above, using 50 μA of current, this 0.05% signal would correspond to a voltage change on the order of 1 nV, which is potentially too small to measure about a 40 mV offset voltage. This necessitates measurement of the transverse signal, which has a similar dependence on the magnetoresistance. Longitudinal magnetoresistance is defined as:

$$\rho_{xx} = \rho_{xx,0} + \Delta\rho_{xx}\cos(2\theta) \tag{6.1}$$

where $\rho_{xx,0}$ is the longitudinal resistance and $\Delta\rho_{xx}\cos(2\theta)$ is the change in resistance which comes from $\mathbf{I} \bullet \mathbf{M}$, θ being the angle between the two. Transverse magnetoresistance can be defined as:

$$\rho_{xy} = \Delta\rho_{xy}\sin(2\theta) \tag{6.2}$$

which, being similar to a Hall effect, has no offset voltage other than device parasitics. These parasitic effects can be mitigated by changing the device terminals, as in a Van Der Pauw experiment, making this a more sensitive measurement for the detection of a small magnetization. In the device mentioned above [303] used by Bhowmik et al., the magnetization of the perpendicularly magnetized nanopillar is measured in the same geometry via the anomalous Hall effect, with a measured signal of approximately 1 Ω at 10^6 A cm^{-2}, corresponding to a 20 μV signal given their device geometry. Transverse magnetoresistance measured in FeGa has been observed to show similar signals to our own longitudinal measurements (ρ_{xy} = 0.04 $\mu\Omega$ cm) [77], which is small (on the order of nV) but may be detectable in a Hall configuration where the signal is measured about a 0. This may be a characterization challenge for miniaturizing these material systems, but the devices can be made smaller and smaller as the electronic measurements become more precise.

Electronic readout of this system should become more straightforward with a more

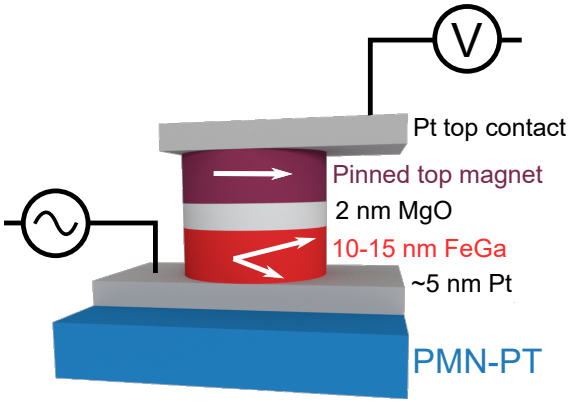

Figure 6.1: Proposed FeGa MTJ device. This system could be used to test lateral scaling of FeGa down to nm dimensions, where the direction of the free layer is controlled by strain anisotropy. Here, FeGa is grown on a thin Pt electrode which serves as a back contact, but still allows for epitaxial growth and strain transfer. The top magnetic layer can be pinned by either exchange bias, as in normal MTJs, or possibly by shape or crystalline anisotropy. Importantly, this layer must have an anisotropy component that cannot be overcome by magnetostriction or stray fields from the FeGa. In a real device, this nanopillar would be milled and then surrounded by an oxide layer that same thickness as the MTJ stack, to prevent shorting between the top and bottom contacts.

complex heteroepitaxial structure. While the transverse MR signal may be on the order of 0.05% of the input signal, on-off ratios of 100's of % at room temperature can be reached with construction of a MTJ [305, 306]. For this structure to work, a backing electrode must be developed to go between the PMN-PT and FeGa layers, to allow for vertical current flow through the heterostructure. This backing layer must be epitaxial to both the PMN-PT and the FeGa to keep the same phase stabilization properties explored in Chapter 2, and must be kept thin so strain from the FE can be efficiently transferred. In our preliminary explorations, Pt and Ir buffer layers have shown promise for this. The isolation layer could be MgO, since the Fe/MgO interface grows remarkably well and the Fe/MgO/Fe MTJ system is known to behave well [305]. The top magnet must then be a material with low magnetostriction, since, as MTJ structures have thicknesses on the order of 10 nm, there will be an appreciable transfer of strain even to the top magnetic layer. A proposed structure is shown in Figure 6.1.

In the absence of electronic transport, magnetization of structures on this length scale can be observed in other ways, particularly magnetic force microscopy (MFM), but possibly optical techniques such as MOKE and XMCD photoemission-electron-

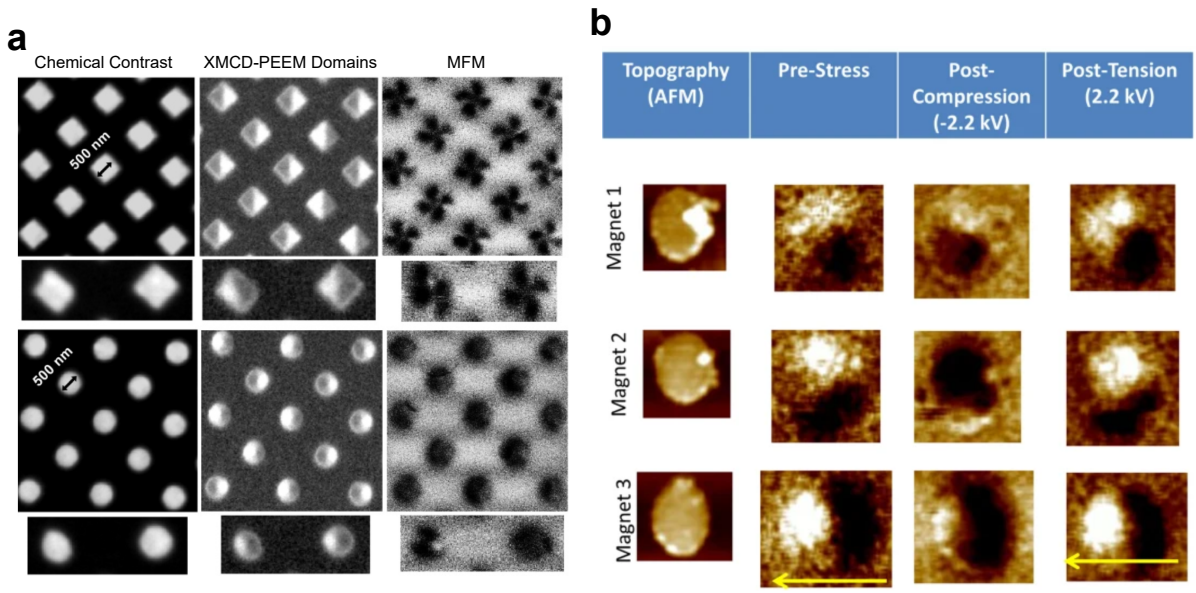

Figure 6.2: MFM and XMCD-PEEM of nanomagnets. a XMCD-PEEM and MFM images of LSMO nanopillars, showing clear domain patterns in magnets at a 500 nm scale. From ref. [307]. **b** MFM images of 300 nm FeGa nanodots on PMN-PT, suggesting switching of the magnetization behavior under different strain states. From ref. [51].

microscopy (XMCD-PEEM). MFM is used fairly widely to look at magnetic domain structures on the order of 100s of nm. In small magnetic nanopillars, and FeGa in particular, it has been shown that domains can be resolved in structures down to 300-500 nm [51, 307] (Figure 6.2). While switching can potentially be evaluated in the FeGa/PMN-PT system using this method, an issue eventually arises in the fact that MFM is slow, limiting measurements to the same quasi-static regime as the experiments in Chapter 2. To investigate the dynamics of switching and domain motion, optical techniques such as MOKE or XMCD-PEEM potentially have a niche [77, 41, 307], but the resolution of visible light, as in MOKE, may limit lateral resolution of the measurement, and thus of domains. Additionally, the large electric fields used in FE switching and birefringence may interfere with optical experiments if a PMN-PT substrate is used, which motivates scaling of the ferroelectric.

Scaling the thickness of the ferroelectric to minimize the energy dissipated and lower the required electric fields, is not as straightforward as the lithography process involved with the magnet. Reducing the thickness of a ferroelectric thin film is well known to give diminishing returns via Kay-Dunn scaling, e.g the coercive voltage increases nonlinearly with reduced dimension [308, 309]. Additionally, when ferroelectrics be-

come thin, they can start to become leaky, or lose ferroelectric polarization altogether [310, 311]. Looking further toward device engineering, a significant hurdle lies in the fact that a FE thin film will be epitaxially clamped to the substrate, severely limiting the possible in-plane actuation [312], which is needed for the FeGa device outlined here. Some studies have shown that patterning of the FE can reduce the clamping to the substrate, showing that the behavior of the material becomes more bulk-like as the aspect ratio becomes more isotropic [312, 313, 314]. It is still more desirable, however, to minimize substrate clamping in an arbitrary material without being restricted to specific geometries.

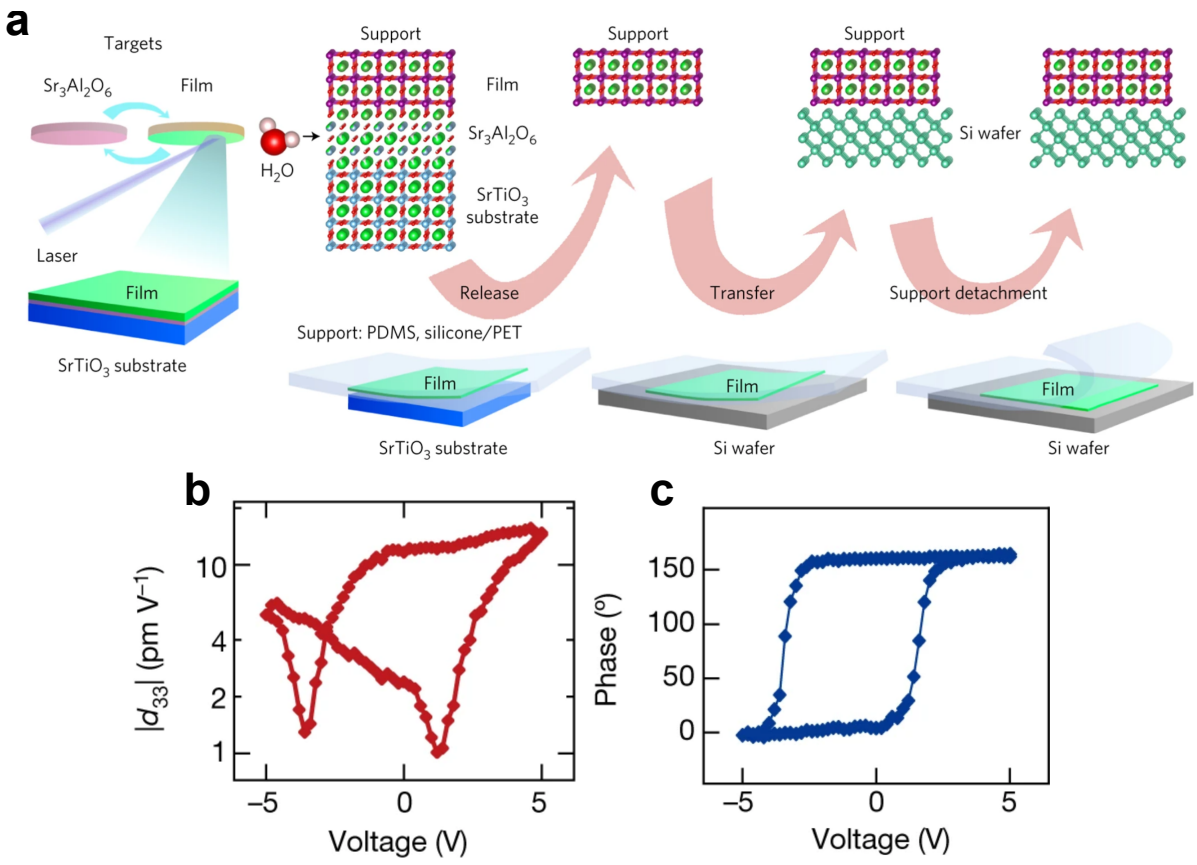

Figure 6.3: Exfoliation of oxide thin films. a Illustration of the process for exfoliating a perovskite film grown on SAO and a STO substrate. The film can be grown as normal via PLD, and then removed form the substrate and transferred to Si for easy characterization. From ref. [315]. Piezoelectric, **b**, and ferroelectric, **c**, loops from an exfoliated 4 unit cell BFO film, showing that the ferroelectricity is preserved is extremely small length scales, even after processing. From ref. [316].

More recent work has been exploring exfoliation of the FE, using a sacrificial layer in the heterostructure which can be chemically dissolved [317, 316, 318]. These works

have explored the use of LSMO and $Sr_3Al_2O_6$ (SAO) as sacrificial layers, which may be dissolved in a chemical etchant and water respectively, and have been developed in particular for the growth of functional perovskite oxides [315]. In the case of SAO, the unit cell is tetragonal and thus the 001 face boasts a square symmetry that matches well with materials like STO. Additionally, substitution of Ca for Sr does not alter the water-solubility, so the lattice constant of the sacrificial layer can be tuned to match perfectly with whatever is grown on top [315]. In practice, the heterostructure can be grown normally by PLD or MBE with the inclusion of 20-40 nm SAO. The stack can then be submerged in water for several hours while the SAO dissolves, and then transferred with a PDMS or PMMA stamp to a more functional substrate, such as a TEM grid or conductive Si. Post-exfoliation characterization of FE and magnetic films grown by this method shows comparable properties before and after (Figure 6.3b and c), indicating that the quality of the film is only minimally effected by the process. Further, ferroelectricity appears enhanced in ultra-thin exfoliated films, where substantial polarization is observed in BFO of only a few unit cells thick (Figure 6.3) [316]. This is attributed to a rhombohedral-to-tetrahedral-like phase transition as the film approaches the 2d limit and increased contributions of the surface polarization components. What this means, is that designing heterostructures in this way may have even further advantages beyond the removal of substrate clamping, allowing the normal size limits of ferroelectricity ot be circumvented.

These studies have shown that lithography of the transferred layer is possible [317], showing a process where, not only is the lateral substrate clamping minimized, electrodes can be tailored to an enormous degree, allowing for control of the surface and contact band offset to minimize leakage at small length scales. This is an exciting prospect for the field of multiferroics, and this proposed device in particular, showing that functional oxides can be deposited as normal and seamlessly integrated into Si-based processes. In the FeGa devices shown here, this technique could be used to scale the PMN-PT layer and maximize transverse strain generation. The heterostructure would be deposited as normal, with 20-40 nm of SAO below the PMN-PT layer. This would then be exfoliated and transferred to a conductive Si substrate, where lithography could occur as normal. Combining this with the above proposal of scal-

ing the magnet laterally, this would be potentially the optimal device for testing this mechanism at scale.

6.3 Functional Glassy Behavior in ESOs

As discussed in chapter 3, entropy-stabilization and high-entropy materials offer a potentially powerful system for the study of structure-property relations when it comes to disorder's influence on functional phenomena. One of the most important points for disorder driven functional phenomena is frustration of the order parameter, such as the competition of ferroelectricity/antiferroelectricity, resulting in relaxor behavior, and ferromagnetism/antiferromagnetism which drives magnetic glassiness. Recent studies in HEOs have demonstrated this ferroic frustration in magnetic systems [11, 12, 116, 117, 216], as well as to a limited extent structurally in perovskite oxides [167, 168]. Due to the large number of competing cation neighbors, these materials seem to be a model system for the demonstration of frustrated ferroic phenomena like strain, dipole, and spin glassiness.

Relaxor ferroelectrics, though being a long-studied and important class of materials, are still relatively poorly understood on an atomic scale. Though there is significant discussion about the mechanism of relaxor behavior, there seems to be consensus on the idea that this is caused by polar nano-regions (PNR) brought on by ferroelectric frustration [319]. Though the term "relaxor" is often used synonymously with relaxor ferroelectrics, non-ferroelectric ergodic relaxors (often used interchangeably with the term dipole glass) are a subset of phases which nominally show no macroscopic polarization, but a large frequency dispersion in the dielectric response. Analogous to a collection of magnetic nanoparticles, this effect is attributed to a collection of weakly interacting magnetic dipoles in a paraelectric matrix- similar to the PNR explanation for relaxor ferroelectricity [320, 321]. These materials are interesting for many of the same reasons as relaxor ferroelectrics and pyroelectrics, mainly the large, highly tunable frequency dispersion. As indications of super-spin glass behavior have already been observed and proposed in the magnetic lattice of ESOs [215, 116] (Figure 3.6)

and simulations of atomic scale features indicate an even stronger lattice distortion [12] (Figure 5.5), non-ergodic relaxor behavior may be present in these systems. Specifically, the distortion seen in DFT calculations, and the idea of high-entropy materials in general, implies a large number of structural ground states, which is one of the expected conditions for dipole glass behavior [322].

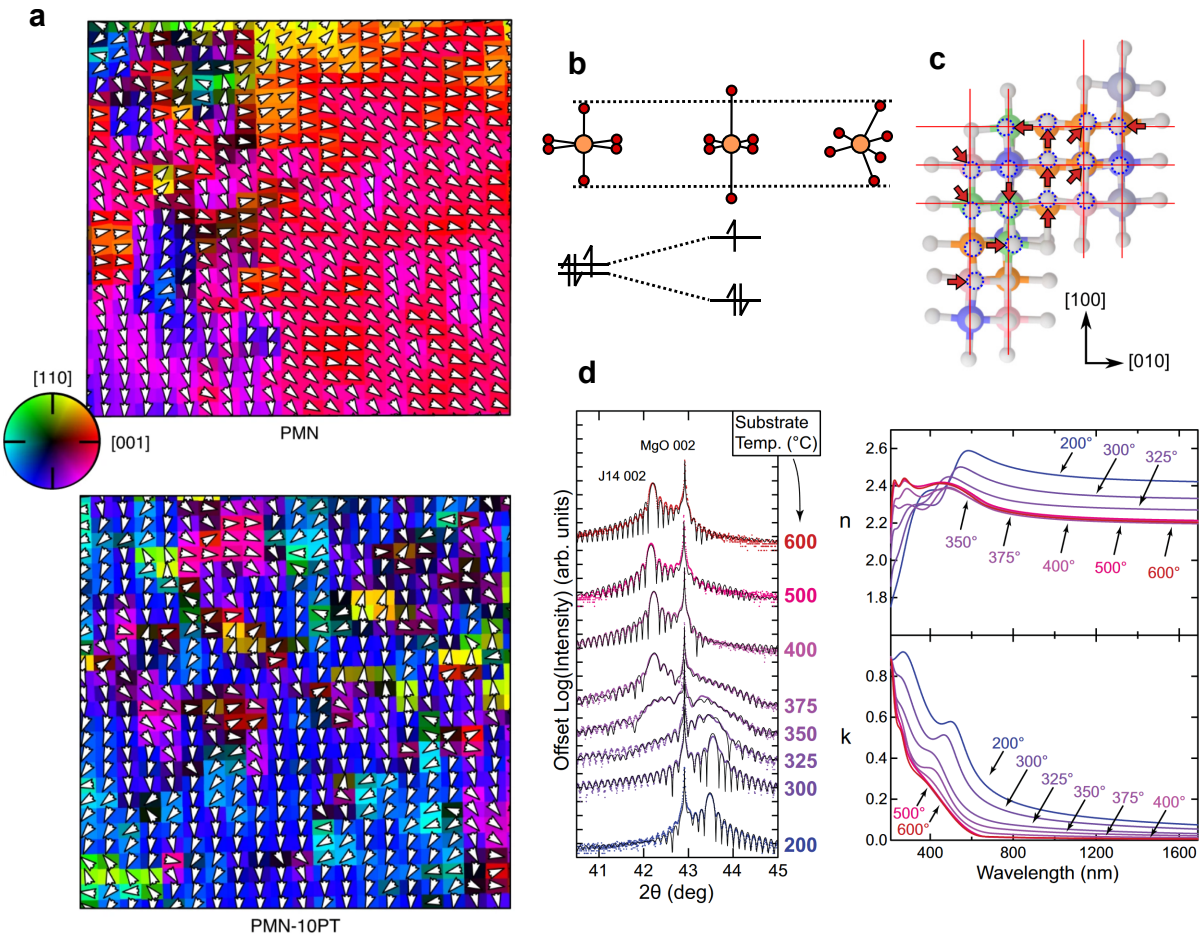

Figure 6.4: Dipole-glassy behavior in ESOs. a Composite image of dark field (ADF) and phase contrast (iDPC) STEM, showing the orientation of individual octahedral cages in relaxor PMN-PT. From ref. [323]. **b** Diagram showing the Jahn-Teller distortion in Cu containing ESOs and (**b**) how that frustration can apply across the whole lattice to potentially serve as relaxor dipoles. From refs. [12, 164] **d** Dependence of structure and the absorption edge on deposition temperature, indicating that even small changes in structure can result in large deviations of the dielectric behavior. From ref. [115].

Though ergodic relaxors may be difficult to characterize, due to the lack of macroscopic polarization, a recent study has been able to show pyroelectric currents and hysteretic permittivity from the nominally ergodic phase of PMN [319]. Additionally, advances in STEM analysis have allowed for the mapping of atomic scale polarizations in

relaxor ferroelectrics [323], which may be applicable to these materials. As discussed in Chapter 3, thus far, rigorous dielectric characterization of ESO has been lacking, potentially due to the difficulty in pulling single crystals, which precludes many of the normal dielectric/ferroelectric characterization methods. Deposition of the (MgCoNiCuZn)O ESO onto a reliable electrode, and then robust electronic characterization, would be a huge step forward for the development of the field and the understanding of structure-property relations in ESOs. Using normal magnetic characterization techniques [11, 12], it has been shown that the functional properties of even nominally boring crystal structures (e.g. rock salt) can be highly complex, and I expect that the electrical response will be no exception. Additionally, with optical probes of the dielectric function, it has been shown that the absorption edge is highly structurally dependent [115], which should only be more pronounced at the lower frequencies which can be associated with acoustic phonons and molecular polarization.

This paradigm can be further extended to glassy networks of other ferroic properties including strain glasses [324, 325] (analogous to ferroelastics), and multiglasses with multiple coupled glassy ferroic orders [326, 327, 328]. If dipole glass behavior can be demonstrated in these materials, it will be the first report in a non-perovskite system. Additionally, because it has been shown that magnetism is very sensitive to structure in (MgCoNiCuZn)O [12] and it can be extrapolated that a dipolar behavior relate to the lattice frustration will be dependent on the same phenomena, it is likely that these two phenomena are coupled and electrical poling can potentially be used to manipulate the spin glass.

A magnetic glassy response has been observed in bulk antiferromagnetic ESOs [116], likely stemming from the competition of superexchange interaction s between neighboring species [11, 215]. In my own unpublished experiments on ESO thin films, I have noted glass-like behavior in the DC regime, where the moment decays as a function of time (Figure 6.5). Fitting this behavior to a decaying exponential, $y = ae^{-bx}$, the decay amplitude and the time constant can be extracted. Looking at this phenomena as a function of the Cu concentration, and thus magnetic frustration, (as in Chapter 5), some trends becomes clear. The preexponential, a, increases as a function of compo-

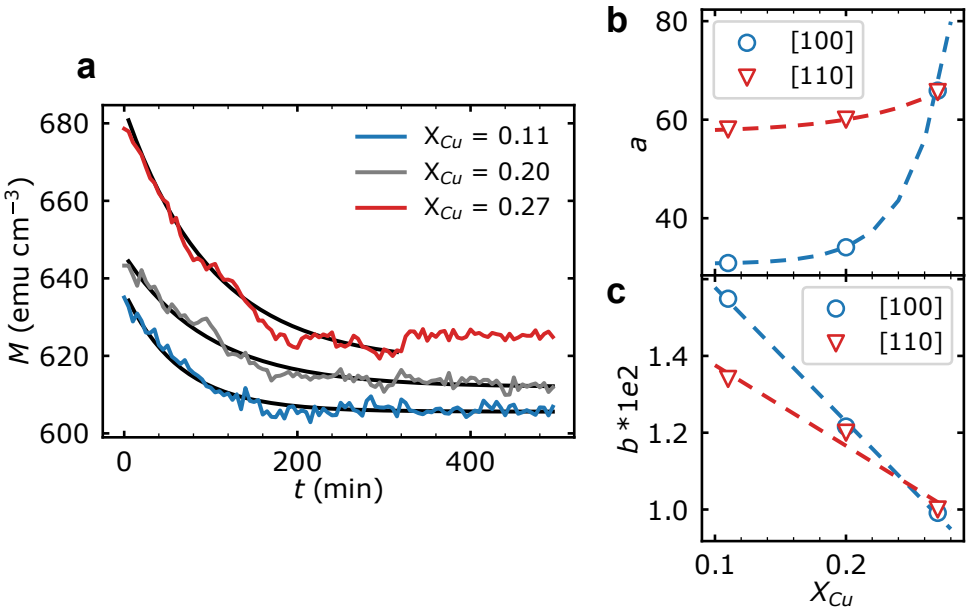

Figure 6.5: Moment decay in Cu-variant ESOs. a Temporal behavior of the magnetic moment in ESO exchange bias structures, varying over Cu composition. The absolute moment here corresponds to the moment of the entire structure, thus it can be assumed, that at t = inf the moment will decay to that of the Py layer. The curves are offset for clarity but, when this offset is removed, they decay to approximately the same value at t = 500 min. In the case of the curve at x_{Cu} = 0.27, the range of the instrument changed at t = 300, explaining the step and data after that point is not included in the fit. When this data is fit (black line) to a decaying exponential $y = ae^{-bx}$, the preexponential, **b**, and time constant, **c**, show clear trends in composition. These show slight differences with different crystallographic axes, likely dependent on the magnetic anisotropy, which points along [112] in the ESO.

sition, and the time constant, b, does the opposite, decreasing with increasing composition. An increase in a implies that there is a larger contribution from stereochemically frustrated spins as concentration increases, which agrees with the findings in ref [12]. The other point to note here is that, with the artificial offset removed, the curves equilibrate the approximately the same value and the initial moment scales proportionally to the Cu concentration. This further agrees with my previous findings, as it might be expected that the higher degree of frustration in Cu-rich samples leads to an additional frustrated-AFM contribution to the moment of the heterostructure. A decrease in the time constant with composition indicates that the moment decays more slowly at higher Cu concentrations, which is a more complex behavior, but to 0-th order may imply that interaction between moments is more frustrated, and thus slower, at higher levels of structural disorder. While these results are certainly not comprehensive, they do indicate that the magnetic behavior of the system is complex on timescales of hours to days, which is one of the indicators of a spin glass [329, 225, 210].

To investigate potential coupling of these glassy phenomena, magnetic characterization under constant electric field may be a valuable experiment. If the rock salt ESO is a dipole glass, constant electric field should help to align the dipoles within the material. Because exchange bias is so sensitive to the magnetic frustration associated with these displacements, the coupling may appear as a change in the exchange anisotropy or a change in *f*, the magnetic frustration of the AFM [12]. This measurement would, however, like dielectric characterization, require robust growth of the material on an electrode to allow a through-thickness electric field. It has been suggested that (MgCoNiCuZn)O can be grown on a Si substrate [108], but, in practice, this has not been explored. A Fe interlayer may also be a good route, due to the ease of growth of MgO on Fe [330, 305]. If these synthesis techniques are developed, it will open the door for a wealth of research into the use of ESOs for electrical, and potentially multifunctional, materials.

Appendix A:

PLD and Fast Quenching of Metastable Species

The ability to deposit materials at a low growth temperature is what allows for stabilization of the deeply metastable phases studied here. Particularly with PLD, but also true to a lesser extent with sputtering and MBE, the kinetic energy of the plasma is very large, on the order of 1-10 eV [37, 331], corresponding to an effective temperature on the order of 10^5 K. This combined with a low substrate temperature, e.g. 300 °C, creates a large effective quench that aids in the stabilization of the high temperature phase, in the case of ESOs [110]. Additionally, the low substrate temperature makes diffusion slow, preventing the dissolution of the metastable phase. Effectively, at a low deposition temperature, materials will be in whatever phase the are immediately deposited into. This makes epitaxial templating extremely important in these systems, as slow diffusion makes the crystal structure of the substrate very impactful for templating the correct structure, and the resultant strain field will further help to stabilize the phase.

The purpose of this appendix is to provide guidelines for ESO and FeGa deposition by PLD. It does not take the place of an SOP, but supplements it with information that I think is important for growth of these specific materials.

A.1 PLD of rock salt ESOs

Rock salt ESOs like (MgCoNiCuZn)O grow best on MgO (001) substrates. This is because, for the reasons mentioned above, epitaxial templating provides a seemingly large fraction of the stabilization energy. The growth of (MgCoNiCuZn)O on MgO is, in particular, extremely robust and high quality, single crystal films are achievable in a wide range of temperatures (around 200-700 °C), pressures (demonstrably vacuum-300 mTorr O_2), and fluences (very low to around 4 J/cm^{-2}). My standard conditions for this material and for attempting any new rock salt ESO composition are 300 °C, 50 mTorr O_2, 3 J $^{-2}$ (300 mJ, 10.5 cm lens distance on our system).

Starting with the target, I have found that the processing condition of home made ESO targets has a significant effect on the final sample. Targets ground by hand should be ground, sintered, and then ground again to get something homogeneous and dense. I hand grind targets for at least 2 hours, but I use a lot of force, so others may need to go for different amounts of time to achieve the same consistency. In my experience, the particles should be fine enough that the dust holds the pattern of a finger/glove print. **If the samples are not ground enough, deposited films wont have nice Laue oscillations.** For cold pressing, I like to use a little bit of acetone in the die to facilitate grain motion. I usually press at 1.5 Tons for around 30-45 minutes. Too much pressure will crack the greenbody and the sample needs to have enough time to densify. Targets should also be polished with a polishing plate (the big glass disk) under the SiC paper, or on a benchtop. The surface of the fumehood is rubber and is flexible enough to create a significant convexity in the target surface.

Substrates mounted to the platen with silver paste should be baked at around 60 °C for 10-15 minutes. The temperature is less important for 5x5 mm^2 samples, but for anything larger, a higher temperature will evaporate the solvent out of the silver paste too quickly and result in large bubbles, ruining thermal contact. **Before deposition, MgO also needs to be baked in the chamber at 950 °C for 30 minutes.** MgO substrates tend to be very poor, with a high degree of surface contamination and bad surface structure [332, 333]. The easiest way to compensate for this is annealing in

vacuum, where contaminants will fall off and grains will flow/decompose to result in a cleaner, single crystallographic domain surface for growth. Skipping this step can ruin the growth, so I always bake it into my routines. My process flow is then: load the sample, bake at 950 °C for 30 minutes in vacuum, bring down to growth temperature, deposit, cool in O_2. I usually cool in 200 sccm (approximately 1 Torr) of O_2, mainly so it will cool faster and the surface will be closer to nominal stoichiometry. This is, however, very different than the growth pressure and I have seen indications of different oxygen chemistry between the surface and the bulk, so this may be something that needs investigation.

A.2 PLD of FeGa alloys

The most important thing when depositing FeGa by any method is that it will not grow unless there is a seed layer. **I usually use a 1-2 UC layer of elemental Fe to seed the FeGa** because, for whatever reason, it will not grow on bare MgO or PMN-PT. Our collaborators have been able seed it with other TMs, for instance Ir, but in general it needs an Fe layer to template off of. I would hypothesize that this has something to do with the magic Fe-O interface formation and that Ga has a hard time bonding to the O in a rock salt configuration, but we have not investigated this. It is important to make sure the Fe layer is thin so there is no appreciable magnetic signal from it.

While everything above about substrate care remains true for MgO; PMN-PT, BTO, PZT, etc. can not be baked in the same fashion because titanates shed oxygen at high temperatures and become conducting, ruining the ferroelectricity. These crystals are also very fragile, so care must be taken when heating over large temperature spaces. This shedding of oxygen and surface conductivity also happens when titanates are ion milled, something very relevant for this project. In this case, the dangling bonds can be trimmed by a quick HF etch, which makes the oxide insulating again.

Something to keep in mind with PLD, in general, is that materials can only be grown for a certain number of shots before the surface of the target starts to roughen

and form periodic structures [334, 335, 336]. This occurs because of interactions between the incident light and the boundary conditions of the surface, which is much more pronounced in metal targets because they reflect so much of the incident light compared to oxide targets. This effect is even more pronounced in FeGa, presumably because heating and functionalization of the target leads to alloy segregation and phase changes. This is not something that can be circumnavigated easily on our system and, in general, **FeGa targets can only be deposited from for about 10,000 shots before they have to be repolished.** The saving grace here is, since metals have much more plastic crystal structures than oxides, these 10k shots can be grown at much higher fluence than is used with oxides. I often remove the aperture from the excimer beam when I grow metals, which does effect the laser spot but that is less important with a metal, and I can reach growth rates in FeGa that approach 75 nm per 10k shots. Do note, though, that this trick may only be possible since these are solid solutions and growth of an intermetallic may need finer control over the beam spot.

Appendix B:

Calculation of Magnetic Anisotropy

In a lot of the analysis shown here, particularly in Chapter 2, fitting of the magnetic hysteresis loop and calculation of the K_1 anisotropy energy is important. The K_1 coefficient can be determined from an integral of the hysteresis loop [127],

$$A_{hkl} = \int_{M_r}^{M_S} H(M)\mathrm{d}M \tag{B.1}$$

where [hkl] is the crystallographic axis, and

$$K_1 = 4\left(A_{110} - A_{100}\right). \tag{B.2}$$

Graphically, this integral corresponds to the area above the hysteresis loop from M_r to M_s, e.g. a perfectly square hysteresis loop will have an $A_{ijk} = 0$ and a perfectly hard axis will maximize the term. Given VSM data, this integral can be easily computed numerically with numpy.trapz(). If the absolute moment of the film is large, this integral is trivial and the confidence is high. If the moment is small, however, as in the case of a <10 nm film, noise is significant and error should be computed more rigorously. The most straightforward way to fit this data is to use an approximate of the Langevin function, Atanh $\left(\frac{x}{B}\right)$ + C, which works well enough to smooth ferromagnetic data in the pre-switching regime. Because this is a fairly simple fit, I generally just use numpy.curve$_f$it(), as is shown in Figure B.1. The error here can then be somewhat rigorously analyzed by looking at the standard error of the fit and propagating it to the calculation of K_1. A simple functional to calculate A_{ijk}, K_1, and the associated errors is included below.

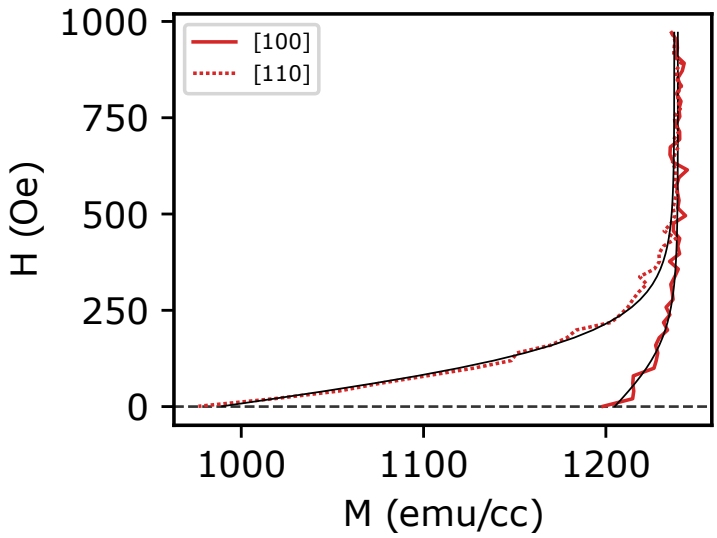

Figure B.1: Calculation of magnetic anisotropy. Plot showing the fit and analysis for a magnetic hysteresis loop of a 10 nm FeGa film. Because the film is thin, and M_S is approximately 200 μemu, the data is noisy and needs to be fit to tanh(x) + C. This fit is shown in black.

```
from scipy import interpolate
from pylab import *
import scipy.integrate as sp
from scipy.optimize import curve_fit



def vsmread(filename):
  with open(filename, 'r') as readfile:

  datalines = readfile.readlines()[13:]

  H = []
  M = []

  for line in datalines[:-4]:
    temp=line.strip('\n').strip('\t').replace(' ','').split('\t')
    H.append(float(temp[0]))
    M.append(float(temp[1]))
  H = np.array(H)
  M = np.array(M)
  return(H,M)
```

```
######
V=2e-7  # Volume of the magnet in cc

def proc(filename):
  H1, M1 = vsmread(filename+'.txt')
  m, b = polyfit(H1[0:20], M1[0:20], 1)
  Mfit = m*H1
  Ma = M1-Mfit
  Ma = Ma/V
  Ma = Ma-(max(Ma)+min(Ma))/2 #centering
  return(H1, Ma, filename)

def anisotropy(f1, f2, e):

  #####
  H1, Ma, F = proc(f1) # f1, f2 are the file names
  H2, Mb, F = proc(f2)
  #     Mb = Mb/max(Mb)*max(Ma)
  Mb = Mb/Mb[0]*Ma[0]
  #####

  H1a = H1[0:e]
  M1a = Ma[0:e]

  H2a = H2[0:e]
  M2a = Mb[0:e]

  #####

  def func(x,a,b,c): #fit to pseudo Langevin function
    y = a*np.tanh(x/(200+b))+c #(200+b) is an easy way to fudge an
                               initial guess with curve_fit
    return y

  def stderr(y, fit):
    temp = np.sum((fit-y)**2)
    return (temp/(len(y)-2))**0.5
```

```
popt1, pcov1 = curve_fit(func, H1a, M1a)
M1afit = func(H1a,*popt1)
M1err = stderr(M1a,M1afit) # standard error of the fit

popt2, pcov2 = curve_fit(func, H2a, M2a)
M2afit = func(H2a,*popt2)
M2err = stderr(M2a,M2afit)



#####

#     A100 = sp.trapz(H1a[::-1], x=M1a[::-1])
#     A110 = sp.trapz(H2a[::-1], x=M2a[::-1])

A100 = sp.trapz(H1a[::-1], x=M1afit[::-1])
A100err = abs(H1a[0]-H1a[-1])*M1err # propagate error to the
                                    integral with sigf^2=(df/dx)^2sigx^
                                    2
A110 = sp.trapz(H2a[::-1], x=M2afit[::-1])
A110err = abs(H2a[0]-H2a[-1])*M2err

#####

V=1e-6 # not actually volume, but conversion from J/cc to J/m^3

A1V = A100*V
A11V = A110*V #J/cc

A1Verr = A100err*V
A11Verr = A110err*V

con = 6.24e18 # eV/J

####
## generate the figure
figuresize=[3,2.2]
left = .25
right = 0.95
```

```
    bottom = .17
    top = 0.90
    f = plt.figure(figsize=(figuresize[0],figuresize[1]), dpi=200,
                                        facecolor='w', edgecolor='k')
    f.subplots_adjust(left=left,right=right,bottom=bottom,top=top)
    plt.rc('axes', linewidth=1)
    ax = plt.subplot(111)
    ll=1 # linewidth

    ax.axhline(0,color='k',lw=0.75,linestyle='--', alpha=0.8)
    plt.plot(M1a, H1a, tr, lw=ll,  label = '[100]')
    plt.plot(M1afit,H1a,'k',lw=0.5) ### plot of the fit
    plt.plot(M2a, H2a, tr,dashes=das, lw=ll, label = '[110]')
    plt.plot(M2afit,H2a,'k',lw=0.5) ### plot of the fit
    plt.xlabel('M (emu/cc)')
    plt.ylabel('H (Oe)')

    leg = plt.legend(loc=2, fontsize=6)

    plt.savefig(f1+'.pdf', format='pdf')
    #     plt.xlim([950,1275])

    ### print values

    print('A100',A1V, 'A110', A11V)
    print('A100/A110', A1V/A11V)
    print('A100 error', A1Verr, 'A110 error', A11Verr)
    print('')
    K1 = (A1V-A11V)/4*1e6 # J/m^3
    K1err = (A1Verr**2 + A11Verr**2)**0.5 /4*1e6
    print('K1', K1, 'K1err', K1err)

    return(A1V, A11V, A1Verr, A11Verr, K1, K1err)
```

Appendix C:

Calculation of PFM Switching Maps

The PFM switching maps shown in Figure 2.4 were calculated by recording PFM signals from both the IP and OOP directions, rotating the sample by 90°, then doing PFM in the same way. Doing this, the 3D direction of the polarization can be determined. Here, the OOP signal will correspond to the OOP polarization, the first IP direction will correspond to the +x and -x directions, and the second IP polarization will be the +y and -y directions (these particular directions are arbitrary and will vary depending on how the sample is rotated). The scan direction here matters, because 1) the flexure of the cantilever will be more sensitive in the direction perpendicular to the scan, so if you scan from left to right, the up down flexure of the cantilever will be more sensitive. 2) scanning in different configurations will rectangularly distort the image slightly, so for images to be lain on top of one another, the scan direction needs to be the same.

The ND-MDT AFM has good internal lockin and so is more than fine for characterization purposes, but I take issue with the fact that I can not easily change the time constant of the internal lockin, so I always use external lockins for important data collection. (show diagram of connection for external lockins)

After the data is collected, I process it in Gwyddion and export it as a txt file. This outputs a 2D array, which is really easy to conceptualize and work with in python/Matlab. PFM data should be a bimodal (or trimodal, if there is an area whit no signal) distribution of color values, so using the color picker in Gwyddion, I can choose the value in between the peaks to separate the data into + and - values (this is commented

in the code below). Plotting these binary-valued PFM matrices in python gives the images shown in Figure C.1, and allows us to construct the composite 3D matrix, where the 3rd dimension corresponds to the z, y, and x components of the polarization vector.

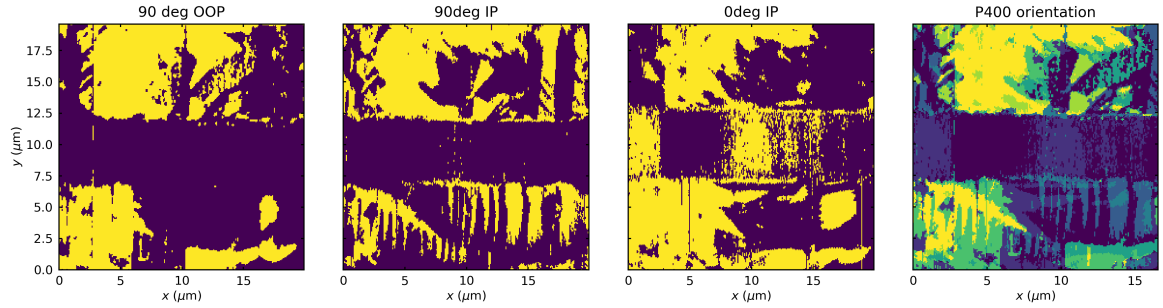

Figure C.1: PFM micrographs read into python. PFM micrographs showing OOP and IP components of polarization exported from Gwyddion and read in python. The last micrograph shows the composite image of the first three, which correspond to the z, y, and x components of the polarization respectively. The bar in the center of the image is the device.

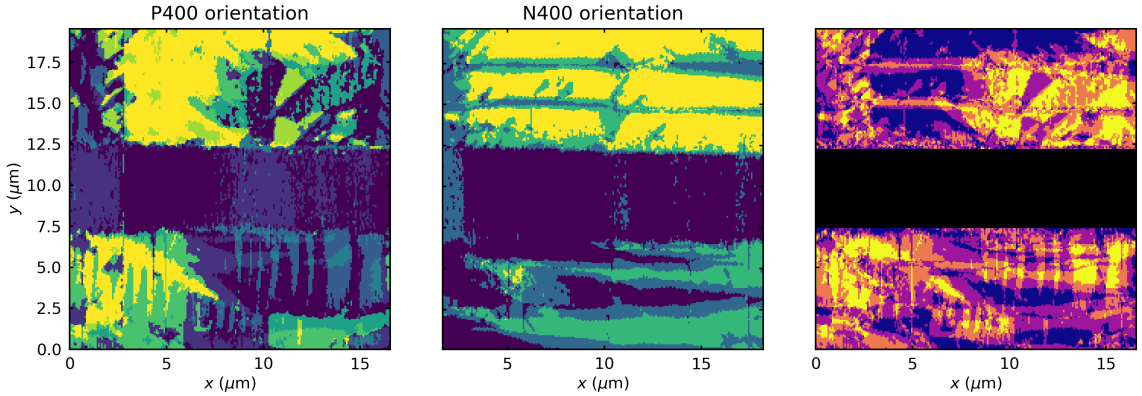

Figure C.2: PFM switching map. PFM composite micrographs showing the 3D polarization vectors both before and after switching. The angle between these two data sets at every pixel can then be calculated and shown as the third map of switching angle per area.

The way I have written this code, the images need to be aligned manually, but given the distortion caused by rotating the sample and by the different scan profiles, this is the best way to do it with out current setup. Scanning over a device is the best way to do this, as the topographical features can be aligned. Once the composite has been constructed, the second image after switching needs to be processed in the same way and the two need to be aligned again. At this point, the angle at every pixel between the two polarization vectors can be calculated and a third map of switching angle can

be constructed. The code used in the calculations done in Chapter 2 is included here.

```
# %matplotlib notebook
## code to analyze PFM switching maps from txt files output by
                                    Gwyddion
## author: Peter Meisenheimer
## last updated: 1/14/21

######
### functionals

import numpy as np
import os
import csv
import matplotlib.pyplot as plt
from pylab import *
from matplotlib.ticker import AutoMinorLocator
from scipy import signal
import matplotlib.colors as mcol
import matplotlib.cm as cm

######



def txtread(filename,threshold,val):
  data = []
  with open(filename+'.txt', 'r') as readfile:

  datalines = readfile.readlines()

  for line in datalines:
    temp=line.strip('\n').split('\t')
    temp = np.array(temp,dtype=float)
    data.append(temp)

  data = np.array(data)

  for i in range(len(data)):
```

```
    for j in range(len(data)):
      if data[i][j] > threshold:
        data [i][j] = val
      else:
        data[i][j] = -1*val

  for i in range(len(data)-1):
    for j in range(len(data)-1):

      if data[i][j] !=  data[i+1][j] and data[i][j] !=  data[i-1][j
                                ] and data[i][j] !=  data[i][j+1]
                                and data[i][j] !=  data[i][j-1]:
        data[i][j] = data[i+1][j]

  return np.flipud(np.array(data))

#######
### figure design
def figfig():

  figuresize=[4,4]
  left = .2
  right = 0.9
  bottom = .2
  top = 0.90
  f = plt.figure(figsize=(figuresize[0],figuresize[1]), dpi=300,
                                facecolor='w', edgecolor='k')
  f.subplots_adjust(left=left,right=right,bottom=bottom,top=top)
  ax = plt.subplot(111)
  ll=1 # linewidth
  ts=10 # title size
  al = 1
  mm = 3
  plt.rc('axes', linewidth=1)
  plt.tick_params(axis='both', which='major', top=True, right=True,
                                labelsize=ts, length=2.5, width=1,
                                pad = 5, direction='in')
  plt.tick_params(axis='both', which='minor', top=True, right=True,
                                labelsize=ts, length=1.5, width=0.5
```

```
                                    , pad = 5, direction='in')
  ax.set_xlabel(r'$x$ ($\mu$m)', fontsize=ts, labelpad=2)
  ax.set_ylabel('$y$ ($\mu$m)',fontsize=ts, labelpad=2)
  return(f)

########
def unit_vector(vector):
  for i in range(len(vector)):
    if vector[i]==4 or vector[i]==2: #convert back to real
                                    coordinates from the easy sum
      vector[i]=1
    elif vector[i]==-4 or vector[i]==-2:
      vector[i]=-1

  return vector / np.linalg.norm(vector)

def angle(v1, v2):
  v1_u = unit_vector(v1)
  v2_u = unit_vector(v2)
  return np.arccos(np.clip(np.dot(v1_u, v2_u), -1.0, 1.0))
```

```
# % matplotlib notebook
########
### S2 +400V

res = 256
l = 20

#x = np.linspace(0,res,res) #pixels
#y = np.linspace(0,res,res)

### create x,y corredinates for mapping
x = np.linspace(0,l,res)# microns
y = np.linspace(0,l,res)

[xx,yy] = np.meshgrid(x,y)
```

```
## import files

filename = 'S2/S2_+400_right_OOP'
cv2 = 8.92 # center value
d2 = txtread(filename, cv2, 4)
# d2 = txtread(filename, cv2, 1)

filename = 'S2/S2_+400_right_IP'
cv3 = 10.777
d3 = txtread(filename, cv3, 2)
# d3 = txtread(filename, cv3, 1)

filename = 'S2/S2_+400_down_IP'
cv4 = 1.119
d4 = txtread(filename, cv4, 1)



#######
# do manual alignment
snipl1 = 1 #trim from the left of the image
snipb1 = 5 #trim from the bottom of the image

f1 = figfig()
plt.title('90 deg OOP')
plt.pcolor(xx[:-snipb1,:-snipl1],yy[:-snipb1,:-snipl1],d2[snipb1:,
                                snipl1:])
plt.savefig('OOP.png', format='png') # save as png's because having
                                 eveythinga s vector graphics is
                                too much for inkscape to handle


f2 = figfig()
plt.title('90deg IP')
plt.pcolor(xx[:-snipb1,:-snipl1],yy[:-snipb1,:-snipl1],d3[snipb1:,
                                snipl1:])
plt.savefig('90IP.png', format='png')

f3 = figfig()
plt.title('0deg IP')
plt.pcolor(xx[:-snipb1,:-snipl1],yy[:-snipb1,:-snipl1],d4[:-snipb1:
```

```
                                    ,:-snipl1])
plt.savefig('0IP.png', format='png')

####
## create composite map
s2P400 = np.array( [ d2[:-snipb1,snipl1:], d3[:-snipb1,snipl1:], d4
                                    [snipb1:,:-snipl1] ] )

# f4 = figfig()
# plt.title('P400 orientation')
# plt.pcolor(xx[:-snipb,:-snipl],yy[:-snipb,:-snipl], np.sum(P400,
                                    axis=0), rasterized=True)
# plt.savefig('S2before.pdf', format='pdf')
#####
#####

### S2 -400

x = np.linspace(0,l,res)# microns
y = np.linspace(0,l,res)

[xx,yy] = np.meshgrid(x,y)

## read second set of files
filename = 'S2/S2_-400_right_OOP'
cv2 = 8.83# center value
d2 = txtread(filename, cv2, 4)
d2 = txtread(filename, cv2, 1)

filename = 'S2/S2_-400_right_IP'
cv3 = 10.244
d3 = txtread(filename, cv3, 1)

filename = 'S2/S2_-400_down_IP'
cv4 = 8.195
d4 = txtread(filename, cv4, 2)
d4 = txtread(filename, cv4, 1)
```

```
######
snipl2 = 1
snipb2 = 3

######

s2N400 = np.array( [ d2[snipb2:,:-snipl2], d3[snipb2:,:-snipl2], d4
                                    [:-snipb2,snipl2:] ] )


# f4 = figfig()
# plt.title('N400 orientation')
# plt.pcolor(xx[:-snipb,:-snipl],yy[:-snipb,:-snipl], np.sum(N400,
                                    axis=0), rasterized=True)
# plt.savefig('S2after.pdf', format='pdf')
#######
#######
#######
# manual alignment of the two composites
sld = 1
sbd = 1
procP400 = s2P400[:,(sbd-1):-sbd,(sld-1):-sld] #im doing this by
                                    hand based on the correction shifts
#cut from the right side
cut=42
procP400=procP400[:,:,:-cut]
print(shape(procP400))
# print(procP400[:,0,0])

f4 = figfig()
plt.title('P400 orientation')
plt.pcolor(xx[(sbd-1):-(snipb1+sbd),(sld-1):-(snipl1+sld+cut)],yy[(
                                    sbd-1):-(snipb1+sbd),(sld-1):-(
                                    snipl1+sld+cut)], np.sum(procP400,
                                    axis=0))
plt.savefig('1P.png', format='png')

######
```

```
sld = 22
sbd = 2
procN400 = s2N400[:,(sbd-1):-sbd,(sld-1):-sld] #im doing this by
                                    hand based on the correction shifts
print(shape(procN400))

f5 = figfig()
plt.title('N400 orientation')
plt.pcolor(xx[(sbd-1):-(snipb2+sbd),(sld-1):-(snipl2+sld)],yy[(sbd-
                                    1):-(snipb2+sbd),(sld-1):-(snipl2+
                                    sld)], np.sum(procN400,axis=0))
plt.savefig('1N.png', format='png')

## set counts for histogram
count0 = 0
count70 = 0
count109 = 0
count180 = 0
## coordinates of the device
bound1=95
bound2=155

ilen = shape(procP400)[1]
jlen = shape(procP400)[2]
A = np.zeros([ilen,jlen])
for i in range(ilen):
for j in range(jlen):
temp = int(round(angle(procP400[:,i,j], procN400[:,i,j])))
A[i,j] = temp
if bound1<i<bound2:
temp=4
elif temp ==0:
count0 = count0+1
elif temp ==1:
count70 = count70+1
elif temp==2:
count109=count109+1
elif temp==3:
count180=count180+1
```

```
total = count0+count70+count109+count180
print('count0',count0/total)
print('count70',count70/total)
print('count109',count109/total)
print('count180',count180/total)

## create variables for propagating counts
c0_1 = count0/total
c71_1 = count70/total
c109_1 = count109/total
c180_1 = count180/total


figfig()
p = plt.pcolor(xx[:ilen,:jlen],yy[:ilen,:jlen], A, rasterized=True,
                                    cmap='plasma',alpha=1) # inplane
                                    left+bottom

# plt.axhline(xx[0,bound1])
# plt.axhline(xx[0,bound2])
plt.fill_between([np.amin(xx[:ilen,:jlen]),np.amax(xx[:ilen,:jlen])
                                    ],xx[0,bound1],xx[0,bound2],color='
                                    k')


# cb = plt.colorbar(p)
# cb.set_ticks([0,1,2,3])
# cb.set_ticklabels([r'0$\degree$',r'71$\degree$',r'109$\degree$',r
                                    '180$\degree$'])
# cb.set_label('Switching Event',rotation=270,labelpad=5)

file = '1switch'
plt.savefig(file + '.png', format='png')
plt.savefig(file + '.pdf', format='pdf')
```

Appendix D:

Processing of XAS and XMCD Data

Working with our collaborators Padraic Shafer and Alpha T. N'Diaye at the ALS at LBL, I have developed some python code to better handle the large amount of data from time at the synchrotron. Padraic and Alpha have Origin macros set up for dealing with data from their beamlines, but Origin is not particularly usable in real time, for large amounts of data (since very little of it is automated), or on a laptop (since you may not have origin because you plot everything in python, right?). This appendix is dedicated to the processing of XAS and XMLD/XMCD data, as well the extraction of $\mathbf{l} \bullet \mathbf{s}$ from XMCD data.

D.1 Reading XAS Data and Calculating Dichroism

The processing of XAS data is fairly straightforward- from a single dataset at the beamline, there will be something like 10 scans for each polarization (linear for XMLD, circular for XMCD). The data are taken progressively, so each successive scan needs to be binned in the opposite manner (e.g. the tool will measure with polarizations +*P*, -*P*, -*P*, +*P*, +*P*, etc.). The background used is just a linear fit, which is not really right but is good enough. We then take the mean of each bin, so we end up with, for instance, a mean *s* polarization and a mean *p* polarization. The difference in these is then the linear or circular dichroism.

Subroutine:

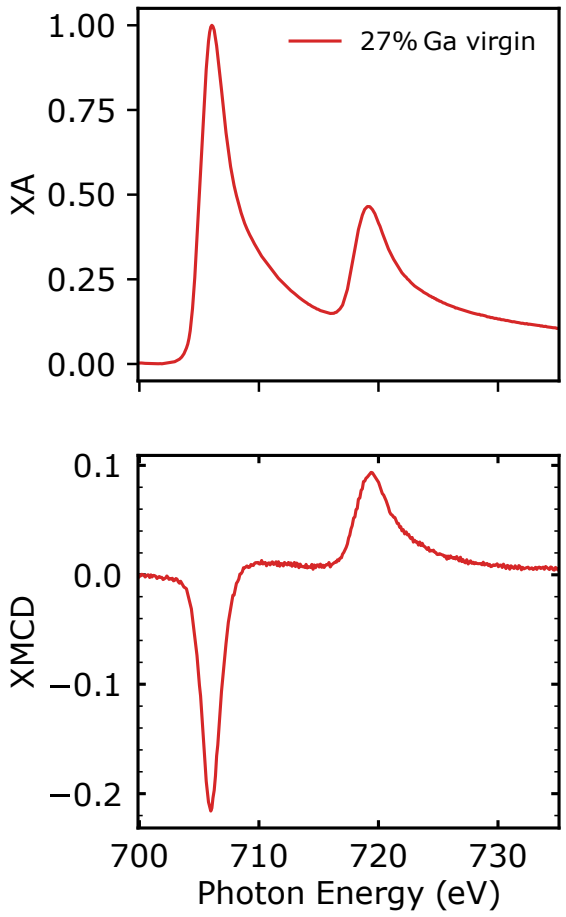

Figure D.1: Example XAS and XMCD. Example XAS and XMCD data about the Fe peak of a FeGa sample

```
#!/bin/python3
#
# file: xmld_data.py
# desc: Takes dat files from ALS XMLD and turns it into a
                                dictionary
# author: Peter Meisenheimer 190604
#

def ReadFile(filename):

  datafile = open(filename+'.txt', 'rb')
```

```
  while True:
    row = datafile.readline()
    if row.decode('utf-8').replace("\r\n", "") == "Description
                                  Length: 0":
      row = datafile.readline()
      break

  # Obtain labels

  labels = datafile.readline().decode('utf-8')
  labels = labels.replace("\n","").split("\t")

  indices = [i for i in range(0, len(labels))]
  data = {label: [] for label in labels}

  while True:
    row = datafile.readline()

  if not row:
    break
  else:
    values = row.decode('utf-8').replace("\r\n", "").split("\t")

    for l, i in zip(labels, indices):
      try:
        data[l].append(float(values[i]))
        except ValueError:
        data[l].append(values[i])

  return data
```

Preamble:

```
import numpy as np
import os
import csv
import matplotlib.pyplot as plt
from pylab import *
from matplotlib.ticker import AutoMinorLocator
```

```
import matplotlib.colors as mcol
import matplotlib.cm as cm
import scipy.interpolate as inter
import xmld_data as xld
```

Averaging:

```
def cat(data):

tim = data['Time (s)']

sI0ES = []
sEY = []
sC11 = []

pI0ES = []
pEY = []
pC11 = []

for i in range(len(tim)):
if tim[i] == tim[0]:
sI0ES.append(data['I0 ES'][i])
sEY.append(data['EY'][i])
sC11.append(data['Energy Readback'][i])

else:
pI0ES.append(data['I0 ES'][i])
pEY.append(data['EY'][i])
pC11.append(data['Energy Readback'][i])


spol = np.transpose( np.array([sC11,sI0ES,sEY]) )

ppol = np.transpose( np.array([pC11,pI0ES,pEY]) )

return(spol,ppol)

#######
```

```
def lyfirstnorm(data):
xx = np.array(range(len(data)))
lya = 65
lyb = 110
mean = (data[lyb]+data[lya])/2
mean = []
for i in range(lya,lyb):
mean.append(data[i])

mean = np.mean(mean)
datanew = data*(1/mean )
return(datanew)


#######

def pull(tag, shift, note):

  n = 1
  if note ==1:
    filename = 'trajscan_data/'+tag+'_0001'
    N = np.arange(n)+1
  elif note==2:
    filename = 'trajscan_data/'+tag+'_0009'
    N = np.arange(n)+9
  elif note==3:
    filename = 'trajscan_data/'+tag+'_0017'
    N = np.arange(n)+17

  data = xld.ReadFile(filename)

  a = data['Energy Readback'][0]+1
  b = data['Energy Readback'][-1]-1

  ll = int( (b-a)*1e3 )

  sC11 = np.zeros(( int( len(data['Time (s)'])/2) ,n))
  sEY = np.zeros(( int( len(data['Time (s)'])/2) ,n))
```

```
pC11 = np.zeros(( int( len(data['Time (s)'])/2) ,n))
pEY = np.zeros(( int( len(data['Time (s)'])/2) ,n))

### arange all data into matrices
for i in range(n):
  if N[i] <= 9:
    filename = 'trajscan_data/'+tag+'_000{}'.format(N[i])
  else:
    filename = 'trajscan_data/'+tag+'_00{}'.format(N[i])
  #          print(filename)
data = xld.ReadFile(filename)

XX = np.linspace(a,b,ll)

spol,ppol = cat(data)

sC11[:,i] = spol[:,0]
sEY[:,i] = lyfirstnorm(spol[:,2]/spol[:,1])

pC11[:,i] = ppol[:,0]
pEY[:,i] = lyfirstnorm(ppol[:,2]/ppol[:,1])


## take out the settling data, replace 1 with 3
#      sLY[:,0] = sLY[:,2]
#      pLY[:,0] = pLY[:,2]

C11out = sC11[:,-1]
#      spacer = 1
#      C11out = XX[spacer:-spacer]
### shift is in 10meV increments

### calculate differences
smean = np.mean(sEY,axis=1)
pmean = np.mean(pEY,axis=1)

#      x = C11out
#      y = smean
#      m, b = polyfit( (x[0],x[-1]), (y[0],y[-1]), 1)
```

```
    #       smean = y-(m*x+b)

    #       y = pmean
    #       m, b = polyfit( (x[0],x[-1]), (y[0],y[-1]), 1)
    #       pmean = y-(m*x+b)

    avgmean = (smean+pmean)/2
    smean = (smean-min(avgmean))/(max(avgmean-min(avgmean)) )
    pmean = (pmean-min(avgmean))/(max(avgmean-min(avgmean)) )

    EYdiff = (smean - pmean)

    ### background subtract
    #       m = (LYdiff[0]-LYdiff[-1])/(C11out[0]-C11out[-1])
    #       LYdiff = LYdiff-(C11out*m)
    #       LYdiff = LYdiff-LYdiff[0]

    x = C11out
    y = EYdiff
    m, b = polyfit( (x[0],x[-1]), (y[0],y[-1]), 1)

    EYdiff = y-(m*x+b)

    #       smean = smean+(m*x+b)/2
    #       pmean = pmean-(m*x+b)/2

    return(C11out, smean, pmean, EYdiff)
```

Plotting:

```
### figures
# %matplotlib inline
def compfig(tag, C11, pmean, smean, EYdiff):

  figuresize=[4,2.5]

  left = .2
  right = 0.95
  bottom = .17
```

```
top = 0.90

f = plt.figure(figsize=(figuresize[0],figuresize[1]), dpi=100,
                                facecolor='w', edgecolor='k')
f.subplots_adjust(left=left,right=right,bottom=bottom,top=top)
plt.rc('axes', linewidth=1)

ax = plt.subplot(111)
ll=1 # linewidth
ts=10 # title size

ax.plot(C11,smean, color='tab:blue',label=r'$0\degree$', lw=ll)
ax.plot(C11,pmean, color='tab:red',label=r'$90\degree$', lw=ll)

ax.set_xlabel(''r'Photon Energy (eV)', fontsize=ts, labelpad=2)
ax.set_ylabel('XMLD (a.u.)',fontsize=ts, labelpad=2)

ax.set_ylim([-0.05,1.1])
#ax.set_xticks(np.arange(20,71,10))
ax.set_xlim([min(C11)+10,max(C11)-10])


minor_locator = AutoMinorLocator(5)
ax.xaxis.set_minor_locator(minor_locator)
ax.yaxis.set_minor_locator(minor_locator)
ax.yaxis.set_ticks_position('both')
ax.xaxis.set_ticks_position('both')
plt.tick_params(axis='both', which='major', labelsize=ts, length=
                                2.5, width=1, pad = 5, direction='
                                in')
plt.tick_params(axis='both', which='minor', labelsize=ts, length=
                                1.5, width=.5, pad = 5, direction='
                                in')

leg = plt.legend(loc=1, fontsize=ts-2)
leg.get_frame().set_linewidth(0.0)
#     plt.show()
#os.chdir(os.path.expanduser('~/Desktop') )
plt.savefig('figures/'+tag+'comp.pdf', format='pdf')
```

```
######
def diffig(tag, C11, pmean, smean, EYdiff):

  figuresize=[4,2.5]

  left = .2
  right = 0.95
  bottom = .17
  top = 0.90

  f = plt.figure(figsize=(figuresize[0],figuresize[1]), dpi=100,
                                  facecolor='w', edgecolor='k')
  f.subplots_adjust(left=left,right=right,bottom=bottom,top=top)
  plt.rc('axes', linewidth=1)

  ax = plt.subplot(111)
  ll=1 # linewidth
  ts=10 # title size

  ax.axhline(0,color='k',linestyle='--', alpha=0.8, lw=0.5)

  ax.plot(C11,EYdiff*100, color='tab:blue', lw=ll)
  #     ax.plot(C11,pmean, color='tab:red', lw=ll)

  ax.set_xlabel(''r'Photon Energy (eV)', fontsize=ts, labelpad=2)
  ax.set_ylabel('Dichroism (%)',fontsize=ts, labelpad=2)

  #     ax.set_ylim([-0.05,1.1])
  #ax.set_xticks(np.arange(20,71,10))
  ax.set_xlim([min(C11)+10,max(C11)-10])


  minor_locator = AutoMinorLocator(5)
  ax.xaxis.set_minor_locator(minor_locator)
  ax.yaxis.set_minor_locator(minor_locator)
  ax.yaxis.set_ticks_position('both')
  ax.xaxis.set_ticks_position('both')
  plt.tick_params(axis='both', which='major', labelsize=ts, length=
```

```
                                    2.5, width=1, pad = 5, direction='
                                    in')
    plt.tick_params(axis='both', which='minor', labelsize=ts, length=
                                    1.5, width=.5, pad = 5, direction='
                                    in')

    #      plt.show()
    #os.chdir(os.path.expanduser('~/Desktop') )
    plt.savefig('figures/'+tag+'dif.pdf', format='pdf')

#######
def postfig(lis,lab,note):

    ######
    Per = range(len(lis))

    cm1 = mcol.LinearSegmentedColormap.from_list("MyCmapName",["tab:
                                    red","tab:blue"])
    cnorm = mcol.Normalize(vmin=min(Per),vmax=max(Per))

    cpick = cm.ScalarMappable(norm=cnorm,cmap=cm1)
    cpick.set_array([])

    #######

    figuresize=[2.5,5]

    left = .2
    right = 0.95
    bottom = .17
    top = 0.90

    # f = plt.figure(figsize=(figuresize[0],figuresize[1]), dpi=150,
                                    facecolor='w', edgecolor='k')
    # f.subplots_adjust(left=left,right=right,bottom=bottom,top=top)
    plt.rc('axes', linewidth=1)

    #      ax = plt.subplot(111)
    f, (ax1, ax2) = plt.subplots(2,1, sharex=True,figsize=(figuresize
```

```
                                [0],figuresize[1]), dpi=130,
                                facecolor='w', edgecolor='k')
f.subplots_adjust(left=left,right=right,bottom=bottom,top=top)
ll=1 # linewidth
ts=10 # title size
val = []

for i in range(len(Per)):
shift=0
tag = 'Trajscan{}'.format(lis[i])
C11, smean,pmean, EYdiff = pull(tag,shift,note[i])
val.append(max(abs(EYdiff)))
ax1.plot(C11,(pmean+smean)/2+0.2*i*0, color = cpick.to_rgba(Per[i
                                ]), lw=ll, label = lab[i])
ax2.plot(C11,EYdiff+0.02*i*0, color = cpick.to_rgba(Per[i]), lw=
                                ll)

ax1.set_ylabel('XA',fontsize=ts, labelpad=2)
ax2.set_xlabel(''r'Photon Energy (eV)', fontsize=ts, labelpad=2)
ax2.set_ylabel('XMCD',fontsize=ts, labelpad=2)

#     ax.set_ylim([-0.05,1.1])
#ax.set_xticks(np.arange(20,71,10))
ax2.set_xlim([min(C11)+10,max(C11)-10])


minor_locator = AutoMinorLocator(5)
ax2.xaxis.set_minor_locator(minor_locator)
ax2.yaxis.set_minor_locator(minor_locator)
ax2.yaxis.set_ticks_position('both')
ax2.xaxis.set_ticks_position('both')
plt.tick_params(axis='both', which='major', labelsize=ts, length=
                                2.5, width=1, pad = 5, direction='
                                in')
plt.tick_params(axis='both', which='minor', labelsize=ts, length=
                                1.5, width=.5, pad = 5, direction='
                                in')

leg = ax1.legend(loc=1, fontsize=ts-2)
```

```
    leg.get_frame().set_linewidth(0.0)

    plt.savefig('figures/'+tag+'post.pdf', format='pdf')
    print(val)

######

def singledata(lis,lab,note):
    shift=0
    i=0
    tag = 'Trajscan{}'.format(lis[i])
    C11, smean,pmean, LYdiff = pull(tag,shift,note[i])
    #      val.append(max(abs(LYdiff)))
    return(C11,(pmean+smean)/2)
```

How to call:

```
## TrajScan28565_0001
lis = [28565]
lab = ['27% Ga virgin']
note = [1]
shift=0
print('first try')

postfig(lis,lab,note)
```

D.2 MVH Loop from XMCD

Circular dichroism can be used to reconstruct a hysteresis loop by measuring the peak value and then evolving the field. Using the same preamble as above, this can be done:

```
def cat(data):

tim = data['Time (s)']

I0ES = []
```

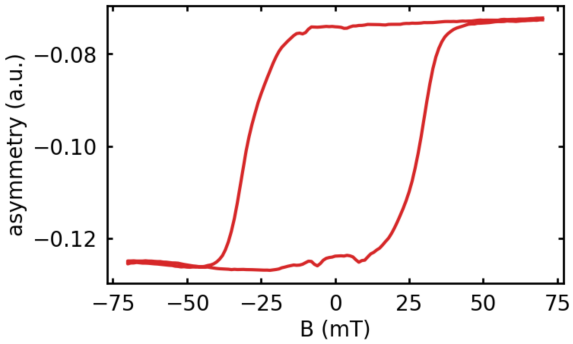

Figure D.2: Magnetic hysteresis from XMCD. Example hysteresis taken from XMCD data about the Fe peak of a FeGa sample

```
EY=[]
B=[]

for i in range(len(tim)):
I0ES.append(data['I0 ES'][i])
EY.append(data['EY'][i])
B.append(data['Magnet Field'][2*i])


dat = np.transpose( np.array([B,I0ES,EY]) )

return(dat)


#####

def pull(tag,npoints):

  n = 1
  filename = 'trajscan_data/'+tag
  data = cat(xld.ReadFile(filename))

  ratio = data[:,2]/data[:,1]

  #brute force the number of loops
  nscans = 12
  nloops = 2*nscans
  #     npoints = 282 # subject to change
```

```
  fields = data[0:npoints,0]
  print(len(fields))
  vals=[]

  for i in range(nloops):
    vals.append(ratio[i*npoints:(i+1)*npoints])
    vals = np.array(vals)
    print(shape(vals))

  L2=[]
  L3=[]
  for i in range(int(nscans/2)):
  L2.append(vals[4*i,:])
  L3.append(vals[4*i+1,:])
  L3.append(vals[4*i+2,:])
  L2.append(vals[4*i+3,:])
  L2=np.array(L2)
  L3=np.array(L3)

  asymm = (L3-L2)/(L2+L3)
  print(shape(asymm))
  meanasymm = np.mean(asymm,axis=0)

  return(fields, vals, meanasymm)
#####

#### figure parameters
def figfig():
  figuresize=[4,2.5]

  left = .2
  right = 0.95
  bottom = .17
  top = 0.90

  f = plt.figure(figsize=(figuresize[0],figuresize[1]), dpi=200,
                                  facecolor='w', edgecolor='k')
  f.subplots_adjust(left=left,right=right,bottom=bottom,top=top)
```

```
  plt.rc('axes', linewidth=1)

  ax = plt.subplot(111)
  ll=1 # linewidth
  ts=10 # title size

  # ax.axhline(0,color='k',linestyle='--', alpha=0.8, lw=0.5)


  ax.set_xlabel(''r'B (mT)', fontsize=ts, labelpad=2)
  ax.set_ylabel('asymmetry (a.u.)',fontsize=ts, labelpad=2)

  ax.yaxis.set_ticks_position('both')
  ax.xaxis.set_ticks_position('both')
  plt.tick_params(axis='both', which='major', labelsize=ts, length=
                                2.5, width=1, pad = 5, direction='
                                in')
  plt.tick_params(axis='both', which='minor', labelsize=ts, length=
                                1.5, width=.5, pad = 5, direction='
                                in')
####
```

```
figfig()

### 0V MVH
tag = ['TrajScan28566']

lab = ['0V']

######
Per = range(len(tag))

cm1 = mcol.LinearSegmentedColormap.from_list("MyCmapName",["tab:red
                                ","tab:blue"])
cnorm = mcol.Normalize(vmin=min(Per),vmax=max(Per))

cpick = cm.ScalarMappable(norm=cnorm,cmap=cm1)
cpick.set_array([])
```

```
#######

for i in range(len(tag)):

    fields,vals,asymm = pull(tag[i],282)
    plt.plot(fields*1000,asymm,color = cpick.to_rgba(Per[i]) ,label =
                                        lab[i])
```

D.3 Calculation of Spin-Orbit Coupling from XMCD

From XMCD data, both the spin and orbital components of the magnetization can be evaluated from the integrals of the two signals. This process is detailed especially well in [337] and so I will not go too far into detail here, but will provide a brief overview, as well as my own calculations.

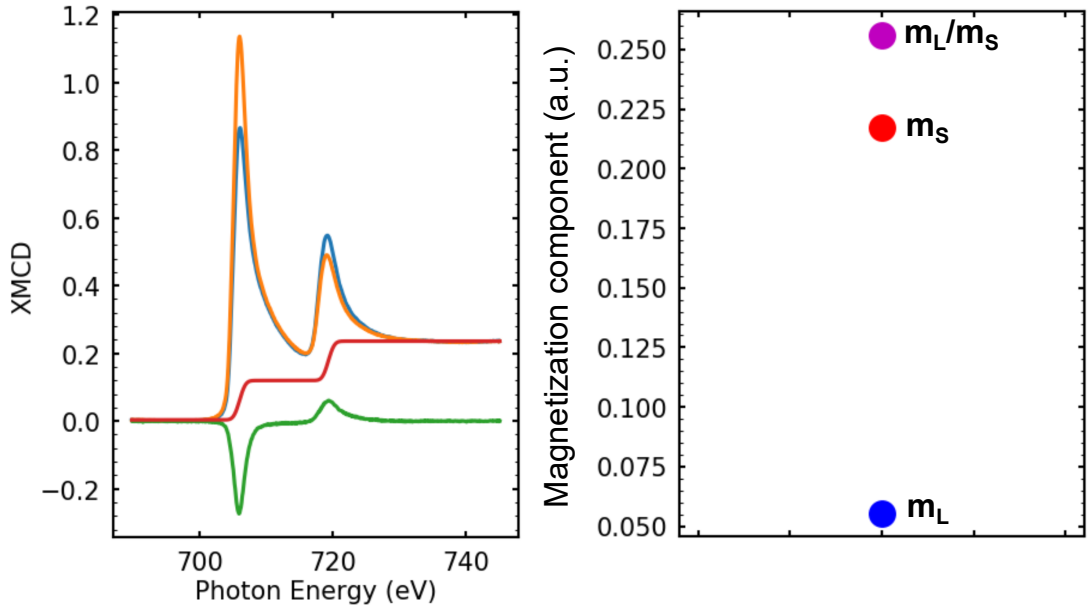

Figure D.3: Spin-orbit coupling from XMCD. Example XMCD about the Fe peak of a FeGa sample, used to calculate m_L/m_S via the sum rule. Both polarization components are shown along with dichroic signal and the subtracted background.

After calculating the mean of the XAS data as normal, subtract a two-step error-function-like background. These steps are at the absorption edge of the signal. The

integral of this background-subtracted function goes to the denominator in the final analysis, R. Now working with the dichroism data, P is the integral at only the L_3 edge and Q is the full integral. From here, the DOS needs to be known to calculate the actual values of m_L and m_S, but m_L/m_S can be expressed as a unitless ratio. The component of the orbital moment is:

$$m_L = \frac{-4Q * N_h}{6R} \tag{D.1}$$

the component of the spin moment is:

$$m_S = \frac{-(6P-4Q)N_h}{2R} \tag{D.2}$$

and the ratio between the two:

$$m_L/m_S = \frac{2Q}{9P-6Q} \tag{D.3}$$

where N_h is the number of holes in the d-band of the element. The total moment should then be $m_L + m_S$

```
def cat(data):

  tim = data['Time (s)']

  sI0ES = []
  sEY = []
  sC11 = []

  pI0ES = []
  pEY = []
  pC11 = []

  for i in range(len(tim)):
  if tim[i] == tim[0]:
  sI0ES.append(data['I0 ES'][i])
  sEY.append(data['EY'][i])
  sC11.append(data['Energy Readback'][i])
```

```
  else:
  pI0ES.append(data['I0 ES'][i])
  pEY.append(data['EY'][i])
  pC11.append(data['Energy Readback'][i])


  spol = np.transpose( np.array([sC11,sI0ES,sEY]) )

  ppol = np.transpose( np.array([pC11,pI0ES,pEY]) )

  return(spol,ppol)

#####

def lyfirstnorm(x,data):
  xx = np.array(range(len(data)))
  lya = 20
  lyb = 120
  lyc = 440
  ### linearize
  background = np.zeros(len(data))
  mp = int(len(x)/2)

  m, b = polyfit( (xx[lya:lyb]), (data[lya:lyb]), 1)
  background[:mp]= m*xx[:mp]


  m2, b2 = polyfit( (xx[lyc:]), (data[lyc:]), 1)
  background[mp:] = m2*xx[mp:] - m2*xx[mp] + background[mp-1]
  #     figure()
  #     plt.plot(background)

  #     for i in range(len(background)):
  #         if i>mp:
  #             background[i] = background[i]+
  #     a,b,c = polyfit( (x[lyc:]), (data[lyc:]), 2)
  #     data = data-(a*x**2+b*x)
```

```
    datanew=data - background
    return(datanew)



######

def pull(tag, shift, note):

    n=1
    filename = 'trajscan_data/'+tag+'_0001'
    N = np.arange(n)+1

    data = xld.ReadFile(filename)

    a = data['Energy Readback'][0]+1
    b = data['Energy Readback'][-1]-1

    ll = int( (b-a)*1e3 )

    sC11 = np.zeros(( int( len(data['Time (s)'])/2) ,n))
    sEY = np.zeros(( int( len(data['Time (s)'])/2) ,n))

    pC11 = np.zeros(( int( len(data['Time (s)'])/2) ,n))
    pEY = np.zeros(( int( len(data['Time (s)'])/2) ,n))

    ### arange all data into matrices
    for i in range(n):
      if N[i] <= 9:
        filename = 'trajscan_data/'+tag+'_000{}'.format(N[i])
      else:
        filename = 'trajscan_data/'+tag+'_00{}'.format(N[i])
      #          print(filename)
      data = xld.ReadFile(filename)

      XX = np.linspace(a,b,ll)

      spol,ppol = cat(data)
```

```
    sC11[:,i] = spol[:,0]
    temp = lyfirstnorm(spol[:,0],spol[:,2]/spol[:,1])
    temp = temp-temp[0]
    sEY[:,i] = temp

    pC11[:,i] = ppol[:,0]
    temp2 = lyfirstnorm(ppol[:,0],ppol[:,2]/ppol[:,1])
    temp2 = temp2-temp2[0]
    pEY[:,i] = temp2

    ## take out the settling data, replace 1 with 3
    #      sLY[:,0] = sLY[:,2]
    #      pLY[:,0] = pLY[:,2]

C11out = sC11[:,-1]
#      spacer = 1
#      C11out = XX[spacer:-spacer]
### shift is in 10meV increments

### calculate differences
smean = np.mean(sEY,axis=1)
#      smean = smean/smean[-1]
pmean = np.mean(pEY,axis=1)
## normalize curves
pmean = pmean/pmean[-1]*smean[-1]
#      pmean = pmean/pmean[-1]

avgmean = (smean+pmean)/2
smean = (smean-min(avgmean))/(max(avgmean-min(avgmean)) )
pmean = (pmean-min(avgmean))/(max(avgmean-min(avgmean)) )

EYdiff = (smean - pmean)

### background subtract
#      m = (LYdiff[0]-LYdiff[-1])/(C11out[0]-C11out[-1])
#      LYdiff = LYdiff-(C11out*m)
#      LYdiff = LYdiff-LYdiff[0]

x = C11out
```

```
    y = EYdiff
    m, b = polyfit( (x[0],x[-1]), (y[0],y[-1]), 1)

    EYdiff = y-(m*x+b)

    #      smean = smean+(m*x+b)/2
    #      pmean = pmean-(m*x+b)/2

    return(C11out, smean, pmean, EYdiff)

####
from scipy.special import erf
def integrals(x,a,b):

    ### XAS integral
    ## indeces of the edge peaks
    p1 = 172
    p2 = 302

    end = 366
    end = -1
    background = np.zeros(len(x))

    XAS = (a+b)/2
    XMCD = a-b
    start = 0

    offset = XAS[start]
    background = (background + offset +
    ( (XAS[end]-offset)/2*(erf(x-x[np.argmax(XMCD)])+1)/2 ) +
    ( (XAS[end]-offset)/2*(erf(x-x[np.argmax(XAS)])+1)/2 ) )


    XASnorm = XAS-background
    R = np.trapz(XASnorm[start:end],x[start:end])

    ### XMCD integral
    #      m, b = polyfit( (x[0],x[-1]), (XMCD[0],XMCD[-1]), 1)
    #      XMCD = XMCD-(m*x+b)
```

```
    Q = np.trapz(XMCD,x)

    ### L3 integral
    ## index of the start of the second peak
    val = np.min(XAS[np.argmax(XAS):np.argmax(XMCD)])
    l3stop = XAS.tolist().index(val)
    #     print(l3stop)

    xL3 = x[start:l3stop]
    L3 = XMCD[start:l3stop]
    P = np.trapz(L3,xL3)

    ML = -(4*Q)/(6*R)
    MS = -(6*P-4*Q)/(2*R)
    MLMS = (2*Q)/(9*P-6*Q)

    return(P,Q,R,ML,MS,MLMS, background)

####

def figfig():
    figuresize=[3,4]

    left = .2
    right = 0.95
    bottom = .17
    top = 0.90

    # f = plt.figure(figsize=(figuresize[0],figuresize[1]), dpi=150,
                                    facecolor='w', edgecolor='k')
    # f.subplots_adjust(left=left,right=right,bottom=bottom,top=top)
    plt.rc('axes', linewidth=1)

    #     ax = plt.subplot(111)
    f, ax = plt.subplots(1,1 ,figsize=(figuresize[0],figuresize[1]),
                                    dpi=150, facecolor='w', edgecolor='
                                    k')
```

```
    f.subplots_adjust(left=left,right=right,bottom=bottom,top=top)
    ll=1 # linewidth
    ts=10 # title size

    ax.set_xlabel(''r'Photon Energy (eV)', fontsize=ts, labelpad=2)
    ax.set_ylabel('XMCD',fontsize=ts, labelpad=2)

    minor_locator = AutoMinorLocator(5)
    ax.xaxis.set_minor_locator(minor_locator)
    ax.yaxis.set_minor_locator(minor_locator)
    ax.yaxis.set_ticks_position('both')
    ax.xaxis.set_ticks_position('both')
    plt.tick_params(axis='both', which='major', labelsize=ts, length=
                                    2.5, width=1, pad = 5, direction='
                                    in')
    plt.tick_params(axis='both', which='minor', labelsize=ts, length=
                                    1.5, width=.5, pad = 5, direction='
                                    in')
```

```
figfig()
lis = [28565,28569,28578,28585,28588,28590,28594,28597]
lab = [0,100,200,300,400,300,100,0]
lis = [28565]
lab = [0]
# lis = [28593,28594]
# lab = [200,100]
note = np.ones(len(lis))
shift=0

ML=[]
MS=[]
MLMS=[]

for i in range(len(lis)):

tag = 'Trajscan{}'.format(lis[i])
C11, smean,pmean, EYdiff = pull(tag,shift,note[i])
```

```
plt.plot(C11,smean)
plt.plot(C11, pmean)
plt.plot(C11, smean-pmean)

P,Q,R,tempML,tempMS,tempMLMS,b = integrals(C11, smean,pmean)
print(P,Q,R)
print(tempML,tempMS,tempMLMS)
plt.plot(C11,b)

ML.append(tempML)
MS.append(tempMS)
MLMS.append(tempMLMS)

figfig()
plt.plot(lab,ML,c='b',marker='o',ms=10)
plt.plot(lab,MS,c='r',marker='o',ms=10)
plt.plot(lab,MLMS,c='m',marker='o',ms=10)
print()

###################################


print('ML',mean(ML) )
print('MS',mean(MS) )
print('MLMS',mean(MLMS) )
```

References

[1] EIA projects nearly 50% increase in world energy usage by 2050, led by growth in Asia - Today in Energy - U.S. Energy Information Administration (EIA).

[2] Ramesh, R. & Spaldin, N. A. Multiferroics: progress and prospects in thin films. *Nature Materials* **6**, 21–29 (2007).

[3] Meisenheimer, P. B., Novakov, S., Vu, N. M. & Heron, J. T. Perspective: Magnetoelectric switching in thin film multiferroic heterostructures. *Journal of Applied Physics* **123**, 240901 (2018).

[4] Manipatruni, S. *et al.* Scalable energy-efficient magnetoelectric spin–orbit logic. *Nature* **565**, 35–42 (2019).

[5] Shevlin, S. Multiferroics and the path to the market. *Nature Materials* **18**, 191 (2019).

[6] Zhu, W. K. *et al.* Strong ferromagnetism induced by canted antiferromagnetic order in double perovskite iridates $(La_{1-x}Sr_x)_2ZnIrO_6$. *Physical Review B - Condensed Matter and Materials Physics* **91**, 1–8 (2015).

[7] Mundy, J. A. *et al.* Atomically engineered ferroic layers yield a room-temperature magnetoelectric multiferroic. *Nature* **537**, 523–527 (2016).

[8] Cai, J.-W., Wang, C., Shen, B.-G., Zhao, J.-G. & Zhan, W.-S. Colossal magnetoresistance of spin-glass perovskite $La_{0.67}Ca_{0.33}Mn_{0.9}Fe_{0.1}O_3$. *Applied Physics Letters* **71**, 1727–1729 (1997).

[9] Wang, R. F. *et al.* Artificial 'spin ice' in a geometrically frustrated lattice of nanoscale ferromagnetic islands. *Nature* **439**, 303–306 (2006).

[10] Ahn, C. H., Rabe, K. M. & Triscone, J.-M. Ferroelectricity at the Nanoscale: Local Polarization in Oxide Thin Films and Heterostructures. *Science* **303**, 488–491 (2004).

[11] Meisenheimer, P. B., Kratofil, T. J. & Heron, J. T. Giant Enhancement of Exchange Coupling in Entropy-Stabilized Oxide Heterostructures. *Scientific Reports* **7**, 13344 (2017).

[12] Meisenheimer, P. B. *et al.* Magnetic frustration control through tunable stereochemically driven disorder in entropy-stabilized oxides. *Physical Review Materials* **3**, 104420 (2019).

[13] Sivakumar, S., Zwier, E., Meisenheimer, P. B. & Heron, J. T. Bulk and Thin Film Synthesis of Compositionally Variant Entropy-stabilized Oxides. *JoVE (Journal of Visualized Experiments)* e57746–e57746 (2018).

[14] Meisenheimer, P. B. *et al.* Engineering new limits to magnetostriction through metastability in iron-gallium alloys. *Nature Communications* **Under Review**.

[15] Rost, C. M. *et al.* Entropy-stabilized oxides. *Nature Communications* **6**, 8485 (2015).

[16] Berardan, D., Franger, S., Dragoe, D., Meena, A. K. & Dragoe, N. Colossal dielectric constant in high entropy oxides. *Physica Status Solidi - Rapid Research Letters* **10**, 328–333 (2016).

[17] Berardan, D., Franger, S., Meena, A. K. & Dragoe, N. Room temperature lithium superionic conductivity in high entropy oxides. *J. Mater. Chem. A* 9536–9541 (2016).

[18] Wang, J. *et al.* Epitaxial $BiFeO_3$ multiferroic thin film heterostructures. *Science* **299**, 1719–1722 (2003).

[19] Choi, T. *et al.* Insulating interlocked ferroelectric and structural antiphase domain walls in multiferroic $YMnO_3$. *Nature Materials* **9**, 253 (2010).

[20] Carpenter, M. A., Salje, E. K. H. & Howard, C. J. Magnetoelastic coupling and multiferroic ferroelastic/magnetic phase transitions in the perovskite $KMnF_3$. *Physical Review B* **85**, 224430 (2012).

[21] Vaz, C. A. F. *et al.* Origin of the Magnetoelectric Coupling Effect in $PbZr_{0.2}Ti_{0.8}O_3$/$La_{0.8}Sr_{0.2}MnO_3$ Multiferroic Heterostructures. *Physical Review Letters* **104**, 127202 (2010).

[22] Balke, N. *et al.* Deterministic control of ferroelastic switching in multiferroic materials. *Nature nanotechnology* **4**, 868–875 (2009).

[23] Butykai, d. *et al.* Characteristics of ferroelectric-ferroelastic domains in Néel-type skyrmion host GaV_4S_8. *Scientific Reports* **7**, 44663 (2017).

[24] Zimmermann, A. S., Meier, D. & Fiebig, M. Ferroic nature of magnetic toroidal order. *Nature Communications* **5**, 4796 (2014).

[25] Van Aken, B. B., Rivera, J.-P., Schmid, H. & Fiebig, M. Observation of ferrotoroidic domains. *Nature* **449**, 702–705 (2007).

[26] Spaldin, N. A., Fiebig, M. & Mostovoy, M. The toroidal moment in condensed-matter physics and its relation to the magnetoelectric effect. *Journal of Physics: Condensed Matter* **20**, 434203 (2008).

[27] Eerenstein, W., Mathur, N. D. & Scott, J. F. Multiferroic and magnetoelectric materials. *Nature* **442**, 759 (2006).

[28] Wang, Y., Hu, J., Lin, Y. & Nan, C.-W. Multiferroic magnetoelectric composite nanostructures. *NPG Asia Materials* **2**, 61–68 (2010).

[29] Nan, C.-W., Bichurin, M. I., Dong, S., Viehland, D. & Srinivasan, G. Multiferroic magnetoelectric composites: Historical perspective, status, and future directions. *Journal of Applied Physics* **103**, 031101 (2008).

[30] Ma, J., Hu, J., Li, Z. & Nan, C.-W. Recent Progress in Multiferroic Magnetoelectric Composites: from Bulk to Thin Films. *Advanced Materials* **23**, 1062–1087 (2011).

[31] Hu, J.-M., Chen, L.-Q. & Nan, C.-W. Multiferroic Heterostructures Integrating Ferroelectric and Magnetic Materials. *Advanced Materials* **28**, 15–39 (2016).

[32] Ascher, E., Rieder, H., Schmid, H. & Stössel, H. Some Properties of Ferromagnetoelectric Nickel-Iodine Boracite, $Ni_3B_7O_{13}I$. *Journal of Applied Physics* **37**, 1404–1405 (1966).

[33] Spaldin, N. A. Multiferroics: from the cosmically large to the subatomically small (2017).

[34] Juraschek, D. M., Fechner, M., Balatsky, A. V. & Spaldin, N. A. Dynamical multiferroicity. *Physical Review Materials* **1**, 014401 (2017).

[35] Khomskii, D. Classifying multiferroics: Mechanisms and effects. *Physics* **2**, 20 (2009).

[36] Cheong, S.-W. & Mostovoy, M. Multiferroics: a magnetic twist for ferroelectricity. *Nature Materials* **6**, 13–20 (2007).

[37] Martin, L. W., Chu, Y. H. & Ramesh, R. Advances in the growth and characterization of magnetic, ferroelectric, and multiferroic oxide thin films. *Materials Science and Engineering: R: Reports* **68**, 89–133 (2010).

[38] Evans, D. M. *et al.* Magnetic switching of ferroelectric domains at room temperature in multiferroic PZTFT. *Nature Communications* **4**, 1534 (2013).

[39] Keeney, L. *et al.* Magnetic Field-Induced Ferroelectric Switching in Multiferroic Aurivillius Phase Thin Films at Room Temperature. *Journal of the American Ceramic Society* **96**, 2339–2357 (2013).

[40] Borisov, P., Hochstrat, A., Chen, X., Kleemann, W. & Binek, C. Magnetoelectric Switching of Exchange Bias. *Physical Review Letters* **94**, 117203 (2005).

[41] Heron, J. T. *et al.* Deterministic switching of ferromagnetism at room temperature using an electric field. *Nature* **516**, 370–373 (2014).

[42] Huang, L., Wen, D., Zhong, Z., Zhang, H. & Bai, F. Magnetoelectric surface acoustic wave resonator with ultrahigh magnetic field sensitivity. *arXiv:1405.4076 [cond-mat]* (2014).

[43] Nan, T. *et al.* Acoustically actuated ultra-compact NEMS magnetoelectric antennas. *Nature Communications* **8**, 296 (2017).

[44] Emam, S., Sun, N.-X. & Nasrollahpour, M. P3-226: electrochemical gas sensor arrays for detecting volatile organic compound biomarkers in the exhaled breath. *Alzheimer's & Dementia* **15**, P1018–P1018 (2019).

[45] Bibes, M. & Barthélémy, A. Multiferroics: Towards a magnetoelectric memory. *Nature Materials* **7**, 425–426 (2008).

[46] Kani, N., Heron, J. T. & Naeemi, A. Strain-Mediated Magnetization Reversal Through Spin-Transfer Torque. *IEEE Transactions on Magnetics* **PP**, 1–1 (2017).

[47] Lu, C., Wu, M., Lin, L. & Liu, J.-M. Single-phase multiferroics: new materials, phenomena, and physics. *National Science Review* **6**, 653–668 (2019).

[48] Sanchez, D. A., Kumar, A., Ortega, N., Katiyar, R. S. & Scott, J. F. Near-room temperature relaxor multiferroic. *Applied Physics Letters* **97**, 202910 (2010).

[49] Pitcher, M. J. *et al.* Tilt engineering of spontaneous polarization and magnetization above 300 K in a bulk layered perovskite. *Science* **347**, 420–424 (2015).

[50] Mandal, P. *et al.* Designing switchable polarization and magnetization at room temperature in an oxide. *Nature* **525**, 363–366 (2015).

[51] Ahmad, H., Atulasimha, J. & Bandyopadhyay, S. Reversible strain-induced magnetization switching in FeGa nanomagnets: Pathway to a rewritable, non-volatile, non-toggle, extremely low energy straintronic memory. *Scientific Reports* **5**, srep18264 (2015).

[52] Scott, J. F. Room-temperature multiferroic magnetoelectrics. *NPG Asia Materials* **5**, e72 (2013).

[53] Hill, N. A. Why Are There so Few Magnetic Ferroelectrics? *The Journal of Physical Chemistry B* **104**, 6694–6709 (2000).

[54] Fiebig, M., Lottermoser, T., Meier, D. & Trassin, M. The evolution of multiferroics. *Nature Reviews Materials* 16046 (2016).

[55] Bibes, M., Villegas, J. E. & Barthélémy, A. Ultrathin oxide films and interfaces for electronics and spintronics. *Advances in Physics* **60**, 5–84 (2011).

[56] Zhou, J. *et al.* Directed assembly of nano-scale phase variants in highly strained $BiFeO_3$ thin films. *Journal of Applied Physics* **112**, 064102 (2012).

[57] Hu, J.-M., Duan, C.-G., Nan, C.-W. & Chen, L.-Q. Understanding and designing magnetoelectric heterostructures guided by computation: progresses, remaining questions, and perspectives. *npj Computational Materials* **3**, 18 (2017).

[58] Biegalski, M. D. *et al.* Relaxor ferroelectricity in strained epitaxial $SrTiO_3$ thin films on $DyScO_3$ substrates. *Applied Physics Letters* **88**, 192907 (2006).

[59] Choi, K. J. *et al.* Enhancement of Ferroelectricity in Strained $BaTiO_3$ Thin Films. *Science* **306**, 1005–1009 (2004).

[60] Schlom, D. G., Chen, L.-Q., Pan, X., Schmehl, A. & Zurbuchen, M. A. A Thin Film Approach to Engineering Functionality into Oxides. *Journal of the American Ceramic Society* **91**, 2429–2454 (2008).

[61] Sullivan, M. C. *et al.* Complex oxide growth using simultaneous in situ reflection high-energy electron diffraction and x-ray reflectivity: When is one layer complete? *Applied Physics Letters* **106**, 031604 (2015).

[62] Lee, W. *et al.* Atomic Layer Deposition of $SrTiO_3$ Films with Cyclopentadienyl-Based Precursors for Metal–Insulator–Metal Capacitors. *Chemistry of Materials* **25**, 953–961 (2013).

[63] Koster, G., Rijnders, G. J. H. M., Blank, D. H. A. & Rogalla, H. In Situ Initial Growth Studies of $SrTiO_3$ on $SrTiO_3$ by Time Resolved High Pressure RHEED. *MRS Online Proceedings Library (OPL)* **526** (1998).

[64] Hafez, M. A. & Elsayed-Ali, H. E. Activation energy of surface diffusion and terrace width dynamics during the growth of In(4×3) on Si(100)-(2×1) by femtosecond pulsed laser deposition. *Journal of Applied Physics* **103**, 093510 (2008).

[65] Liu, M. *et al.* Electrically induced enormous magnetic anisotropy in Terfenol-D/lead zinc niobate-lead titanate multiferroic heterostructures. *Journal of Applied Physics* **112**, 063917 (2012).

[66] Lahtinen, T. H. E., Franke, K. J. A. & Dijken, S. v. Electric-field control of magnetic domain wall motion and local magnetization reversal. *Scientific Reports* **2**, 258 (2012).

[67] Franke, K. J. A., López González, D., Hämäläinen, S. J. & van Dijken, S. Size Dependence of Domain Pattern Transfer in Multiferroic Heterostructures. *Physical Review Letters* **112**, 017201 (2014).

[68] Buzzi, M. *et al.* Single Domain Spin Manipulation by Electric Fields in Strain Coupled Artificial Multiferroic Nanostructures. *Physical Review Letters* **111**, 027204 (2013).

[69] Lou, J., Liu, M., Reed, D., Ren, Y. & Sun, N. X. Giant Electric Field Tuning of Magnetism in Novel Multiferroic FeGaB/Lead Zinc Niobate–Lead Titanate (PZN-PT) Heterostructures. *Advanced Materials* **21**, 4711–4715 (2009).

[70] Callen, E. R. & Callen, H. B. Static Magnetoelastic Coupling in Cubic Crystals. *Physical Review* **129**, 578–593 (1963).

[71] Newnham, R. E. *Properties of Materials: Anisotropy, Symmetry, Structure*.

[72] Wu, R. Origin of large magnetostriction in FeGa alloys. *Journal of Applied Physics* **91**, 7358–7360 (2002).

[73] Du, Y. *et al.* Relation between Ga ordering and magnetostriction of Fe-Ga alloys studied by x-ray diffuse scattering. *Physical Review B* **81**, 054432 (2010).

[74] Wang, H. *et al.* Understanding strong magnetostriction in $Fe_{100-x}Ga_x$ alloys. *Scientific Reports* **3**, 1–5 (2013).

[75] Furthmuller, J., Fahnle, M. & Herzer, G. Theory of magnetostriction in amorphous and polycrystalline ferromagnets. *Journal of Physics F: Metal Physics* **16**, L255–L258 (1986).

[76] Wang, Q. *et al.* Strain-mediated 180° switching in CoFeB and Terfenol-D nanodots with perpendicular magnetic anisotropy. *Applied Physics Letters* **110**, 102903 (2017).

[77] Parkes, D. E. *et al.* Non-volatile voltage control of magnetization and magnetic domain walls in magnetostrictive epitaxial thin films. *Applied Physics Letters* **101**, 072402 (2012).

[78] Lee, Y. *et al.* Large resistivity modulation in mixed-phase metallic systems. *Nature Communications* **6**, ncomms6959 (2015).

[79] Zhang, S. *et al.* Giant electrical modulation of magnetization in $Co_{40}Fe_{40}B_{20}/Pb(Mg_{1/3}Nb_{2/3})_{0.7}Ti_{0.3}O_3$ (011) heterostructure. *Scientific Reports* **4**, 3727 (2014).

[80] Feng, M. *et al.* Optimizing direct magnetoelectric coupling in $Pb(Zr,Ti)O_3$/Ni multiferroic film heterostructures. *Applied Physics Letters* **106**, 072901 (2015).

[81] Kim, J.-Y., Yao, L. & Dijken, S. v. Coherent piezoelectric strain transfer to thick epitaxial ferromagnetic films with large lattice mismatch. *Journal of Physics: Condensed Matter* **25**, 082205 (2013).

[82] Franke, K. J. *et al.* Reversible Electric-Field-Driven Magnetic Domain-Wall Motion. *Physical Review X* **5**, 011010 (2015).

[83] Nikonov, D. E. & Young, I. A. Benchmarking spintronic logic devices based on magnetoelectric oxides. *Journal of Materials Research* **29**, 2109–2115 (2014).

[84] Nikonov, D. E. & Young, I. A. Benchmarking of Beyond-CMOS Exploratory Devices for Logic Integrated Circuits. *IEEE Journal on Exploratory Solid-State Computational Devices and Circuits* **1**, 3–11 (2015).

[85] Ma, J., Shi, Z. & Nan, C.-W. Magnetoelectric Properties of Composites of Single $Pb(Zr,Ti)O_3$ Rods and Terfenol-D/Epoxy with a Single-Period of 1-3-Type Structure. *Advanced Materials* **19**, 2571–2573 (2007).

[86] Nan, C.-W., Liu, G. & Lin, Y. Influence of interfacial bonding on giant magnetoelectric response of multiferroic laminated composites of $Tb_{1-x}Dy_xFe_2$ and $PbZr_xTi_{1-x}O_3$. *Applied Physics Letters* **83**, 4366–4368 (2003).

[87] Zhang, S. *et al.* Electric-Field Control of Nonvolatile Magnetization in $Co_{40}Fe_{40}B_{20}/Pb(Mg_{1/3}Nb_{2/3})_{0.7}Ti_{0.3}O_3$ Structure at Room Temperature. *Physical Review Letters* **108**, 137203 (2012).

[88] Wu, T. *et al.* Electric-poling-induced magnetic anisotropy and electric-field-induced magnetization reorientation in magnetoelectric Ni/(011) $[Pb(Mg_{1/3}Nb_{2/3})O_3]_{1-x}$-$[PbTiO_3]_x$ heterostructure. *Journal of Applied Physics* **109**, 07D732 (2011).

[89] Mardana, A., Ducharme, S. & Adenwalla, S. Ferroelectric Control of Magnetic Anisotropy. *Nano Letters* **11**, 3862–3867 (2011).

[90] Ghidini, M. *et al.* Non-volatile electrically-driven repeatable magnetization reversal with no applied magnetic field. *Nature Communications* **4**, 1453 (2013).

[91] Gradauskaite, E., Meisenheimer, P., Müller, M., Heron, J. & Trassin, M. Multiferroic heterostructures for spintronics. *Physical Sciences Reviews* (2020).

[92] Jahjah, W. *et al.* Electrical Manipulation of Magnetic Anisotropy in a Electrical Manipulation of Magnetic Anisotropy in a $Fe_{81}Ga_{19}$/PMN-PT Magnetoelectric Multiferroic Composite. *Physical Review Applied* **13**, 034015 (2020).

[93] Wang, J. J. *et al.* Full 180° Magnetization Reversal with Electric Fields. *Scientific Reports* **4**, 7507 (2014).

[94] Hu, J.-M. *et al.* Purely Electric-Field-Driven Perpendicular Magnetization Reversal. *Nano Letters* **15**, 616–622 (2015).

[95] Imamura, H., Nozaki, T., Yuasa, S. & Suzuki, Y. Deterministic Magnetization Switching by Voltage Control of Magnetic Anisotropy and Dzyaloshinskii-Moriya Interaction under an In-Plane Magnetic Field. *Physical Review Applied* **10**, 054039 (2018).

[96] Nan, T. *et al.* A Strain-Mediated Magnetoelectric-Spin-Torque Hybrid Structure. *Advanced Functional Materials* **29**, 1806371 (2019).

[97] Lou, J. *et al.* Soft magnetism, magnetostriction, and microwave properties of FeGaB thin films. *Applied Physics Letters* **91**, 182504 (2007).

[98] Nakayama, H. *et al.* Mechanism of strong enhancement of anomalous Nernst effect in Fe by Ga substitution. *Physical Review Materials* **3**, 114412 (2019).

[99] Sakai, A. *et al.* Iron-based binary ferromagnets for transverse thermoelectric conversion. *Nature* **581**, 53–57 (2020).

[100] Yeh, J. W. *et al.* Nanostructured high-entropy alloys with multiple principal elements: Novel alloy design concepts and outcomes. *Advanced Engineering Materials* **6**, 299–303+274 (2004).

[101] Miracle, D. B. High-Entropy Alloys: A Current Evaluation of Founding Ideas and Core Effects and Exploring “Nonlinear Alloys”. *JOM* 1–7 (2017).

[102] Tsai, M.-H. & Yeh, J.-W. High-Entropy Alloys: A Critical Review. *Materials Research Letters* **2**, 107–123 (2014).

[103] Tsai, M.-H. Physical Properties of High Entropy Alloys. *Entropy* **15**, 5338–5345 (2013).

[104] Otto, F., Yang, Y., Bei, H. & George, E. P. Relative effects of enthalpy and entropy on the phase stability of equiatomic high-entropy alloys. *Acta Materialia* **61**, 2628–2638 (2013).

[105] Gao, M. C. *et al.* Design of Refractory High-Entropy Alloys. *Jom* **67**, 2653–2669 (2015).

[106] Wang, Y. P., Li, B. S. & Fu, H. Z. Solid Solution or Intermetallics in a High-Entropy Alloy. *Advanced Engineering Materials* **11**, 641–644 (2009).

[107] Ji, X. Relative effect of electronegativity on formation of high entropy alloys. *International Journal of Cast Metals Research* **28**, 229–233 (2015).

[108] Rost, C. *Entropy-Stabilized Oxides: Explorations of a Novel Class of Multicomponent Materials*. Ph.D. thesis, North Carolina State University (2016).

[109] Gludovatz, B. *et al.* A fracture-resistant high-entropy alloy for cryogenic applications. *Science* **345**, 1153–1158 (2014).

[110] Kotsonis, G. N., Rost, C. M., Harris, D. T. & Maria, J.-P. Epitaxial entropy-stabilized oxides: growth of chemically diverse phases via kinetic bombardment. *MRS Communications* **8**, 1371–1377 (2018).

[111] Sarkar, A. *et al.* Nanocrystalline multicomponent entropy stabilised transition metal oxides. *Journal of the European Ceramic Society* **37**, 747–754 (2017).

[112] Liu, D. *et al.* Ultrafast synthesis of entropy-stabilized oxide at room temperature. *Journal of the European Ceramic Society* **40**, 2504–2508 (2020).

[113] Lufaso, M. W. & Woodward, P. M. Jahn–Teller distortions, cation ordering and octahedral tilting in perovskites. *Acta Crystallographica Section B: Structural Science* **60**, 10–20 (2004).

[114] Ding, J. F. *et al.* Interfacial spin glass state and exchange bias in manganite bilayers with competing magnetic orders. *Physical Review B* **87**, 054428 (2013).

[115] Kotsonis, G. N. *et al.* Property and cation valence engineering in entropy-stabilized oxide thin films. *Physical Review Materials* **4**, 100401 (2020).

[116] Jimenez-Segura, M. P. *et al.* Long-range magnetic ordering in rocksalt-type high-entropy oxides. *Applied Physics Letters* **114**, 122401 (2019).

[117] Zhang, J. *et al.* Long-Range Antiferromagnetic Order in a Rocksalt High Entropy Oxide. *Chemistry of Materials* **31**, 3705–3711 (2019).

[118] Weisheit, M. *et al.* Electric Field-Induced Modification of Magnetism in Thin-Film Ferromagnets. *Science* **315**, 349–351 (2007).

[119] Nan, T., Hui, Y., Rinaldi, M. & Sun, N. X. Self-Biased 215MHz Magnetoelectric NEMS Resonator for Ultra-Sensitive DC Magnetic Field Detection. *Scientific Reports* **3**, 1985 (2013).

[120] Van Aken, B. B., Palstra, T. T. M., Filippetti, A. & Spaldin, N. A. The origin of ferroelectricity in magnetoelectric $YMnO_3$. *Nature Materials* **3**, 164–170 (2004).

[121] Dong, S., Zhai, J., Li, J.-F., Viehland, D. & Summers, E. Strong magnetoelectric charge coupling in stress-biased multilayer-piezoelectric/magnetostrictive composites. *Journal of Applied Physics* **101**, 124102 (2007).

[122] Clark, A. E. *et al.* Temperature dependence of the magnetic anisotropy and magnetostriction of $Fe_{100-x}Ga_x$ (x=8.6, 16.6, 28.5). *Journal of Applied Physics* **97**, 10M316 (2005).

[123] Clark, A. E. *et al.* Extraordinary magnetoelasticity and lattice softening in bcc Fe-Ga alloys. *Journal of Applied Physics* **93**, 8621–8623 (2003).

[124] Song, Y., Liu, P., Zhao, X., Guo, B. & Cui, X. Dielectric properties of $(Bi_{0.5}Nb_{0.5})_xTi_{1-x}O_2$ ceramics with colossal permittivity. *Journal of Alloys and Compounds* **722**, 676–682 (2017).

[125] O'Handley, R. C. *Modern magnetic materials: principles and applications*.

[126] Sander, D. The correlation between mechanical stress and magnetic anisotropy in ultrathin films. *Reports on Progress in Physics* **62**, 809–858 (1999).

[127] Rafique, S., Cullen, J. R., Wuttig, M. & Cui, J. Magnetic anisotropy of FeGa alloys. *Journal of Applied Physics* **95**, 6939–6941 (2004).

[128] Hu, J.-M., Li, Z., Wang, J. & Nan, C. W. Electric-field control of strain-mediated magnetoelectric random access memory. *Journal of Applied Physics* **107**, 093912 (2010).

[129] Yang, L. *et al.* Bipolar loop-like non-volatile strain in the (001)-oriented $Pb(Mg_{1/3}Nb_{2/3})O_3$-$PbTiO_3$ single crystals. *Scientific Reports* **4**, 4591 (2014).

[130] Guo, X. *et al.* Electrical field control of non-volatile 90° magnetization switching in epitaxial FeSi films on (001) 0.7[$Pb(Mg_{1/3}Nb_{2/3})O_3$]-0.3[$PbTiO_3$]. *Applied Physics Letters* **108**, 042403 (2016).

[131] Noheda, B., Cox, D. E., Shirane, G., Gao, J. & Ye, Z.-G. Phase diagram of the ferroelectric relaxor (1-x)$PbMg_{1/3}Nb_{2/3}O_3$-x$PbTiO_3$. *Physical Review B* **66**, 054104 (2002).

[132] Ghidini, M. *et al.* Shear-strain-mediated magnetoelectric effects revealed by imaging. *Nature Materials* 1 (2019).

[133] Petculescu, G., Hathaway, K. B., Lograsso, T. A., Wun-Fogle, M. & Clark, A. E. Magnetic field dependence of galfenol elastic properties. *Journal of Applied Physics* **97**, 10M315 (2005).

[134] Datta, S., Atulasimha, J., Mudivarthi, C. & Flatau, A. B. Stress and magnetic field-dependent Young's modulus in single crystal iron–gallium alloys. *Journal of Magnetism and Magnetic Materials* **322**, 2135–2144 (2010).

[135] Barturen, M. *et al.* Bulklike behavior of magnetoelasticity in epitaxial $Fe_{1-x}Ga_x$ thin films. *Physical Review B* **99**, 134432 (2019).

[136] Grössinger, R., Turtelli, R. S. & Mehmood, N. Materials with high magnetostriction. *IOP Conference Series: Materials Science and Engineering* **60**, 012002 (2014).

[137] Srinivasan, G. *et al.* Magnetoelectric bilayer and multilayer structures of magnetostrictive and piezoelectric oxides. *Physical Review B* **64**, 214408 (2001).

[138] Lo, C., Ring, A., Snyder, J. & Jiles, D. Improvement of magnetomechanical properties of cobalt ferrite by magnetic annealing. *IEEE Transactions on Magnetics* **41**, 3676–3678 (2005).

[139] Wang, D., Nordman, C., Qian, Z., Daughton, J. M. & Myers, J. Magnetostriction effect of amorphous CoFeB thin films and application in spin-dependent tunnel junctions. *Journal of Applied Physics* **97**, 10C906 (2005).

[140] Özkale, B., Shamsudhin, N., Bugmann, T., Nelson, B. J. & Pané, S. Magnetostriction in electroplated CoFe alloys. *Electrochemistry Communications* **76**, 15–19 (2017).

[141] Muth, P. & Wohlfarth, E. P. *Ferromagnetic Materials, Volume 1*, vol. 16.

[142] Samata, H., Fujiwara, N., Nagata, Y., Uchida, T. & Der Lan, M. Magnetic anisotropy and magnetostriction of SmFe2 crystal. *Journal of Magnetism and Magnetic Materials* **195**, 376–383 (1999).

[143] Summers, E. M., Lograsso, T. A. & Wun-Fogle, M. Magnetostriction of binary and ternary Fe–Ga alloys. *Journal of Materials Science* **42**, 9582–9594 (2007).

[144] Wang, Y. *et al.* Fragile morphotropic phase boundary and phase stability in the near-surface region of the relaxor ferroelectric (1-x)PbZn$_{1/3}$Nb$_{2/3}$O$_3$ - xPbTiO$_3$: [001] field-cooled phase diagrams. *Physical Review B* **94**, 174103 (2016).

[145] Cross, L. E. Relaxor ferroelectrics. *Ferroelectrics* **76**, 241–267 (1987).

[146] Pogrebnjak, A. D. *et al.* The effect of the deposition parameters of nitrides of high-entropy alloys (TiZrHfVNb)N on their structure, composition, mechanical and tribological properties. *Journal of Superhard Materials* **35**, 356–368 (2013).

[147] Meng, F. & Baker, I. Nitriding of a high entropy FeNiMnAlCr alloy. *Journal of Alloys and Compounds* **645**, 376–381 (2015).

[148] Pogrebnjak, A. D., Bagdasaryan, A. A., Yakushchenko, I. V. & Beresnev, V. M. The structure and properties of high-entropy alloys and nitride coatings based on them. *Russian Chemical Reviews* **83**, 1027 (2014).

[149] Musicó, B. L. *et al.* The emergent field of high entropy oxides: Design, prospects, challenges, and opportunities for tailoring material properties. *APL Materials* **8**, 040912 (2020).

[150] Lokcu, E., Ozden, R. C. & Anik, M. Effect of Co Content on the Electrochemical Properties of (MgCoNiZnLi)O Based High Entropy Oxides for Li-Ion Batteries. *The Eurasia Proceedings of Science Technology Engineering and Mathematics* **11**, 29–32 (2020).

[151] Zhou, S. *et al.* Microstructure and dielectric properties of high entropy Ba(Zr$_{0.2}$Ti$_{0.2}$Sn$_{0.2}$Hf$_{0.2}$Me$_{0.2}$)O$_3$ perovskite oxides. *Ceramics International* **46**, 7430–7437 (2020).

[152] Zhao, Z. *et al.* High-entropy $(Y_{0.2}Nd_{0.2}Sm_{0.2}Eu_{0.2}Er_{0.2})AlO_3$: A promising thermal/environmental barrier material for oxide/oxide composites. *Journal of Materials Science & Technology* **47**, 45–51 (2020).

[153] Chen, H. *et al.* High entropy $(Y_{0.2}Yb_{0.2}Lu_{0.2}Eu_{0.2}Er_{0.2})_3Al_5O_{12}$: A novel high temperature stable thermal barrier material. *Journal of Materials Science & Technology* **48**, 57–62 (2020).

[154] Vinnik, D. A. *et al.* High Entropy Oxide Phases with Perovskite Structure. *Nanomaterials* **10**, 268 (2020).

[155] Vinnik, D. A. *et al.* The new extremely substituted high entropy (Ba,Sr,Ca,La)Fe_6-x(Al,Ti,Cr,Ga,In,Cu,W)$_xO_{19}$ microcrystals with magnetoplumbite structure. *Ceramics International* **46**, 9656–9660 (2020).

[156] Dąbrowa, J. *et al.* An innovative approach to design SOFC air electrode materials: high entropy $La_{1-x}Sr_x(Co,Cr,Fe,Mn,Ni)O_{3-\delta}$ (x = 0, 0.1, 0.2, 0.3) perovskites synthesized by the sol–gel method. *Journal of Materials Chemistry A* **8**, 24455–24468 (2020).

[157] Zhang, J.-C., Sun, S., Yang, Z.-M., Qiu, N. & Wang, Y. Extended damage range of $(Al_{0.3}Cr_{0.2}Fe_{0.2}Ni_{0.3})_3O_4$ high entropy oxide films induced by surface irradiation. *Chinese Physics B* **29**, 066104 (2020).

[158] Krawczyk, P. A. *et al.* High-Entropy Perovskites as Multifunctional Metal Oxide Semiconductors: Synthesis and Characterization of $(Gd_{0.2}Nd_{0.2}La_{0.2}Sm_{0.2}Y_{0.2})CoO_3$. *ACS Applied Electronic Materials* **2**, 3211–3220 (2020).

[159] Sun, L. *et al.* A multicomponent γ-type $(Gd_{1/6}Tb_{1/6}Dy_{1/6}Tm_{1/6}Yb_{1/6}Lu_{1/6})_2Si_2O_7$ disilicate with outstanding thermal stability. *Materials Research Letters* **8**, 424–430 (2020).

[160] Chen, T.-Y. *et al.* In operando synchrotron X-ray studies of a novel spinel $(Ni_{0.2}Co_{0.2}Mn_{0.2}Fe_{0.2}Ti_{0.2})_3O_4$ high-entropy oxide for energy storage applications. *Journal of Materials Chemistry A* **8**, 21756–21770 (2020).

[161] Liu, J., Ren, K., Ma, C., Du, H. & Wang, Y. Dielectric and energy storage properties of flash-sintered high-entropy $(Bi_{0.2}Na_{0.2}K_{0.2}Ba_{0.2}Ca_{0.2})TiO_3$ ceramic. *Ceramics International* **46**, 20576–20581 (2020).

[162] Mao, A. *et al.* A novel six-component spinel-structure high-entropy oxide with ferrimagnetic property. *Journal of Magnetism and Magnetic Materials* **503**, 166594 (2020).

[163] Du, Q. *et al.* Phase evolution and dielectric properties of $Ba(Ti_{1/6}Sn_{1/6}Zr_{1/6}Hf_{1/6}Nb_{1/6}Ga_{1/6})O_3$ high-entropy perovskite ceramics. *Journal of Materials Science: Materials in Electronics* (2020).

[164] Meisenheimer, P. B. & Heron, J. T. Oxides and the high entropy regime: A new mix for engineering physical properties. *MRS Advances* **5**, 3419–3436 (2020).

[165] Rost, C. M., Rak, Z., Brenner, D. W. & Maria, J.-P. Local structure of the $Mg_xNi_xCo_xCu_xZn_xO$ (x=0.2) entropy-stabilized oxide: An EXAFS study. *Journal of the American Ceramic Society* **100**, 2732–2738.

[166] Esser, B. *et al.* Quantitative STEM Imaging of Order-Disorder Phenomena in Double Perovskite Thin Films. *Physical Review Letters* **117**, 176101 (2016).

[167] Patel, R. K. *et al.* Epitaxial stabilization of ultra thin films of high entropy perovskite. *Applied Physics Letters* **116**, 071601 (2020).

[168] Sharma, Y. *et al.* Single-crystal high entropy perovskite oxide epitaxial films. *Physical Review Materials* **2**, 060404 (2018).

[169] Assal, J., Hallstedt, B. & Gauckler, L. J. Thermodynamic evaluation of the Mg-Cu-O system. *Zeitschrift fuer Metallkunde* **87** (1996).

[170] Zabdyr, L. A. & Fabrichnaya, O. B. Phase equilibria in the cobalt oxide-copper oxide system. *Journal of Phase Equilibria* **23**, 149 (2002).

[171] Perrot, P. & Kumar, H. Cu-Ni-O Ternary Phase Diagram Evaluation. Tech. Rep. 10.14969.1.8, MSI Materials Science International Services GmbH, Stuttgart. URL https://materials.springer.com/msi/docs/sm_msi_r_10_014969_01.

[172] Sarver, J. F., Katnack, F. L. & Hummel, F. A. Phase Equilibria and Manganese-Activated Fluorescence in the System $Zn_3(PO_4)_2$ - $Mg_3(PO_4)_2$. *Journal of The Electrochemical Society* **106**, 960 (1959).

[173] Bates, C. H., White, W. B. & Roy, R. The solubility of transition metal oxides in zinc oxide and the reflectance spectra of Mn2+ and Fe2+ in tetrahedral fields. *Journal of Inorganic and Nuclear Chemistry* **28**, 397–405 (1966).

[174] Krogstad, M. J. *et al.* The relation of local order to material properties in relaxor ferroelectrics. *Nature Materials* 1 (2018).

[175] Damjanovic, D. Ferroelectric, dielectric and piezoelectric properties of ferroelectric thin films and ceramics. *Reports on Progress in Physics* **61**, 1267 (1998).

[176] Cheng, Z.-Y., Katiyar, R. S., Yao, X. & Bhalla, A. S. Temperature dependence of the dielectric constant of relaxor ferroelectrics. *Physical Review B* **57**, 8166–8177 (1998).

[177] Grinberg, I., Cooper, V. R. & Rappe, A. M. Oxide chemistry and local structure of $Pb(Zr_xTi_{1-x})O_3$ studied by density-functional theory supercell calculations. *Physical Review B* **69**, 144118 (2004).

[178] Grinberg, I., Cooper, V. R. & Rappe, A. M. Relationship between local structure and phase transitions of a disordered solid solution. *Nature* **419**, 909–911 (2002).

[179] Eremenko, M. *et al.* Local atomic order and hierarchical polar nanoregions in a classical relaxor ferroelectric. *Nature Communications* **10**, 1–9 (2019).

[180] Manley, M. E. *et al.* Giant electromechanical coupling of relaxor ferroelectrics controlled by polar nanoregion vibrations. *Science Advances* **2**, e1501814 (2016).

[181] Li, F. *et al.* The origin of ultrahigh piezoelectricity in relaxor-ferroelectric solid solution crystals. *Nature Communications* **7**, 1–9 (2016).

[182] Rák, Z., Maria, J. P. & Brenner, D. W. Evidence for Jahn-Teller compression in the (Mg, Co, Ni, Cu, Zn)O entropy-stabilized oxide: A DFT study. *Materials Letters* **217**, 300–303 (2018).

[183] Berardan, D., Meena, A. K., Franger, S., Herrero, C. & Dragoe, N. Controlled Jahn-Teller distortion in (MgCoNiCuZn)O-based high entropy oxides. *Journal of Alloys and Compounds* **704**, 693–700 (2017).

[184] Dixit, A., Majumder, S. B., Katiyar, R. S. & Bhalla, A. S. Studies on the relaxor behavior of sol-gel derived $Ba(Zr_xTi_{1-x})O_3$ (0.30<x<0.70) thin films. *Journal of Materials Science* **41**, 87–96 (2006).

[185] Gild, J. *et al.* High-Entropy Metal Diborides: A New Class of High-Entropy Materials and a New Type of Ultrahigh Temperature Ceramics. *Scientific Reports* **6**, 37946 (2016).

[186] Braun, J. L. *et al.* Charge-Induced Disorder Controls the Thermal Conductivity of Entropy-Stabilized Oxides. *Advanced Materials* **30**, 1805004 (2018).

[187] Rak, Z. *et al.* Charge compensation and electrostatic transferability in three entropy-stabilized oxides: Results from density functional theory calculations. *Journal of Applied Physics* **120**, 095105 (2016).

[188] Li, F., Zhou, L., Liu, J.-X., Liang, Y. & Zhang, G.-J. High-entropy pyrochlores with low thermal conductivity for thermal barrier coating materials. *Journal of Advanced Ceramics* **8**, 576–582 (2019).

[189] Gild, J. *et al.* High-entropy fluorite oxides. *Journal of the European Ceramic Society* **38**, 3578–3584 (2018).

[190] Yan, X. *et al.* $(Hf_{0.2}Zr_{0.2}Ta_{0.2}Nb_{0.2}Ti_{0.2})C$ high-entropy ceramics with low thermal conductivity. *Journal of the American Ceramic Society* **101**, 4486–4491 (2018).

[191] Brahlek, M. *et al.* Unexpected crystalline homogeneity from the disordered bond network in $La(Cr_{0.2}Mn_{0.2}Fe_{0.2}Co_{0.2}Ni_{0.2})O_3$ films. *arXiv:2004.02985 [cond-mat]* (2020).

[192] Sarkar, A. *et al.* High entropy oxides for reversible energy storage. *Nature Communications* **9**, 1–9 (2018).

[193] Qiu, N. *et al.* A high entropy oxide ($Mg_{0.2}Co_{0.2}Ni_{0.2}Cu_{0.2}Zn_{0.2}O$) with superior lithium storage performance. *Journal of Alloys and Compounds* **777**, 767–774 (2019).

[194] Wang, Q. *et al.* High entropy oxides as anode material for Li-ion battery applications: A practical approach. *Electrochemistry Communications* **100**, 121–125 (2019).

[195] Zheng, Y. *et al.* A high-entropy metal oxide as chemical anchor of polysulfide for lithium-sulfur batteries. *Energy Storage Materials* **23**, 678–683 (2019).

[196] Chen, H. *et al.* Entropy-stabilized metal oxide solid solutions as CO oxidation catalysts with high-temperature stability. *Journal of Materials Chemistry A* **6**, 11129–11133 (2018).

[197] Chen, H. *et al.* Mechanochemical Synthesis of High Entropy Oxide Materials under Ambient Conditions: Dispersion of Catalysts via Entropy Maximization. *ACS Materials Letters* **1**, 83–88 (2019).

[198] Grzesik, Z. *et al.* Defect structure and transport properties in (Co,Cu,Mg,Ni,Zn)O high entropy oxide. *Journal of the European Ceramic Society* **39**, 4292–4298 (2019).

[199] Bhaskar, L. K., Nallathambi, V. & Kumar, R. Critical role of cationic local stresses on the stabilization of entropy-stabilized transition metal oxides. *Journal of the American Ceramic Society* **103**, 3416–3424 (2020).

[200] Lin, M.-I., Tsai, M.-H., Shen, W.-J. & Yeh, J.-W. Evolution of structure and properties of multi-component (AlCrTaTiZr)O_x films. *Thin Solid Films* **518**, 2732–2737 (2010).

[201] Tsau, C.-H., Yang, Y.-C., Lee, C.-C., Wu, L.-Y. & Huang, H.-J. The Low Electrical Resistivity of the High-entropy Alloy Oxide Thin Films. *Procedia Engineering* **36**, 246–252 (2012).

[202] Tsau, C.-H., Hwang, Z.-Y. & Chen, S.-K. The Microstructures and Electrical Resistivity of (Al, Cr, Ti)FeCoNiO_x High-Entropy Alloy Oxide Thin Films (2015).

[203] Sarkar, A. *et al.* Role of intermediate 4f states in tuning the band structure of high entropy oxides. *arXiv:2003.00268 [cond-mat]* (2020).

[204] Goodenough, J. B. Theory of the Role of Covalence in the Perovskite-Type Manganites [La, M(II)]MnO_3. *Physical Review* **100**, 564–573 (1955).

[205] Kanamori, J. Superexchange interaction and symmetry properties of electron orbitals. *Journal of Physics and Chemistry of Solids* **10**, 87–98 (1959).

[206] Anderson, P. W. Antiferromagnetism. Theory of Superexchange Interaction. *Physical Review* **79**, 350–356 (1950).

[207] Bramwell, S. T. & Gingras, M. J. P. Spin Ice State in Frustrated Magnetic Pyrochlore Materials. *Science* **294**, 1495–1501 (2001).

[208] Iwata-Harms, J. M. *et al.* Controlling spin ordering in frustrated magnets via thin film heteroepitaxy. *Physical Review B* **85**, 214424 (2012).

[209] Sherrington, D. Neural networks: the spin glass approach. In Taylor, J. G. (ed.) *North-Holland Mathematical Library*, vol. 51, 261–291.

[210] Parisi, G. Spin glasses, complexity and all that. *Physica A: Statistical Mechanics and its Applications* **194**, 28–40 (1993).

[211] Ramirez, A. P., Hayashi, A., Cava, R. J., Siddharthan, R. & Shastry, B. S. Zero-point entropy in 'spin ice'. *Nature* **399**, 333–335 (1999).

[212] Broholm, C. *et al.* Quantum spin liquids. *Science* **367** (2020).

[213] Dijkkamp, D. *et al.* Preparation of Y-Ba-Cu oxide superconductor thin films using pulsed laser evaporation from high Tc bulk material. *Applied Physics Letters* **51**, 619–621 (1987).

[214] Balents, L. Spin liquids in frustrated magnets. *Nature* **464**, 199–208 (2010).

[215] Witte, R. *et al.* High-entropy oxides: An emerging prospect for magnetic rare-earth transition metal perovskites. *Physical Review Materials* **3**, 034406 (2019).

[216] Frandsen, B. A. *et al.* Spin dynamics and a nearly continuous magnetic phase transition in an entropy-stabilized oxide antiferromagnet. *arXiv:2004.04218 [cond-mat]* (2020).

[217] Radu, F. & Zabel, H. Exchange bias effect of ferro-/antiferromagnetic heterostructures. *Springer Tracts in Modern Physics* **227**, 97–184 (2007).

[218] Heron, J. T. *et al.* Electric-field-induced magnetization reversal in a ferromagnet-multiferroic heterostructure. *Physical Review Letters* **107**, 1–5 (2011).

[219] Mao, A. *et al.* A new class of spinel high-entropy oxides with controllable magnetic properties. *Journal of Magnetism and Magnetic Materials* **497**, 165884 (2020).

[220] Musicó, B. *et al.* Tunable magnetic ordering through cation selection in entropic spinel oxides. *Physical Review Materials* **3**, 104416 (2019).

[221] Sharma, Y. *et al.* Magnetic anisotropy in single-crystal high-entropy perovskite oxide $LaCr_{0.2}Mn_{0.2}Fe_{0.2}Co_{0.2}Ni_{0.2}O_3$ films. *Physical Review Materials* **4**, 014404 (2020).

[222] Amit, D. J., Gutfreund, H. & Sompolinsky, H. Spin-glass models of neural networks. *Physical Review A* **32**, 1007–1018 (1985).

[223] Baldi, P. & Venkatesh, S. S. Number of stable points for spin-glasses and neural networks of higher orders. *Physical Review Letters* **58**, 913–916 (1987).

[224] Hamilton, K. E., Schuman, C. D., Young, S. R., Imam, N. & Humble, T. S. Neural Networks and Graph Algorithms with Next-Generation Processors. In *2018 IEEE International Parallel and Distributed Processing Symposium Workshops (IPDPSW)*, 1194–1203 (2018).

[225] Bert, F., Dupuis, V., Vincent, E., Hammann, J. & Bouchaud, J.-P. Spin Anisotropy and Slow Dynamics in Spin Glasses. *Physical Review Letters* **92**, 167203 (2004).

[226] Parisi, G., Ritort, F. & Slanina, F. Several results on the finite-size corrections in the Sherrington-Kirkpatrick spin-glass model. *Journal of Physics A: Mathematical and General* **26**, 3775–3789 (1993).

[227] Parisi, G. & Slanina, F. Generalization of Rules by Neural Nets. *Europhysics Letters (EPL)* **17**, 497–502 (1992).

[228] Mézard, M. & Parisi, G. Thermodynamics of glasses: a first principles computation. *Journal of Physics: Condensed Matter* **11**, A157–A165 (1999).

[229] Sidebottom, D. L. Connecting Glass-Forming Fragility to Network Topology. *Frontiers in Materials* **6** (2019).

[230] Yildirim, C., Raty, J.-Y. & Micoulaut, M. Revealing the role of molecular rigidity on the fragility evolution of glass-forming liquids. *Nature Communications* **7** (2016).

[231] Gruyters, M. Spin-Glass-Like Behavior in CoO Nanoparticles and the Origin of Exchange Bias in Layered CoO/Ferromagnet Structures. *Physical Review Letters* **95**, 077204 (2005).

[232] Ali, M. *et al.* Exchange bias using a spin glass. *Nature Materials* **6**, 70–75 (2007).

[233] Rák, Z. & Brenner, D. W. Exchange interactions and long-range magnetic order in the (Mg,Co,Cu,Ni,Zn)O entropy-stabilized oxide: A theoretical investigation. *Journal of Applied Physics* **127**, 185108 (2020).

[234] Menshikov, A. Z., Dorofeev, Y. A., Klimenko, A. G. & Mironova, N. A. Magnetic Phase Diagram of $(Ni_{1-x}Mg_x)O$ Solid Solutions. *physica status solidi (b)* **164**, 275–283 (1991).

[235] Seehra, M. S., Dean, J. C. & Kannan, R. Magnetic phase diagrams of diluted fcc antiferromagnets $Co_pMg_{1-p}O$ and $Eu_pSr_{1-p}Te$. *Physical Review B* **37**, 5864–5865 (1988).

[236] Praveen, S. & Kim, H. S. High-Entropy Alloys: Potential Candidates for High-Temperature Applications – An Overview. *Advanced Engineering Materials* **20**, 1700645.

[237] Huang, H. *et al.* Phase-Transformation Ductilization of Brittle High-Entropy Alloys via Metastability Engineering. *Advanced Materials* **29**, 1701678 (2017).

[238] Acet, M. Inducing strong magnetism in $Cr_{20}Mn_{20}Fe_{20}Co_{20}Ni_{20}$ high-entropy alloys by exploiting its anti-Invar property. *AIP Advances* **9**, 095037 (2019).

[239] Li, P., Wang, A. & Liu, C. T. A ductile high entropy alloy with attractive magnetic properties. *Journal of Alloys and Compounds* **694**, 55–60 (2017).

[240] Schneeweiss, O. *et al.* Magnetic properties of the CrMnFeCoNi high-entropy alloy. *Physical Review B* **96**, 014437 (2017).

[241] Chang, X., Zeng, M., Liu, K. & Fu, L. Phase Engineering of High-Entropy Alloys. *Advanced Materials* **n/a**, 1907226.

[242] Niu, C., LaRosa, C. R., Miao, J., Mills, M. J. & Ghazisaeidi, M. Magnetically-driven phase transformation strengthening in high entropy alloys. *Nature Communications* **9**, 1–9 (2018).

[243] Dąbrowa, J. & Danielewski, M. State-of-the-Art Diffusion Studies in the High Entropy Alloys. *Metals* **10**, 347 (2020).

[244] Maier-Kiener, V., Schuh, B., George, E. P., Clemens, H. & Hohenwarter, A. Insights into the deformation behavior of the CrMnFeCoNi high-entropy alloy revealed by elevated temperature nanoindentation. *Journal of Materials Research* **32**, 2658–2667 (2017).

[245] Esser, B. D. *et al.* Quantifying Ordering Phenomena Through High-Resolution Electron Microscopy, Spectroscopy, and Simulation. *Microscopy and Microanalysis; Cambridge* **22**, 1448–1449 (2016).

[246] Kaufmann, K. *et al.* Discovery of high-entropy ceramics via machine learning. *npj Computational Materials* **6**, 1–9 (2020).

[247] Sarker, P. *et al.* High-entropy high-hardness metal carbides discovered by entropy descriptors. *Nature Communications* **9**, 1–10 (2018).

[248] Zhang, Y. *et al.* Microstructures and properties of high-entropy alloys. *Progress in Materials Science* **61**, 1–93 (2014).

[249] Zou, Y., Ma, H. & Spolenak, R. Ultrastrong ductile and stable high-entropy alloys at small scales. *Nature Communications* **6**, 7748 (2015).

[250] Fazakas, E. *et al.* Experimental and theoretical study of $Ti_{20}Zr_{20}Hf_{20}Nb_{20}X_{20}$ (X = V or Cr) refractory high-entropy alloys. *International Journal of Refractory Metals and Hard Materials* **47**, 131–138 (2014).

[251] Zhou, J. *et al.* High-entropy carbide: A novel class of multicomponent ceramics. *Ceramics International* **44**, 22014–22018 (2018).

[252] Schlom, D. G. *et al.* Strain Tuning of Ferroelectric Thin Films. *Annual Review of Materials Research* **37**, 589–626 (2007).

[253] Bhattacharya, A. & May, S. J. Magnetic Oxide Heterostructures. *Annu. Rev. Mater. Res* **44**, 65–90 (2014).

[254] Takano, K., Kodama, R. H., Berkowitz, A. E., Cao, W. & Thomas, G. Interfacial Uncompensated Antiferromagnetic Spins: Role in Unidirectional Anisotropy in Polycrystalline $Ni_{81}Fe_{19}$/CoO Bilayers. *Physical Review Letters* **79**, 1130–1133 (1997).

[255] Roy, S. *et al.* Depth Profile of Uncompensated Spins in an Exchange Bias System. *Physical Review Letters* **95**, 047201 (2005).

[256] Hong, J.-I., Leo, T., Smith, D. J. & Berkowitz, A. E. Enhancing Exchange Bias with Diluted Antiferromagnets. *Physical Review Letters* **96**, 117204 (2006).

[257] Ambrose, T., Liu, K. & Chien, C. L. Doubly exchange-biased NiCoO/NiFe/Cu/NiFe/NiCoO spin valves. *Journal of Applied Physics* **85**, 6124–6126 (1999).

[258] Carey, M. J. & Berkowitz, A. E. Exchange anisotropy in coupled films of $Ni_{81}Fe_{19}$ with NiO and $Co_xNi_{1-x}O$. *Applied Physics Letters* **60**, 3060–3062 (1992).

[259] Topkaya, R. & Kazan, S. Enhancement of exchange bias with crystal orientation in NiFe/CoO and CoO/NiFe bilayers grown on MgO(100) and MgO(111). *Journal of Magnetism and Magnetic Materials* **368**, 300–307 (2014).

[260] Kuanr, B. K., Camley, R. E. & Celinski, Z. Exchange bias of NiO/NiFe: Linewidth broadening and anomalous spin-wave damping. *Journal of Applied Physics* **93**, 7723–7725 (2003).

[261] Shannon, R. D. Revised effective ionic radii and systematic studies of interatomic distances in halides and chalcogenides. *Acta Crystallographica Section A: Crystal Physics, Diffraction, Theoretical and General Crystallography* **32**, 751–767 (1976).

[262] Brooks, C. M. *et al.* Growth of homoepitaxial $SrTiO_3$ thin films by molecular-beam epitaxy. *Applied Physics Letters* **94**, 162905 (2009).

[263] Zhou, F., Cococcioni, M., Marianetti, C. A., Morgan, D. & Ceder, G. First-principles prediction of redox potentials in transition-metal compounds with LDA+U. *Physical Review B* **70**, 235121 (2004).

[264] Wu, S. Z. *et al.* Strain-mediated electric-field control of exchange bias in a $Co_{90}Fe_{10}$/$BiFeO_3$/$SrRuO_3$/PMN-PT heterostructure. *Scientific Reports* **5**, srep08905 (2015).

[265] Zhu, J. *et al.* Strain-modulated antiferromagnetic spin orientation and exchange coupling in Fe/CoO(001). *Journal of Applied Physics* **115**, 193903 (2014).

[266] Dimitrov, D. V., Zhang, S., Xiao, J. Q., Hadjipanayis, G. C. & Prados, C. Effect of exchange interactions at antiferromagnetic/ferromagnetic interfaces on exchange bias and coercivity. *Physical Review B* **58**, 12090–12094 (1998).

[267] Martin, L. W. *et al.* Nanoscale Control of Exchange Bias with $BiFeO_3$ Thin Films. *Nano Letters* **8**, 2050–2055 (2008).

[268] Nowak, U. *et al.* Domain state model for exchange bias. I. Theory. *Physical Review B* **66**, 014430 (2002).

[269] Keller, J. *et al.* Domain state model for exchange bias. II. Experiments. *Physical Review B* **66**, 014431 (2002).

[270] Siemons, W. *et al.* Tetragonal CuO: A new end member of the 3d transition metal monoxides. *Physical Review B* **79** (2009).

[271] Peralta, G., Puggioni, D., Filippetti, A. & Fiorentini, V. Jahn-Teller stabilization of magnetic and orbital ordering in rocksalt CuO. *Physical Review B* **80**, 140408 (2009).

[272] Misra, A., Nowak, U. & Usadel, K. D. Control of exchange bias by diluting the antiferromagnetic layer. *Journal of Applied Physics* **93**, 6593–6595 (2003).

[273] Zhang, Y., Zhou, Y. J., Lin, J. P., Chen, G. L. & Liaw, P. K. Solid-solution phase formation rules for multi-component alloys. *Advanced Engineering Materials* **10**, 534–538 (2008).

[274] Goodenough, J. B. Metallic oxides. *Progress in Solid State Chemistry* **5**, 145–399 (1971).

[275] Shoemaker, D. P. & Seshadri, R. Total-scattering descriptions of local and cooperative distortions in the oxide spinel $Mg_{1-x}Cu_xCr_2O_4$ with dilute Jahn-Teller ions. *Physical Review B* **82**, 214107 (2010).

[276] Binek, C., Hochstrat, A. & Kleemann, W. Exchange bias in a generalized Meiklejohn–Bean approach. *Journal of Magnetism and Magnetic Materials* **234**, 353–358 (2001).

[277] Keen, D. A. & Goodwin, A. L. The crystallography of correlated disorder. *Nature* **521**, 303–309 (2015).

[278] Huang Kun & Mott Nevill Francis. X-ray reflexions from dilute solid solutions. *Proceedings of the Royal Society of London. Series A. Mathematical and Physical Sciences* **190**, 102–117 (1947).

[279] Debye, P. Interferenz von Röntgenstrahlen und Wärmebewegung. *Annalen der Physik* **348**, 49–92 (1913).

[280] Waller, I. Zur Frage der Einwirkung der Wärmebewegung auf die Interferenz von Röntgenstrahlen. *Zeitschrift für Physik* **17**, 398–408 (1923).

[281] Warren, B. E., Averbach, B. L. & Roberts, B. W. Atomic Size Effect in the X-Ray Scattering by Alloys. *Journal of Applied Physics* **22**, 1493–1496 (1951).

[282] Kresse, G. & Joubert, D. From ultrasoft pseudopotentials to the projector augmented-wave method. *Physical Review B* **59**, 1758–1775 (1999).

[283] Blöchl, P. E. Projector augmented-wave method. *Physical Review B* **50**, 17953–17979 (1994).

[284] Kresse, G. & Hafner, J. Ab initio molecular dynamics for liquid metals. *Physical Review B* **47**, 558–561 (1993).

[285] Kresse, G. & Hafner, J. Ab initio molecular-dynamics simulation of the liquid-metal–amorphous-semiconductor transition in germanium. *Physical Review B* **49**, 14251–14269 (1994).

[286] Kresse, G. & Furthmüller, J. Efficiency of ab-initio total energy calculations for metals and semiconductors using a plane-wave basis set. *Computational Materials Science* **6**, 15–50 (1996).

[287] Kresse, G. & Furthmüller, J. Efficient iterative schemes for ab initio total-energy calculations using a plane-wave basis set. *Physical Review B* **54**, 11169–11186 (1996).

[288] Perdew, J. P., Burke, K. & Ernzerhof, M. Generalized Gradient Approximation Made Simple. *Physical Review Letters* **77**, 3865–3868 (1996).

[289] van de Walle, A. *et al.* Efficient stochastic generation of special quasirandom structures. *Calphad* **42**, 13–18 (2013).

[290] Rocquefelte, X., Schwarz, K. & Blaha, P. Theoretical Investigation of the Magnetic Exchange Interactions in Copper(II) Oxides under Chemical and Physical Pressures. *Scientific Reports* **2**, 1–5 (2012).

[291] Shimizu, T. *et al.* Spin susceptibility and superexchange interaction in the antiferromagnet CuO. *Physical Review B* **68**, 224433 (2003).

[292] Snyder, J., Slusky, J. S., Cava, R. J. & Schiffer, P. How 'spin ice' freezes. *Nature* **413**, 48–51 (2001).

[293] Ramirez, A. P. Chapter 4 Geometrical frustration. In *Handbook of Magnetic Materials*, vol. 13, 423–520.

[294] Chang, C. F. *et al.* Spin Blockade, Orbital Occupation, and Charge Ordering in $La_{1.5}Sr_{0.5}CoO_4$. *Physical Review Letters* **102**, 116401 (2009).

[295] Radu, F., Westphalen, A., Theis-Bröhl, K. & Zabel, H. Quantitative description of the azimuthal dependence of the exchange bias effect. *Journal of Physics: Condensed Matter* **18**, L29 (2006).

[296] Radu, F. *et al.* Soft X-ray resonant magnetic scattering studies on Fe/CoO exchange bias system. *Journal of Magnetism and Magnetic Materials* **300**, 206–210 (2006).

[297] Hagemann, I. S., Khalifah, P. G., Ramirez, A. P. & Cava, R. J. Geometric magnetic frustration in olivines. *Physical Review B* **62**, R771–R774 (2000).

[298] Karel, J. *et al.* Using structural disorder to enhance the magnetism and spin-polarization in Fe_xSi_{1-x} thin films for spintronics. *Materials Research Express* **1**, 026102 (2014).

[299] Liao, Z. & Zhang, J. Metal-to-Insulator Transition in Ultrathin Manganite Heterostructures. *Applied Sciences* **9**, 144 (2019).

[300] Hollmann, E., Schubert, J., Kutzner, R. & Wördenweber, R. Stress generated modifications of epitaxial ferroelectric $SrTiO_3$ films on sapphire. *Journal of Applied Physics* **105**, 114104 (2009).

[301] Martin, L. W. & Rappe, A. M. Thin-film ferroelectric materials and their applications. *Nature Reviews Materials* **2**, 16087 (2017).

[302] Baek, S. H. *et al.* Giant Piezoelectricity on Si for Hyperactive MEMS. *Science* **334**, 958–961 (2011).

[303] Bhowmik, D., You, L. & Salahuddin, S. Spin Hall effect clocking of nanomagnetic logic without a magnetic field. *Nature Nanotechnology* **9**, 59–63 (2014).

[304] Dutta, S. *et al.* Thickness dependence of the resistivity of platinum-group metal thin films. *Journal of Applied Physics* **122**, 025107 (2017).

[305] Parkin, S. S. P. *et al.* Giant tunnelling magnetoresistance at room temperature with MgO (100) tunnel barriers. *Nature Materials* **3**, 862–867 (2004).

[306] Ikeda, S. *et al.* Tunnel magnetoresistance of 604% at 300K by suppression of Ta diffusion in CoFeB/MgO/CoFeB pseudo-spin-valves annealed at high temperature. *Applied Physics Letters* **93**, 082508 (2008).

[307] Takamura, Y. *et al.* Tuning Magnetic Domain Structure in Nanoscale $La_{0.7}Sr_{0.3}MnO_3$ Islands. *Nano Letters* **6**, 1287–1291 (2006).

[308] Steffes, J. J., Ristau, R. A., Ramesh, R. & Huey, B. D. Thickness scaling of ferroelectricity in $BiFeO_3$ by tomographic atomic force microscopy. *Proceedings of the National Academy of Sciences* **116**, 2413–2418 (2019).

[309] Xu, R. *et al.* Reducing Coercive-Field Scaling in Ferroelectric Thin Films via Orientation Control. *ACS Nano* **12**, 4736–4743 (2018).

[310] Nordlander, J. *et al.* The ultrathin limit of improper ferroelectricity. *Nature Communications* **10**, 1–7 (2019).

[311] Saremi, S. *et al.* Enhanced Electrical Resistivity and Properties via Ion Bombardment of Ferroelectric Thin Films. *Advanced Materials* **28**, 10750–10756 (2016).

[312] Ma, Z. *et al.* Effect of 90° domain movement on the piezoelectric response of patterned $PbZr_{0.2}Ti_{0.8}O_3$/$SrTiO_3$/Si heterostructures. *Applied Physics Letters* **87**, 072907 (2005).

[313] Sun, T. *et al.* Nanopatterning of multiferroic $BiFeO_3$ using “soft” electron beam lithography. *Applied Physics Letters* **89**, 163117 (2006).

[314] Sun, F. *et al.* Phase transitions in BiFeO3 nanoislands with enhanced electromechanical response. *Ceramics International* **44**, 21725–21729 (2018).

[315] Lu, D. *et al.* Synthesis of freestanding single-crystal perovskite films and heterostructures by etching of sacrificial water-soluble layers. *Nature Materials* **15**, 1255–1260 (2016).

[316] Ji, D. *et al.* Freestanding crystalline oxide perovskites down to the monolayer limit. *Nature* **570**, 87–90 (2019).

[317] Bakaul, S. R. *et al.* Single crystal functional oxides on silicon. *Nature Communications* **7**, ncomms10547 (2016).

[318] Xu, R. *et al.* Strain-induced room-temperature ferroelectricity in $SrTiO_3$ membranes. *Nature Communications* **11**, 3141 (2020).

[319] Riemer, L. M. *et al.* Macroscopic polarization in the nominally ergodic relaxor state of lead magnesium niobate. *Applied Physics Letters* **117**, 102901 (2020).

[320] Kleemann, W. & Dec, J. Relaxor ferroelectrics and related superglasses. *Ferroelectrics* **553**, 1–7 (2019).

[321] Kleemann, W. & Dec, J. Ferroic superglasses: Polar nanoregions in relaxor ferroelectric PMN versus CoFe superspins in a discontinuous multilayer. *Physical Review B* **94**, 174203 (2016).

[322] Tagantsev, A. K. & Glazounov, A. E. Mechanism of polarization response in the ergodic phase of a relaxor ferroelectric. *Physical Review B* **57**, 18–21 (1998).

[323] Kumar, A. *et al.* Atomic-resolution electron microscopy of nanoscale local structure in lead-based relaxor ferroelectrics. *Nature Materials* **20**, 62–67 (2021).

[324] Sarkar, S., Ren, X. & Otsuka, K. Evidence for Strain Glass in the Ferroelastic-Martensitic System $Ti_{50-x}Ni_{50+x}$. *Physical Review Letters* **95**, 205702 (2005).

[325] Wang, F., Luo, L., Zhou, D., Zhao, X. & Luo, H. Complete set of elastic, dielectric, and piezoelectric constants of orthorhombic 0.71Pb($Mg_{1/3}Nb_{2/3}$)O3–0.29$PbTiO_3$ single crystal. *Applied Physics Letters* **90**, 212903 (2007).

[326] Choudhury, D. *et al.* Near-Room-Temperature Colossal Magnetodielectricity and Multiglass Properties in Partially Disordered La_2NiMnO_6. *Physical Review Letters* **108**, 127201 (2012).

[327] Kleemann, W. *et al.* Multiglass order and magnetoelectricity in Mn2+ doped incipientferroelectrics. *The European Physical Journal B* **71**, 407 (2009).

[328] Kleemann, W. *et al.* (Sr,Mn)TiO_3—a magnetoelectrically coupled multiglass. *Journal of Physics: Condensed Matter* **20**, 434216 (2008).

[329] Parisi, G. Spin glasses and fragile glasses: Statics, dynamics, and complexity. *Proceedings of the National Academy of Sciences* **103**, 7948–7955 (2006).

[330] Yuasa, S. & Djayaprawira, D. D. Giant tunnel magnetoresistance in magnetic tunnel junctions with a crystalline MgO(001) barrier. *Journal of Physics D: Applied Physics* **40**, R337 (2007).

[331] Krebs, H.-U. *et al.* Pulsed Laser Deposition (PLD) – A Versatile Thin Film Technique. In Kramer, B. (ed.) *Advances in Solid State Physics*, Advances in Solid State Physics, 505–518.

[332] Schroeder, J. L., Ingason, A. S., Rosén, J. & Birch, J. Beware of poor-quality MgO substrates: A study of MgO substrate quality and its effect on thin film quality. *Journal of Crystal Growth* **420**, 22–31 (2015).

[333] Geler-Kremer, J., Posadas, A. B. & Demkov, A. A. Preparation of clean MgO surface by oxygen plasma: Comparison with standard substrate cleaning procedures. *Journal of Vacuum Science & Technology B* **38**, 062201 (2020).

[334] Krajnovich, D. J. & Vázquez, J. E. Formation of “intrinsic” surface defects during 248 nm photoablation of polyimide. *Journal of Applied Physics* **73**, 3001–3008 (1993).

[335] Singh, R. K., Bhattacharya, D. & Narayan, J. Laser-Target Interactions and its Effect on Surface Morphology of Laser Deposited thin films. *MRS Online Proceedings Library (OPL)* **201** (1990).

[336] Jeong, Y. S. *et al.* Surface modification of laser ablated YBCO target. *Applied Surface Science* **109-110**, 424–427 (1997).

[337] Chen, C. T. *et al.* Experimental Confirmation of the X-Ray Magnetic Circular Dichroism Sum Rules for Iron and Cobalt. *Physical Review Letters* **75**, 152–155 (1995).